The University of Nottingham

Weld Consumables and PWHT for P92 Power Plant Steel

Kieran Chalk, BEng, MSc

Thesis submitted to the University of Nottingham for the degree of Doctor of Philosophy in Materials Engineering and Materials Design

2013

Acknowledgements

I would like to thank my supervisors Prof. Philip Shipway and Prof. Tom Hyde for their help and guidance throughout my studies, Dr David Allen of E.On for his advice and direction, Dr David Tanner for his support and collaboration in creep testing, Dr Geoff West of Loughborough University for his help with material characterization, Keith Dinsdale and Tom Buss for their help and advice. I would like to acknowledge the support of The Energy Programme, which is a Research Councils UK cross council initiative led by EPSRC and contributed to by ESRC, NERC, BBSRC and STFC, and specifically the Supergen initiative (Grants GR/S86334/01 and EP/F029748) and the following companies; Alstom Power Ltd., Doosan Babcock, E.On, National Physical Laboratory, Praxair Surface Technologies Ltd, QinetiQ, Rolls-Royce plc, RWE npower, Siemens Industrial Turbomachinery Ltd. and Tata Steel, for their valuable contributions to the project.

Abstract

P92 steel is a high-alloy steel that has been specifically designed for operating at high temperatures (600°C - 650°C) and has found wide use in the power generation industry, particularly since 2005. For the successful installation and use of this advanced steel, all aspects of its behaviour, in terms of both metallurgy and in-service behaviour, must be investigated. Investigating all the relevant material aspects is beyond the scope of a single PhD, and so the Supergen consortium funds a number of projects working on different material aspects. The purpose of this thesis is to investigate, and seek a greater understanding of, the behaviour of welds in P92 steel so that their in-service behaviour may be better understood particularly the response of the material to post-weld heat treatments (PWHT), the optimum weld consumable composition and the microstuctural development during creep-rupture. This understanding has been achieved through a combination of microstructural characterization, thermodynamic modelling and mechanical testing.

Specifications for weld metals define a range of compositions; thermodynamic modelling has enabled a better understanding of how the composition affects the final microstructure of P92 weld metal (given that this work is based upon thermodynamic predictions, the understanding developed here is applicable to both parent and weld metal). Precipitation strengthening is important to the creep resistance of P92 and the modelling has revealed how precipitate levels vary based on composition. Using this knowledge, quality checks on P92 used by industry can better ensure the fitness for service of a material if an accurate composition is known; furthermore, this understanding will enable manufacturers to further tailor compositions to produce the strongest possible material.

Following welding with P92 fillers, post-weld heat treatment is carried out, and there is a desire to perform this heat treatment close to the A_1[1] temperature of the materials involved. As such, it is important to accurately know the A_1 temperature of the materials being heat treated. A combination of thermodynamic modelling, experimental thermal analysis and microstructural characterization was used to investigate the key transformation of ferrite to austenite. This investigation focused on the

[1] A_1 = The temperature at which ferrite begins to transform to austenite on heating.

effect of composition on the transformation temperature, A_1, and the rate at which austenite could form during PWHT. An equation to predict the Ae_1 [2] temperature of P92 is produced and validated. The knowledge of how composition affects the A_1 temperature is useful for both welds and parent material, enabling the design and selection of P92 material that will not undesirably transform during heat treatments. It is proposed that the equation for Ae_1 allows the determination of maximum safe heat treatment temperatures and will reduce the likelihood of poor quality material entering service. Experimental work has demonstrated that during PWHT (or parent material tempering), equilibrium conditions are approached, confirming that Ae_1 should be used to determine maximum heat treatment temperatures instead of the Ac_1 [3] temperatures which are currently employed.

Creep testing of three different weld consumables was carried out to determine which had the best properties for use in service, and to understand the microstructural features which controlled creep behaviour of these weld metals. Creep testing of weld metal has indentified that δ-ferrite causes early failure as the resulting precipitate-free zones (PFZs) are creep weak. The presence of localized δ-ferrite is caused by an inhomogeneous distribution of ferrite stabilizers, particularly tungsten within the weld metal, resulting in greater stability of δ-ferrite and its retention in the weld. Using this knowledge, alloy specifications of weld consumables and corresponding welding procedures can be improved to ensure a homogeneous distribution of elements so that localized weaknesses in a weld can be avoided. There is tentative evidence that tungsten plays an important role in the creep ductility of P92 and that variations in tungsten and silicon could lead to an optimization of creep strength.

The outcomes of this thesis facilitate a better understanding of P92 parent metal and welds and provide results that are immediately applicable and useful to the power generation industry.

---

[2] Ae_1 = The theoretical temperature at which ferrite begins to transform to austenite on heating using only thermodynamic considerations.

[3] Ac_1 = The temperature at which ferrite begins to transform to austenite during continuous heating.

Table of Contents

1 Introduction

The constraints that are currently placed on power generation plant in terms of environmental impact and economics have focussed attention on the development of high efficiency, low emission systems. If thermal efficiencies of generating plants can be increased, fuel can be conserved (less fuel is required for a given power output) and emissions reduced (lower fuel consumption means lower emissions of environmentally damaging gases). An increase in the thermal efficiency of a power plant can be most effectively achieved by increasing the temperature and, to a lesser extent, the pressure of the steam entering the turbine. Most modern steam power stations now in operation reach efficiencies of around 42% with steam temperatures of up to 600°C and pressures of 25–30 MPa (Bugge et al. 2006; Chew 2003).

Steam generating fossil fuel fired power stations make up the majority of electrical power generation across the world; however they are inherently inefficient. Energy is lost as heat has to be removed to ensure that the metal, which makes up the majority of the power plant structure, remains at a safe operating temperature, thereby reducing the thermal efficiency of the system. Increasing the safe operating temperature of metals within the power plant reduces the energy that is lost to cooling, thereby increasing efficiency.

Conventional steam generating power plants currently fall into three categories depending on their operating conditions;

1. Subcritical plants that make up most of the steam generating power plants currently operating at temperatures lower than 600°C. Subcritical means that there is a non-homogeneous mixture of water and steam in the evaporator part of the boiler. In this case a drum-type boiler is used because the steam needs to be separated from water in the drum of the boiler before it is superheated and fed into the turbine.
2. Supercritical plants operating beyond the critical pressure of steam (255 bar) and at temperatures approaching 620°C. Supercritical power stations are also known as "once-through plants" because boiler water does not circulate multiple times through the steam

drum until it has transformed to steam; rather the water transforms to steam in the boiler waterwall due to the higher temperatures.

3. Research and development is ongoing to commercialize ultra-supercritical steam plants. Their "clean coal" technology would push efficiency rates higher and CO_2 and particulate emissions lower, compared to supercritical steam plants. Operating parameters have projected temperatures of 760°C and boiler feed discharge pressures from 330 bar to 420 bar.

Increasing the efficiency is in part a material issue, as higher operating efficiencies require materials that are able to operate at a higher temperature. Metals are the materials currently able to operate at high temperatures and withstand the stresses created by the steam they transport. The problem with metals is that when they are held at temperatures above a third of their melting temperature, they may suffer from a time dependent deformation process called creep, which eventually leads to failure.

Steels are the primary metal used for construction of power plants, in particular the parts which transfer heat in the boiler and transport steam to the turbines. For decades, efforts have been made to better design steels that have improved creep resistance, achieved primarily through alloy design and careful control of the microstructure. The alloying elements strengthen the steels by solid solution strengthening, precipitate strengthening and altering/controlling the development of the microstructure over time. Parent steels generally exhibit good creep resistance thanks to continuing improvements in material design, the pace of which has increased rapidly thanks to computer modelling which reduces the amount of experimental trial and error.

However, power plants are massive constructions made of many components that must be joined together. The joining of metals in the power plant is primarily done through welding. While the bulk material of components (so-called 'parent material') are carefully designed to have a homogeneous microstructure, welding of the large pipes introduces localised inhomogeneous microstructures that alter the mechanical properties of the structure as a whole.

The weld itself introduces a filler material that melts and fuses with the parent material, but while the composition of the filler may be similar to

the parent metal, there will be elements present at different levels, along with some additional elements, in order to control the microstructural outcome of the complex multi-pass weld thermal cycle. The thermal cycle associated with the welding process also affects the parent material adjacent to the weld metal, often detrimentally altering its microstructure. The thermal cycle also introduces residual stresses associated with the expansion and contraction of the filler metal during melting and solidification. Heat treatments following the welding process seek to reduce residual stresses and restore the material to a microstructural state which is acceptable for the application in which the structure is being utilised, but these heat treatments have to be carefully controlled so as to prevent the accidental formation of undesirable phases.

Invariably, the weldment becomes creep-weak compared to the parent, and therefore will be the region most likely to fail first during service. The steel P92 is currently one of the best performing creep-resistant high-temperature commercially available steels. It is important to understand how welds in this material will perform under creep and a full understanding of this requires an examination of:

- The chemical composition of potential filler metals.
- The microstructure that the welding process produces in the various zones of the weldment.
- The appropriate post-weld-heat-treatment for the weldment.
- The performance of the welds during creep.

2 Literature Review

2.1 Steam-Generating Power Plant

The Energy Information Administration (EIA) projects that total worldwide installed coal-fired generating capacity will approach 2000 GW by 2030, up from 1119 GW in 2003. More than 61% of the projected new generating capacity is expected to be in China (546 GW), followed by the U.S. (16.7%, 147 GW) and India (10.7%, 94 GW) (EIA 2006).The boiler is the heart of a PC (pulverised-coal) power plant, burning fuel to provide the steam that drives turbines to generate electricity. Technology improvements in PC boilers and in other plant components have yielded significant economies of scale along with improvements in efficiency, reliability, and environmental performance of the overall power plant. This has contributed to significant cost reductions since the introduction of PC plant technology (Paul et al. 2005). Figure 2.1 shows the cumulative installed capacity of pulverized coal-fired plants in the world from 1921 to 2004 (Yeh and Rubin 2007).

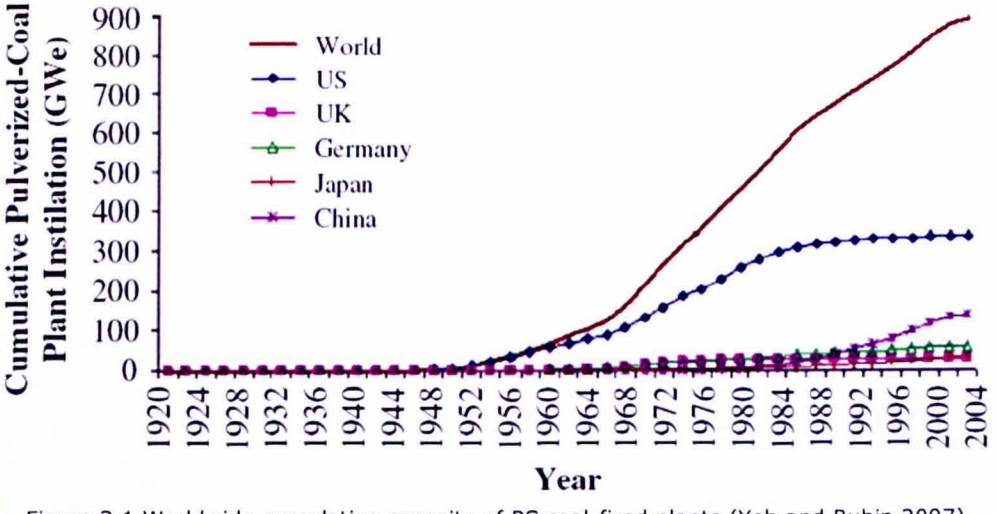

Figure 2.1 Worldwide cumulative capacity of PC coal-fired plants (Yeh and Rubin 2007)

While the majority of new PC boilers installed worldwide since 1990 have been subcritical units employing 166 bar/538°C/538°C drum boilers (Kitto 1996), supercritical boiler technology, operating at higher temperature and pressure, continues to be developed in Europe and Asia (primarily Japan). More recently, several "ultra-supercritical" boilers—with even higher temperature and pressure—were built in Europe and Japan, where higher coal prices justified the higher cost of these more efficient plants (Figure 2.2) (Bugge et al. 2006; Kitto 1996). In the 1990s, more efficient PC

plants using supercritical boiler technology achieved net plant efficiencies of 42–44% in Japan, Germany, Denmark, Netherlands, and most recently China (Yeh and Rubin 2007). Figure 2.3 shows the recent progress in PC plant efficiency, achieved via higher steam pressure and temperature, double reheat, and other design changes, albeit with an increase in capital cost. Other studies note that advances in materials and process components could allow ultra-supercritical boilers to achieve still higher efficiency within a decade (Viswanathan et al. 2006).

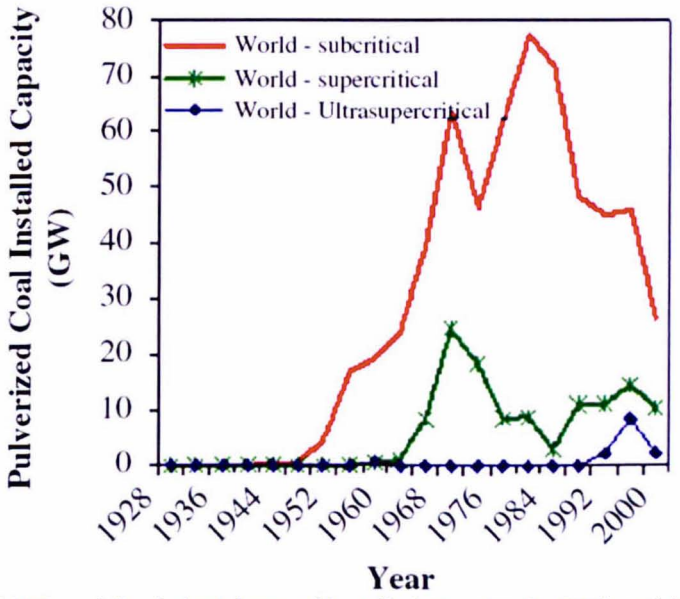

Figure 2.2 World PC coal-fired plants' annual installed capacity (in GW/year) by type of boiler (Yeh and Rubin 2007)

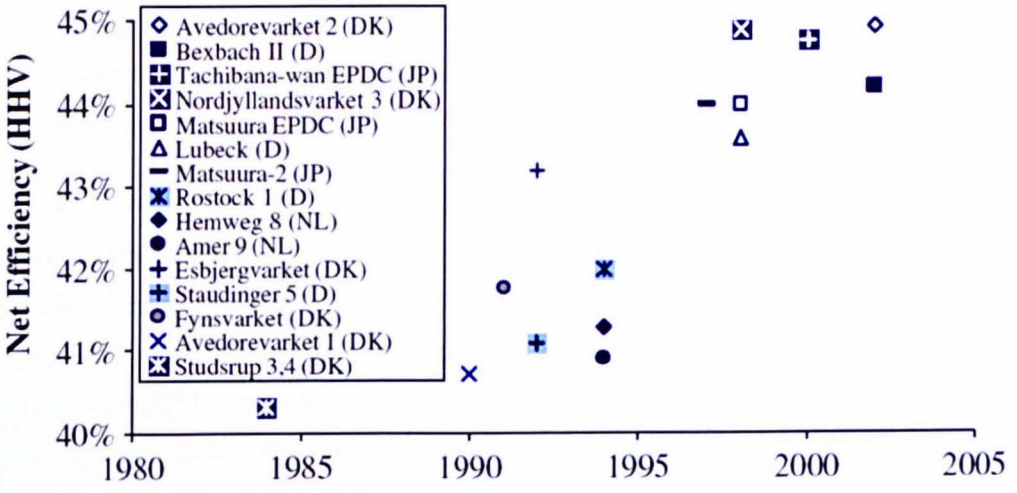

Figure 2.3 Recent progress in plant efficiency of PC coal-fired power plants in European countries and Japan (Bugge et al. 2006)

Early coal-fired boilers typically employed fixed or moving grates on which chunks of coal were burned to provide the heat needed to generate steam. The introduction of PC technology, in which coal is pulverized into a fine powder and injected into the furnace via burners, substantially increased the surface area of the fuel and improved the speed and efficiency of combustion. Major subsequent advances in PC boiler design came from economies of scale together with the increased steam pressure and temperature that became possible with the development of stronger metals (such as "superalloy" steels) and other technology improvements (Bugge et al. 2006). The resulting increase in boiler efficiency allowed utilities to produce more electricity with less fuel, thereby reducing the capital and operating costs. The following sections elaborate on the technology advancements in PC boiler size, steam temperature, steam pressure, and materials.

2.1.1 Advances in Boilers

The rapid unit cost reduction of new generating plants prior to the 1970s has been mainly attributed to economies of scale in all power plant components including the generator, turbine, and boiler. In the early 1900s, a 50 MW plant (considered large at that time) housed five 10 MW steam turbines and typically required 50–60 boilers to power the turbines. By the 1920s, the introduction of PC, together with improvements in boiler design that raised steam temperatures and boiler output, reduced significantly the number of boilers per plant. The subsequent development of single-boiler, single-turbine systems contributed to more rapid improvements in thermal efficiency and unit cost reductions (Viswanathan and Bakker 2001b).

2.1.2 Advances in steam temperature and pressure

Advancements in steam temperature and steam pressure have contributed greatly to PC plant efficiency improvements. The maximum steam temperature and pressure increased from about 260°C and 6.9 bar in 1900 to about 593°C and over 276 bar in the 1950s (Yeh and Rubin 2007). In the early 1960s, the utility industry's move toward larger units was accompanied by widespread adoption of supercritical boilers operating at 621°C and 310 bar. Of the nearly 11,000 MW in large units committed by U.S. utilities in 1962 and 1963, 70% were designed for supercritical steam pressure with either single or double reheat (Yeh and Rubin 2007). Reheat refers to the process of passing steam that has already been through the

turbine back through the boiler to increase the thermal efficiency; this may be done multiple times depending on the design of the boiler and the turbine. During the late 1960s and early 1970s, boiler tubes on supercritical units started to experience metal fatigue and creep, and scale deposits from boiler walls induced greater corrosion and erosion damage in the boiler, turbine nozzles, and other parts of the plant. As a result, the availability of these plants dropped and they became more costly to operate. The inability at that time to improve the metallurgy of boilers and turbines led the utility industry to retreat from supercritical units to the more reliable subcritical units (Bugge et al. 2006; Yeh and Rubin 2007). Not until roughly 20 years later did utilities in Europe and Japan begin to adopt improved supercritical units (Figure 2.3).

2.1.3 Advances in materials

In the mid-1930s, metallurgical progress made available superheater tubing and turbine parts that allowed steam temperatures to be raised to 496°C, thus increasing plant thermal efficiency to 26% (Yeh and Rubin 2007). The subsequent development of superalloys that resisted metal fatigue and cracking allowed engineers to design boilers for still higher temperatures and pressures, culminating in the development of supercritical boilers that began service in 1957 (Viswanathan et al. 2006). The introduction in the 1950s of the 0.5CrMoV, 1.25Cr0.5Mo and 2.25Cr1Mo ferritic steels allowed an increase in steam temperature from about 450°C to 540-568°C with a corresponding increase in thermal efficiency. For operations at even higher temperatures (i.e. above 568°C), the use of new high strength austenitic steels (such as the German 17Cr13NiMoN) could have offered a solution but this was not feasible because these steels have:

- high coefficient of thermal expansion
- low thermal conductivity
- higher cost than ferritics
- poor fatigue behaviour
- they are difficult to inspect by Non-Destructive Examination (NDE) methods.

At that time, most engineers believed that the extra cost of special alloys would be compensated for by the fuel savings from more efficient

supercritical boilers. However, the sustained material problems noted above led to lower availability and higher maintenance costs, which ended the use of supercritical units in the U.S. by the early 1980s. Attention therefore turned to the 9Cr1Mo and 12Cr steels in the search for ferritic steels for superheater and steam pipework components that could withstand operation at up to 600°C and beyond. Originally developed for the chemical process industries, 9Cr1Mo bainitic steels evolved into the ASTM P9 that has been used for creep resistant tubing in power plants at temperatures up to around 540°C. Steel P91 is a martensitic version of grade P9 which contains micro-alloying additions of vanadium, niobium, and nitrogen. P91 was originally developed during the 1970s by Oak Ridge National Laboratory (ORNL) in the USA. This steel was approved by ASTM Standard A213 as T91 for tubing in 1983. In 1984, ASTM Standard A335 approved Grade 91 material as piping steel and on-site testing began in the United States, Canada, and Europe. P92 was originally developed by Nippon Steel as NF616, being approved by ASTM as standard A213 T92 for tubing in 1994 and by ASTM as standard A335 P92 for piping steel in 1994. The material is included in EN 10216-2 under the designation X10CrWMoVNb9-2. P92 was developed to give a material with higher strength than P91. Exploitation of P92 steel began in the late 1990s with a small number of installations. Use of the material is increasing now that further experience has been gained in the fabrication and use of this steel. Grade 92 steel variations are designated as T92 for tubing, P92 for piping, and F92 for forgings. Tubing refers to relatively thin-walled components (typically 6 - 8mm wall thickness) that are used for heat transfer purposes; piping refers to relatively thick-walled components (typically 25 mm or greater wall thickness) used for the transfer of superheated steam to the turbine.

The only unit using P92 in the USA is the main-steam pipe in the 530 MW, Weston 4 power plant of Wisconsin Public Service Corp. which began operating on June 30, 2008 (steam temperature 585°C) although several such units (for example main-steam pipe in Comanche 3 and John W. Turk (610°C)) are now being planned as a result of the success of units operating in Europe and Japan since the late 1990s (Yeh and Rubin 2007). According to Vallourec & Mannesmann Tubes (V&M TUBES), a leading supplier of P92 steel, between 1990 and 2005, they delivered approximately 1000 tonnes of T/P92 all over the world. Since 2005 they

have delivered a further 79,000 tonnes, mainly to new projects in Germany and Asia, with 24 large power generating units (400 MW+) using V&M P92 in Europe, two in the USA, 14 in Asia (excluding China) and 77 in China. Other manufacturers report similar increases in demand between 2000 and 2012 with China representing the largest uptake for P92 due to the large number of new fossil-fired plants being constructed.

New materials, such as nickel-based superalloys and further developed steels, are expected to increase steam temperature beyond 760°C and pressures up to 345 bar, which is expected to increase plant efficiency beyond 45% within a decade (Bugge et al. 2006).

2.2 Principles of Creep

As has already been mentioned, creep failure of components is a major barrier to the development of super-critical and USC power plants. Creep describes the material deformation occurring as a result of long term exposure to stress at a level that is lower than the yield stress or ultimate strength of the material and at a temperature greater than 0.4 of the absolute melting temperature T_m. This creep strain is thermally activated and is a function of stress, temperature, time and material properties and eventually leads to failure. Creep is a time dependent deformation process where failure does not occur suddenly upon loading; rather the material irreversibly strains over a period of time until failure occurs (Evans 1984; Evans and Wishire 1985).

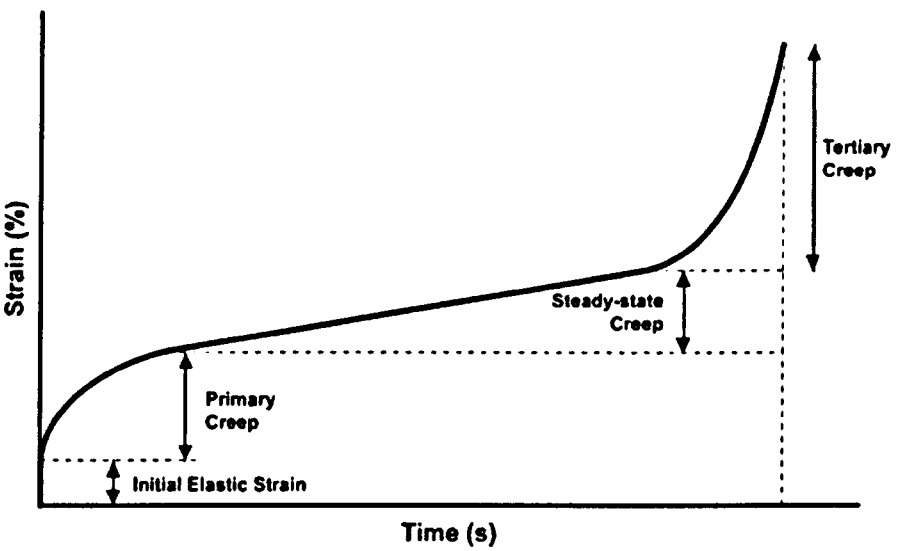

Figure 2.4 Schematic of a high temperature creep curve at constant stress and temperature (Evans and Wishire 1985)

Figure 2.4 shows a typical creep curve demonstrating the variation of creep strain with time when a material is subjected to a constant stress σ_a. The three stages during creep are the primary (transient), secondary (steady state) and tertiary (rupture) stages. During primary creep, after the initial strain on loading, the creep rate gradually decreases to a constant value. The strain is a combination of elastic and plastic deformation, and the increase in dislocation density results in a decreased creep rate. In secondary creep, the rate of strain hardening is balanced by the rate of dislocation recovery, so the creep strain rate is constant and reaches the minimum creep rate, hence the steady-state. Creep here can be governed by two creep mechanisms, namely dislocation creep and

diffusional creep. In the tertiary stage, the strain rate sharply increases and causes the formation of creep damage voids within the material. This voiding causes an increase in the local stress within the component which further accelerates the strain eventually leading to the final rupture. As creep is also dependent upon material properties, the primary stage may sometimes be absent or inverted, and the extent of the tertiary stage may be limited in brittle materials and extensive in ductile materials (Evans 1984).

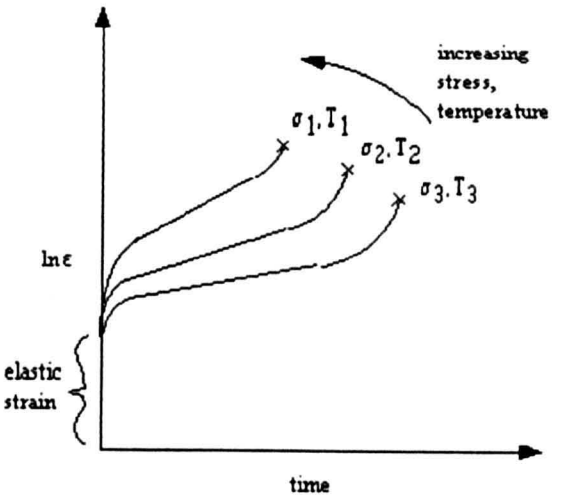

Figure 2.5 Effect of temperature and stress on the strain vs time creep behaviour (Evans 1984)

The time from the first application of stress to final rupture is termed the creep failure life at a particular stress and temperature, while the total strain along the stress axis after creep rupture is the total elongation. Figure 2.5 demonstrates the importance of stress and temperature on the creep curve. As stress and temperature increase, so does the minimum creep rate; accordingly, the creep failure life decreases.

The relationship between creep strain rate ($\dot{\varepsilon}$) and temperature (T) is expressed using the Arrhenius law, as shown in Equation 2.1 (Evans and Wishire 1993), where A is a material-dependent constant, Q_c is the activation energy for creep which is constant for a given creep mechanism, R is the universal gas constant and T is the absolute temperature in Kelvin.

$$\dot{\varepsilon} = A\, e^{\left(-\frac{Q_c}{RT}\right)}$$

Equation 2.1

Norton's law, Equation 2.2, describes the relationship between steady state creep rate $\dot{\varepsilon}$ and stress σ, where n is the creep index.

$$\dot{\varepsilon} \propto \sigma^n$$

Equation 2.2

The parameter of greatest significance in controlling the creep life is the steady state creep rate $\dot{\varepsilon}$ (see Figure 2.5 where $\dot{\varepsilon}$ is the slope of the secondary stage), due to its extended duration. Life calculations use the steady state creep rate as $\dot{\varepsilon}$ varies with both stress and temperature as shown in Equation 2.3.

$$\dot{\varepsilon} = u(\sigma)\, v(T)$$

Equation 2.3

By substituting *v(T)* from Equation 2.1 and *u(σ)* from Equation 2.2, we get the power law relationship (Equation 2.4) of $\dot{\varepsilon}$ expressed as a function of σ and T (Evans and Wishire 1993).

$$\dot{\varepsilon} = A\, \sigma^n e^{\left(-\frac{Q_c}{RT}\right)}$$

Equation 2.4

Materials may creep by several mechanisms at elevated temperatures depending on the stress and temperature. Diffusion creep is controlled by volume diffusion (Nabarro-Herring creep) or grain boundary diffusion (Coble creep); dislocation creep is controlled by volume diffusion (high temperature power law creep) or by pipe diffusion (low temperature power law creep). The creep rates of all the mechanisms are represented by the following general equation (Equation 2.5):

$$\dot{\varepsilon} = \dot{\varepsilon}_0 \left(\frac{\sigma}{G}\right)^n d^p D$$

Equation 2.5

where $\dot{\varepsilon}_0$ is a material constant characteristic of the mechanism and material, *d* is the grain size, *p* is the grain size exponent, *G* is the shear modulus and *D* is the diffusion coefficient relevant to the mechanism. The values of *n*, *p* and *D* are typical of each creep mechanism and are listed in Table 2.1.

Table 2.1 Stress exponent n, grain size exponent p and diffusion mechanism for each creep mechanism (Abe 2008)

Deformation mechanism	*n*	*p*	*D*
Dislocation Creep			
Low temperature power law creep	5-7	0	D_p
High temperature power law creep	3-5	0	D_l
Diffusion creep			
Coble creep	1	3	D_{gb}
Nabarro-Herring creep	1	2	D_l

D_l, D_p and D_{gb} indicate the diffusion mechanisms of lattice, dislocation pipe and grain boundary diffusion, respectively. The four creep mechanisms are independent of each other and the creep strain produced by each mechanism contributes additively to the total creep strain; therefore, the mechanism which results in the highest value of $\dot{\varepsilon}$ dominates. The different creep mechanisms can be represented using a deformation mechanism map as shown in figure 2.6. The diffusion creep mechanisms (Coble and Nabarro-Herring creep) appear in the lowest stress range while the dislocation creep mechanisms (high and low temperature power law creep) appear in the intermediate stress range. A dislocation glide mechanism without the aid of diffusion takes over the role of plastic deformation above the athermal yield stress (σ_a, the stress at which dislocations are able to move without diffusion). Creep rates of both dislocation mechanisms are independent of grain size, but the diffusion creep mechanisms see an increase in creep rate with decreasing grain size. The steel P92 is designed to operate at high temperatures and stresses where high temperature power law creep is the dominant mechanism.

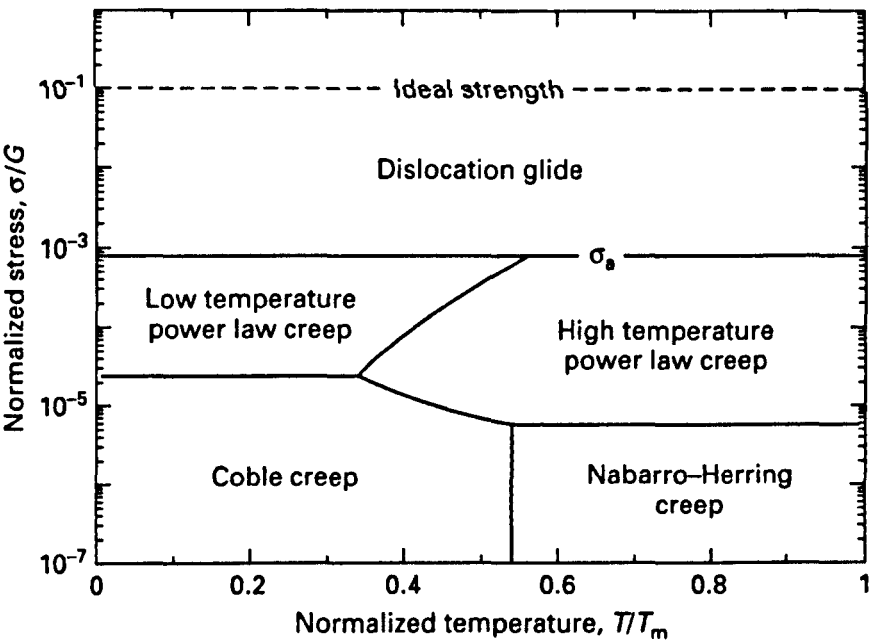

Figure 2.6 Schematic drawing of a deformation mechanism map. T_m is the materials melting temperature (Abe 2008)

2.3 Development of Power Plant Steels

The constraints that are currently placed on power generation plant in terms of environmental impact and economics have focussed attention on the development of high efficiency, low emission systems.

The process of steam generation to drive turbines is the same for supercritical and ultra-supercritical plants with the difference coming from the operating conditions (and improved thermal efficiency) of ultra-supercritical plants, while the advantage that both have over subcritical plants is the absence of a steam drum as the high pressure and temperature allows water to rapidly turn to steam rather than being re-circulated as required in a subcritical plant. Ultra-supercritical pressure refers to steam pressure exceeding conventional supercritical pressure steam conditions, i.e., 24 MPa with a superheater outlet temperature of 538°C, but can be more accurately defined as representing turbine inlet steam conditions of at least 24 MPa for main steam pressure and a temperature of at least 565°C for main steam and reheat steam (see Figure 2.7 for a process diagram of the supercritical/USC power plant). Such elevated steam conditions increase plant efficiency and thereby contribute to improved resource and energy conservation, as well as environmental protection. Power plants incorporating these steam conditions had already been constructed in the US and Europe by the late 1950s. While the improvements in ultra-supercritical pressure power plant are not obvious merely from steam conditions and plant specifications, there is in fact a very major technological difference between modern plants and those of a generation ago. Specifically, the older plants were designed and constructed as base load plants without the load-adjusting functions considered essential for the plants being used today. Base-load refers to plants that are almost continuously generating electricity at or near their design conditions such as steam pressure and power output of the turbine and generator. Load-adjusting (or plant cycling) refers to a mode of operation where power plants are frequently required to either start-up/shut-down or adjust the output power to meet demand in power grids that increasingly give priority to energy generated by renewables. Plant cycling is a problem for older plants as they were typically designed to experience 1-2 full cycles in a year but are now experiencing hundreds of cycles per year creating problems with thermal fatigue. Thus, elevated pressure and temperature requirements formerly met through the use of

large quantities of austenitic steels for heavy, thick-walled components such as headers, piping, and turbine equipment in the older generation of ultra-supercritical pressure power plants now have potential problems from thermal stress due to the larger thermal expansion coefficient of the austenitic steels. For steam power plants to be capable of responding to changes in electricity demand, or for plants undergoing frequent start and stop cycles, Sliding pressure operation is a method of controlling the MW output by a power station by reducing the pressure of steam going to the turbines. This is done by changing the heat input in the boiler, often in a short space of time, thus introducing frequent changes in temperature; this type of operation causes problems if using austenitic steels. It is preferable to use ferritic steels with their smaller coefficients of thermal expansion for heavy, thick-walled components in order to reduce thermal stresses during this mode of operation. Accordingly, the heat resistance capability of ferritic steels is the major determinant of steam conditions (Masuyama 2001).

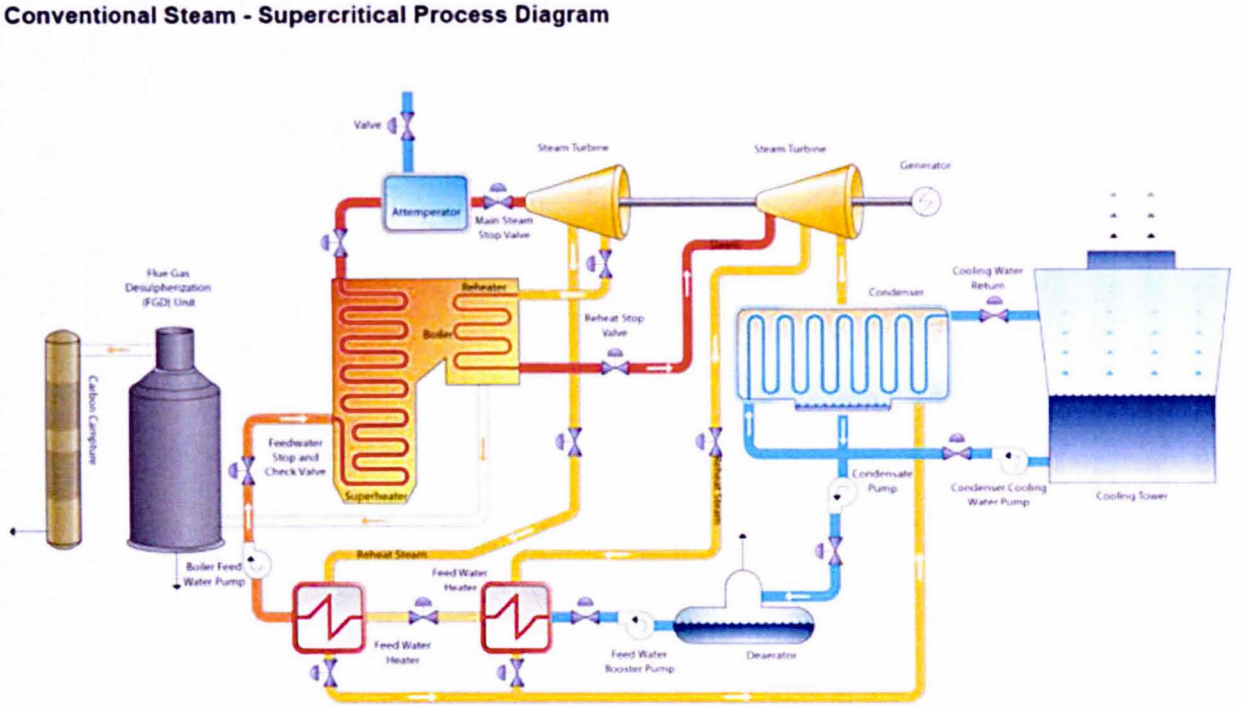

Figure 2.7 Process diagrams of supercritical steam generating power plant (http://www.flowserve.com/Industries/Power-Generation/Conventional-Steam).

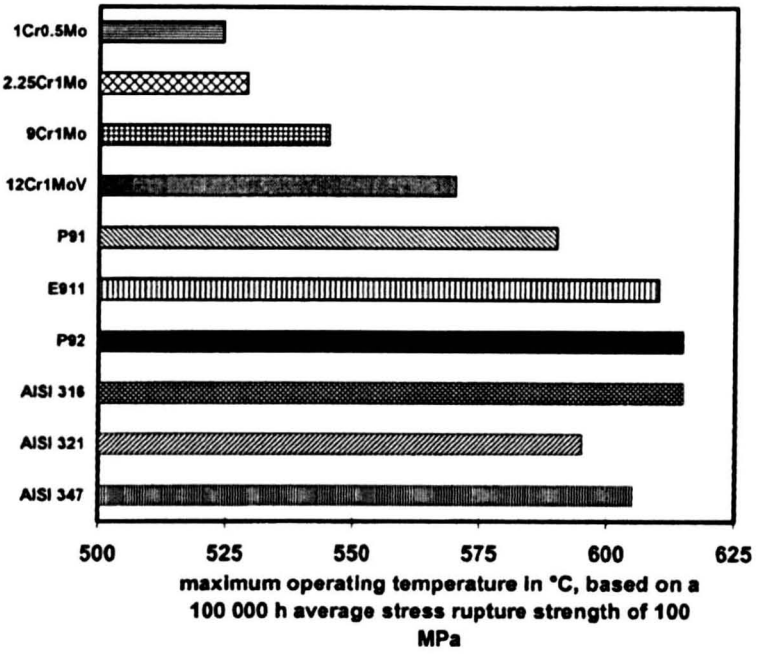

Figure 2.8 Stress rupture strengths of the currently used and the newly developed power station steels (Ennis and Czyrska-Filemonowicz 2003)

The next generation of steam power plants should be capable of operating with steam at 625–650°C, to enable thermal efficiencies of around 45% to be achieved. The increasing operating temperatures and pressures impose increasingly stringent requirements on the materials of construction (Viswanathan and Bakker 2001a, b; Viswanathan et al. 2006). High chromium ferritic/martensitic steels such as P91, E911 and P92 (Shibli 2008; Vaillant et al. 2008) have been developed for advanced steam power plants, in particular those sections requiring thick walled pipe to transport supercritical steam as shown by the thick red pipe sections in Figure 2.7. In Figure 2.8, the stress rupture strengths of the currently used and the new power station steels are compared on the basis of the maximum service temperature for a 100,000 h stress rupture strength of 100 MPa (Ennis and Czyrska-Filemonowicz 2003). It can be seen that the maximum service temperature increases with increasing complexity of the steel composition and the more highly alloyed steels have sufficient 100,000 h stress rupture strength to be considered for application at temperatures in excess of 600°C. Indeed, the new high chromium steels have similar stress rupture strengths to austenitic stainless steels. There are several reasons for the reluctance to use the austenitic steels; obviously the increased cost of the steel with the high chromium and nickel contents is a disadvantage but there are technical problems because the thermal expansion coefficient of austenitic materials is at least 50% higher than that of ferritic steels.

This means that care has to be taken during cooling and heating to avoid excessive thermal stresses that can lead to fatigue failures. Steels with a ferritic/martensite microstructure have good thermal conductivity, low coefficient of thermal expansion and a high resistance to thermal shock (Cerjak and Letofsky 1998) which make them more attractive for high temperature applications then austenitic steel.

2.3.1 Types of Heat Resistant Steels

Various kinds of heat resistant steels are separately used in power plants according to their specific purposes. They are generally classified into ferritic steels and austenitic steels, but are then further sub-divided. Ferritic steels include carbon steels (C–Mn, etc.), low alloy steels (0.5%Mo,2.25%Cr–1%Mo), intermediate alloy steels (5–10%Cr) and high alloy steels (12% Cr martensitic steels and 12–18%Cr ferritic steels of the AISI400 series); steels with 9-12%Cr are also usually considered a class due to their martensitic microstructure. Austenitic steels include 18%Cr–8%Ni steels and 25%Cr–20%Ni steels of the AISI300 series, 21%Cr–32%Ni steels such as Alloy 800H, and Cr–Mn steels of the AISI200 series (Masuyama 2001). Figure 2.9 shows the chemical compositions of typical heat resistant steels used under stresses in the Fe–Cr–Ni ternary phase diagram (Masuyama 2001). Ferritic steels generally do not contain nickel, and, because steels with chromium compositions of 2%, 9% and 12% are particularly high in strength, they are widely used. Among austenitic steels, materials in commercial use are positioned along the boundary between the full γ phase and the γ phase containing α and/or σ. The full γ phase steels contain relatively high Ni content, the high cost of which is typically offset by high creep strength. In contrast, the γ phase steels with α and/or σ, although less costly, require some improvement to elevate the creep strength. In order to facilitate a better understanding of the different types of steels, Figure 2.10 shows schematically illustrated microstructures of ferritic and austenitic heat resistant materials. In both cases, material upgrades are illustrated from left to right, and the precipitates appearing therein change according to type.

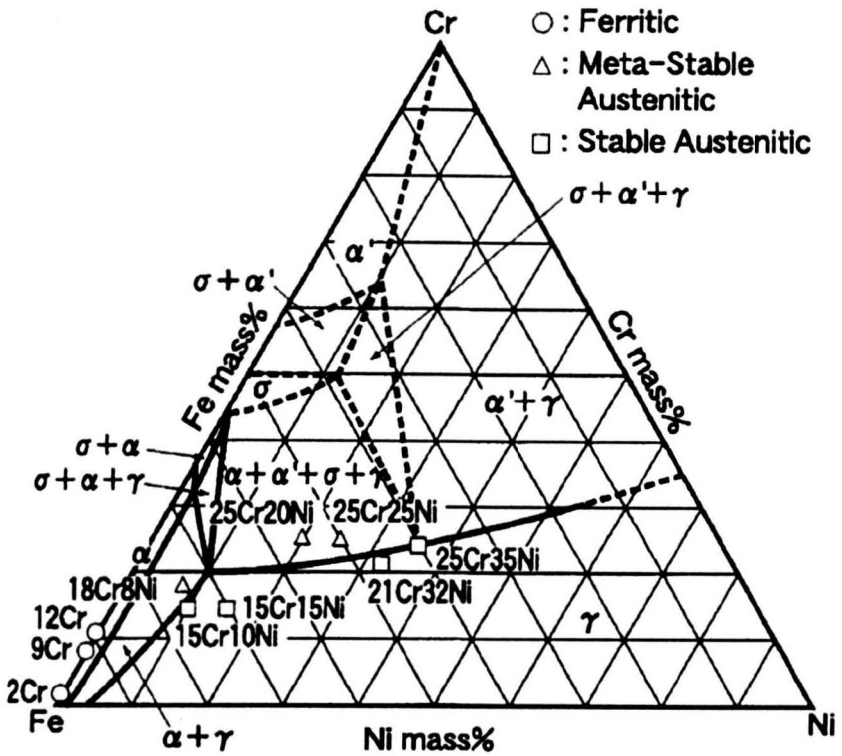

Figure 2.9 Compositions of heat resistant steels in Fe–Cr–Ni ternary phase diagram at 800°C (Masuyama 2001)

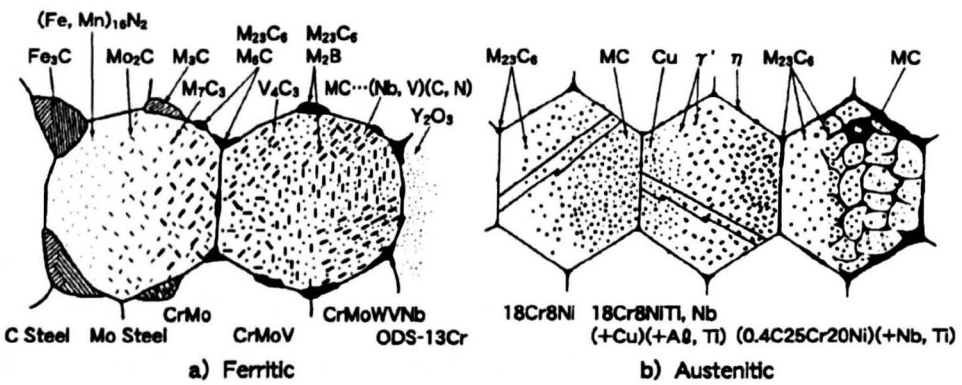

Figure 2.10 Schematic illustration of microstructures of ferritic and austenitic steels (Masuyama 2001)

2.3.2 The Alloy Design Concept

Heat resistant steels for practical application must be designed by considering their service conditions and environments, and by examining their various properties. However, when alloy design is performed based on modification of existing steels, oxidation and corrosion resistance as well as their general material properties are expected to be nearly equivalent to those of the original materials. Hence, chemical compositions and heat treatment conditions are examined in particular consideration of creep strength improvement. Figure 2.11 shows the concept of alloy design

for heat resistant steels to improve creep strength through the modification of existing steels. For ferritic heat resistant steels, research on 9–12%Cr system steels is fairly advanced, and approaches for the improvement of creep strength through solution strengthening, precipitation strengthening and microstructural stabilization have been adopted. These techniques are also applicable for the modification of Cr–Mo low alloy steels as well. On the other hand, chemical compositions of austenitic steels can be largely classified into the four categories shown in the figure, and solution strengthening and precipitation strengthening are designed specifically for each of these categories. 18%Cr–8%Ni steels based on Type 304 steels include Type 316 steels solution-strengthened through the addition of Mo, as well as Type 321 steels and Type 347 steels precipitation-strengthened through the addition of Ti or Nb. However, these materials were originally developed for chemical equipment, placing emphasis on corrosion resistance, but were not designed from the standpoint of creep strengthening. Accordingly, the further enhancement of precipitation strengthening by means of "under-stabilizing" carbon and/or composition design for improved creep strength is used. 15%Cr–15%Ni or 21%Cr–30%Ni steels with full γ phase structure are capable of high creep strength in is the as-received condition (with no special need for alloying for precipitation strengthening of solution strengthening), although they are costly because of their high nickel content. Steels with chromium levels of 20% and over are likely to have excellent oxidation and corrosion resistance, but a costly nickel content of at least 30% is required to maintain a full γ structure. Nevertheless, low-cost, high strength, highly corrosion-resistant austenitic steel can be designed by adding nitrogen of about 0.2%, which reduces the nickel content necessary to maintain a full γ structure as nitrogen is also a strong austenite stabiliser, and by combining the strengthening mechanisms as described above (Masuyama 2001).

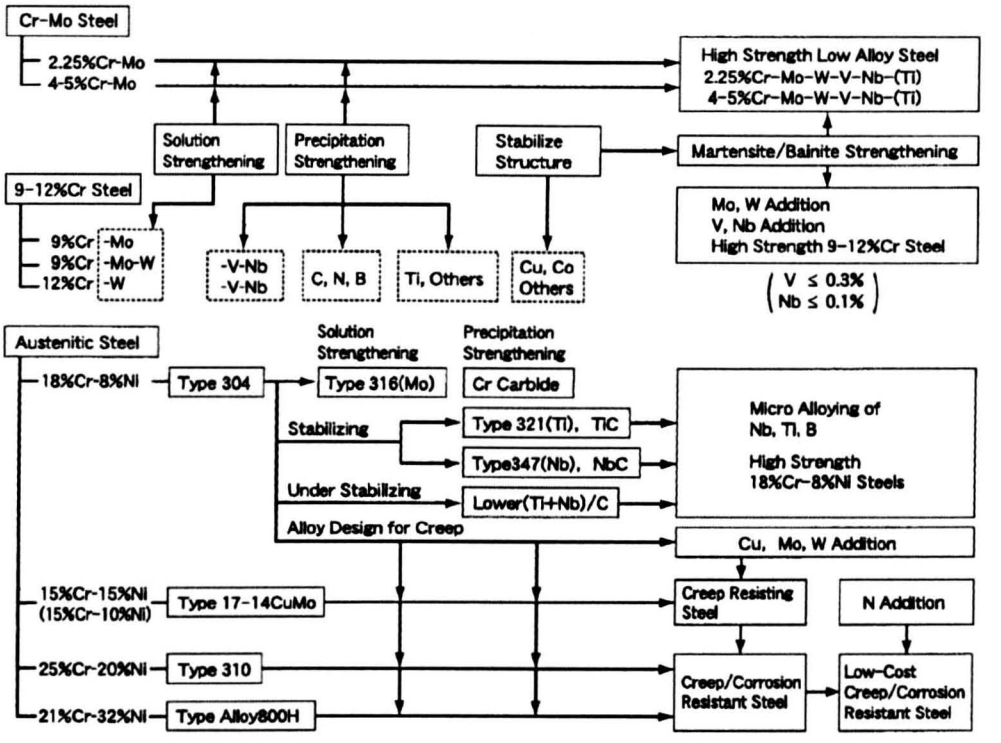

Figure 2.11 General concept of alloy design for heat resistant steels (Masuyama 2001)

Alloying Elements and Microstructure in 9-12%Cr Steels

Although the overall microstructures of the 9–12%Cr steels are quite similar for most compositions that have been developed, it is the compositional changes made over the years that have resulted in the improved properties as shown in Figure 2.12. The effects of the various alloying additions are outlined in the following discussion.

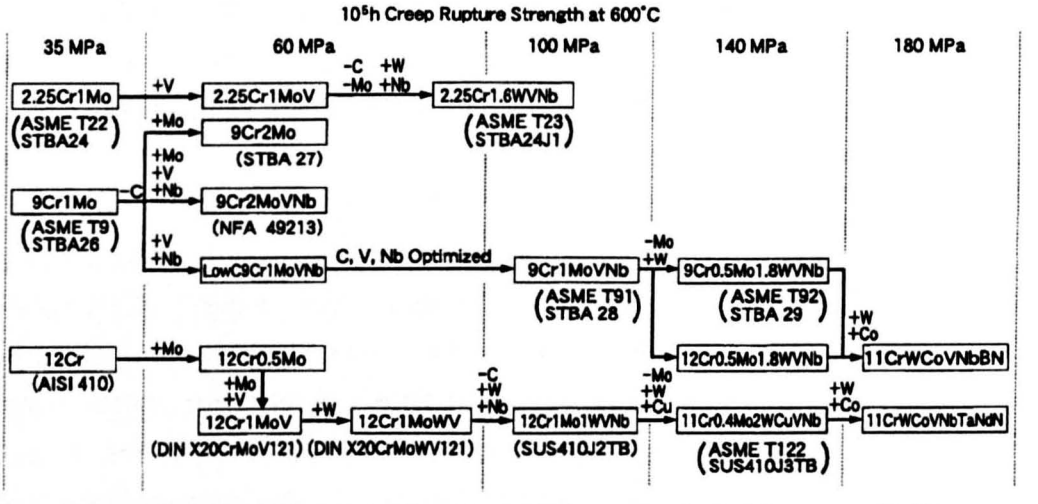

Figure 2.12 The development of ferritic steels for power plants (Masuyama 1999)

Chromium (Cr)

Chromium is a ferrite stabilising element that is generally added to steels for oxidation and corrosion resistance and is the main alloying element in P92 steel, where it also contributes to solid solution strengthening. However, the main strengthening effect is achieved by the precipitation of chromium-rich carbides from the solid-solution, which can impede the movement of dislocations and grain boundaries to increase creep strength of the steel. Chromium reacts with carbon to form carbides; the chromium rich carbides usually encountered in P92 steels are $M_{23}C_6$ which form during tempering and remain present throughout elevated temperature exposure. In steels containing nitrogen, chromium rich M_2X (Cr_2N) can also form under some conditions (Klueh 2005).

Molybdenum (Mo)

Molybdenum is a ferrite stabiliser and improves the creep properties of P92 steel by solid solution hardening, but can also be detrimental as it accelerates the growth of $M_{23}C_6$ carbides (Maruyama et al. 2001). In the tempered condition, molybdenum is in solid solution and provides solid-solution strengthening. However, the amount of the molybdenum must be limited to avoid the formation of δ-ferrite and the intermetallic Laves-phase. Klueh (Klueh 2005) stated that for structural steels being used at elevated temperatures, the Mo_{eq} (where Mo_{eq} = Mo + 0.5 W [wt%]) should not exceed 1%. If the steel has a Mo_{eq} greater than 1% when operating in the 600-650°C temperature range, the tendency for the intermetallic Laves-phase to form is increased, resulting in the removal of molybdenum from solid solution and a reduction in solid solution strengthening (Klueh 2005).

Tungsten (W)

Tungsten is used in P92 steels as a substitute for the higher level of molybdenum seen in steels from earlier generations such as P91. Like molybdenum, tungsten is a solid solution strengthener and its addition has been found to be effective in increasing high temperature creep strength. The strengthening effect of tungsten can be lowered dramatically during long time exposure due to the formation of the intermetallic Laves-phase during long time exposure at high temperatures. The limit of tungsten can also be defined using the aforementioned Mo_{eq} equation (Klueh 2005). It has been found that according to the tungsten precipitation behaviour, the

optimum tungsten content is around 1.8wt%; tungsten contents higher than 2wt% have been seen to accelerate the intermetallic Laves phase formation if the chromium content stays at 9 wt% (Hasegawa et al. 2000).

Vanadium and Niobium (V, Nb)

Vanadium and niobium are added to steels in order to promote the formation of fine, dispersed and thermally stable MX particles within grains. In P92, the MX precipitates (V or Nb = M, C or N = X) can be in the form of carbides MC, nitrides MN, or carbonitrides M(C, N) (Sourmail 2001). Although the density of MX particles is low in the common grades of high chromium ferritic steel, the particles are necessary in maintaining a fine subgrain structure in the steels over extended service at high temperature and to improve creep strength of the steel (Abe et al. 2004; Abe et al. 2007; Sawada et al. 2001a, 2003; Yin and Jung 2009). A comparison (Maruyama et al. 2001) was made among stress-rupture curves of three ferritic steels: 9Cr-1.8W-0.4Mo-VNb steel (0.16V, 0.06Nb, 0.11C and 0.036N) with tungsten and MX, 9Cr-1Mo-VNb steel (0.22V, 0.09Nb, 0.10C and 0.051N) with MX but without tungsten, and 9Cr-2W steel (0.08C) with tungsten but without MX particles. Although the 9Cr-1Mo-VNb steel contained larger amounts of vanadium, niobium and nitrogen than the 9Cr-1.8W-0.4Mo-VNb steel, the former was inferior to the latter in creep rupture strength because of the absence of tungsten. However, the rupture life of 9Cr-2W steel was substantially shorter than those of the 9Cr-1Mo-VNb steel in spite of the tungsten addition, and the important role of the MX was seen as a major factor in determining these properties.

Nitrogen and Aluminium (N, Al)

Nitrogen plays an important role in increasing the creep life of steel: it allows the precipitation of strengthening nitrides in the form of MX, while nitrogen in solid solution has a greater strengthening effect than carbon (Sourmail 2001). If the P92 steel contains aluminium, it is also possible for AlN to form. The AlN removes nitrogen and thus reduces the amount of vanadium nitride particles in the system leading to a reduction in creep strength (Gomez et al. 2009). As such, 9-12%Cr steels should have a very low aluminium content or high N:Al ratio. In this way, aluminium does not combine with a significant part of the nitrogen and the precipitated volume of vanadium nitrides is not significantly diminished.

Boron and Phosphorus (B, P)

Boron segregates to austenite grain boundaries during cooling after austenitization. During tempering, boron diffuses into prior austenite grains and is incorporated in growing $M_{23}C_6$ precipitates. Boron incorporated in $M_{23}C_6$ reduces their coarsening rate by reducing the interfacial energy of this phase (Abe et al. 2004; Czyrska-Filemonowicz et al. 2003; Golpayegani et al. 2003). Phosphorus can also segregate to the surface of $M_{23}C_6$, and a small amount of phosphorus has been found in the intermetallic Laves-phase (Ennis et al. 1997).

Carbon

Carbon is a strong austenite stabiliser with a relatively large solubility in austenite, but a small solubility in ferrite. It is mainly added to P92 for the formation of the strengthening phases $M_{23}C_6$ and MX (Ennis et al. 1998).

Nickel and Manganese (Ni, Mn)

Nickel and manganese are austenite stabilisers, lowering the ferrite to austenite transformation temperature A_1. The main reason for adding them is to ensure 100% austenite formation (without δ-ferrite) during the austenitization treatment and by lowering the temperature for transformation from austenite to ferrite, ensuring a 100% martensite structure when cooled (Knezevic et al. 2008). Nickel results in an increase in toughness of the steel, but at concentrations higher than 0.4 at%, it is responsible for significant coarsening of $M_{23}C_6$ (Yin and Faulkner 2003). Manganese decreases the coarsening rate of $M_{23}C_6$ at low concentrations; however, when its concentration reaches about 0.5 at%, it actually contributes to the coarsening of $M_{23}C_6$ (Helis et al. 2009). Manganese is also present in the steel in order to collocate with sulfur, and to increase the solubility of nitrogen in austenite (Sourmail 2001).

Microstructures of 9–12%Cr steels currently being developed or already commercially available generally consist of a single phase of tempered martensite, with just a few exceptions. High dislocation densities are generally found in this type of structure, being principally influenced by the tempering temperature. The dislocation density remains high when the tempering temperature is low, as in the case of turbine rotor steels. Figure 2.13 shows a representative microstructure observed through optical microscopy and transmission electron microscopy (TEM) of a typical 9–

12%Cr heat resistant steel. The tempered martensite is composed of numerous laths, and chromium carbides such as $M_{23}C_6$ precipitate along the lath boundaries and along the prior-austenite grain boundaries. Fine MX carbonitrides of (V, Nb)(C, N) coherently precipitate on the ferrite matrix in laths, and dislocation networks are formed along the lath boundaries or the sub-grain boundaries. It is considered that the creep strength of 9–12%Cr steels is closely associated with the stabilization of MX carbonitrides and the dislocation structures, and it is inferred that in tungsten-containing steels, strength rises by suppressing recovery and recrystallization of martensitic structures during creep.

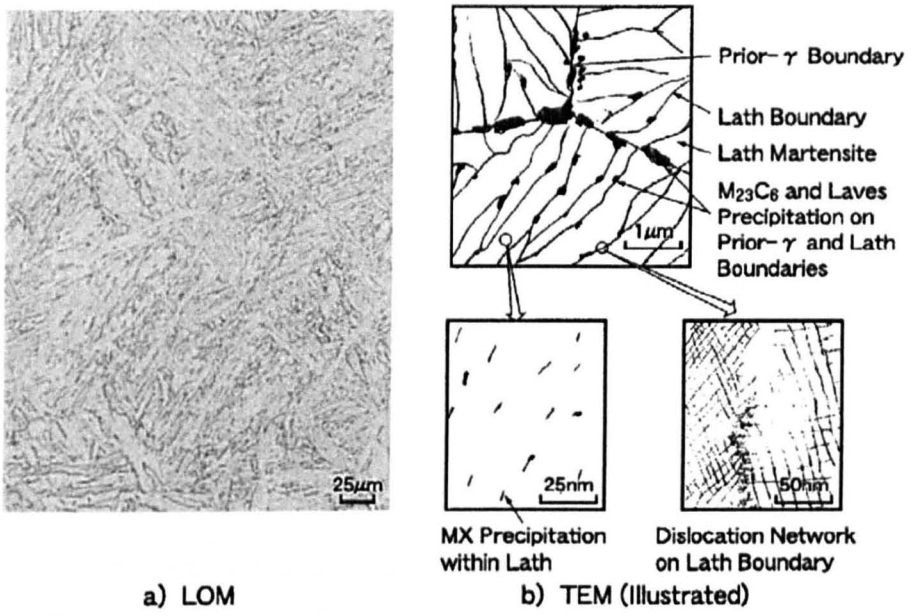

Figure 2.13 Typical microstructure of tempered martenstitc 9–12% Cr steel (Masuyama 2001)

2.3.3 Evolution of microstructure and material properties during creep

2.3.3.1 Precipitation

The high strength of 9-12%Cr steels is due to a chemical composition designed to produce 100% austenite during austenitization by balancing the austenite and ferrite stabilizers, while forming 100% martensite during the quench (Klueh 2005). The creep strength of the material is also determined by elements which contribute to solid solution strengthening and precipitation strengthening; in the latest steels, solid solution strengthening is provided by tungsten while the main precipitates are $M_{23}C_6$ and MX (Anderson et al. 2003). Dislocation motion is an important mechanism of creep and the precipitates dispersed in the material can act as obstacles for dislocation motion. For the dislocations to move around

the precipitates, a higher stress must be applied compared to the stress it takes to move through the bulk material. Creep deformation proceeds after the dislocations have overcome the additional stress imposed by the precipitates, and therefore materials with large numbers of precipitates normally possess higher creep strength.

The precipitates $M_{23}C_6$ and MX are described in detail in section 2.4.3. $M_{23}C_6$ is the dominant precipitate in P92 steel and improves creep strength in the short term, though the strengthening effect is reduced at later stages due to coarsening of the precipitates. The evolution of particle mean size d is described by the Ostwald ripening law (Orlova et al. 1998) as shown in Equation 2.6 where d_0 is the initial particle size at t=0 and k is the particle growth rate.

$$d^3 = d_0^3 + k.t$$

Equation 2.6

Creep strength is diminished by precipitate coarsening as it limits the effect that grain boundary precipitates have on subgrain growth. Large grain boundary precipitates can also act as the initial locations of creep cavitation, resulting in the onset of tertiary stage creep.

The minor precipitate MX that forms in the subgrain interior does not coarsen rapidly during creep. Klueh (Klueh et al. 2005) performed tests on 9-12%Cr steels which showed the presence of elements such as vanadium, niobium, and nitrogen gave an advantage in creep strength over steels without these elements where chromium and carbon levels were similar. Previous authors have also shown that MX precipitates based on molybdenum, niobium, vanadium, titanium or tungsten are resistant to coarsening (Nawrocki et al. 2000; Tamura et al. 2003). While $M_{23}C_6$ at grain boundaries coarsen during creep with reducing numbers and greater inter-particle spacing, MX precipitates in the subgrain interior increase primarily in number with time at a given temperature (Klueh et al. 2005). In contrast, $M_{23}C_6$ precipitates within martensite laths decrease in size and number, indicating that they dissolve and re-precipitate at the grain boundary (Anderson et al. 2003). Ongoing MX precipitation offsets some of the loss in creep strength due to $M_{23}C_6$ coarsening, but eventually the reduction overwhelms the strengthening effect of MX, leading to creep cavitation and material deformation.

2.3.3.2 Recovery of martensite and dislocations

Well developed martensite laths (subgrains) with low dislocation density in their interiors are important characteristic features of long-term creep exposed materials (Czyrska-Filemonowicz et al. 2003). As shown in Figure 2.14, with the progress of creep deformation, the subgrain width increases and free dislocation density decreases.

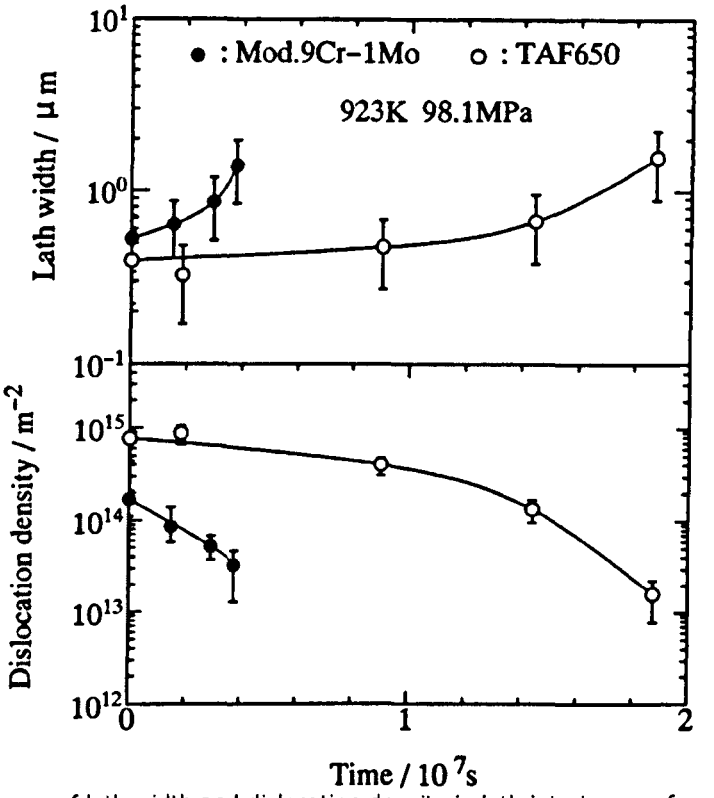

Figure 2.14 Change of lath width and dislocation density in lath interior as a function of creep duration (Sawada et al. 1999)

Sawada (Sawada et al. 1999) also looked at the effect of tungsten on lath recovery and found that the growth of lath width and the annihilation of dislocations in the lath interiors are slower in tungsten containing steel. Accumulation of creep strain is suppressed because of the slow recovery of its lath structure which results in the lower creep rate and the higher creep rupture strength of the tungsten containing steels.

High dislocation density in tempered martensite structures also contributes to creep strength. During creep, dislocations move by glide and climb resulting in the deformation of material. If the stress is high enough, dislocations can cut or loop obstacles such as precipitates, grain boundaries and other dislocations. However, coarsening of precipitates and martensite lath boundaries during creep (such as increasing spacing or subgrain width) make dislocation movement easier.

2.3.3.3 Hardness

Hardness can give an indication of the creep strength of materials. Its well established relationships with other parameters such as yield stress, elongation and fatigue make hardness evaluation useful in obtaining plastic flow and strain hardening parameters associated with creep of materials (Kohlhofer and Penny 1996).

It has been shown that hardness reduces with increasing temperature and thermal exposure duration. The effect of stress on hardness degradation has also been investigated (Watanabe et al. 2004) where it was shown that a stress-aged specimen has a lower hardness than a solely thermally aged specimen, indicating that stress has a significant effect on hardness degradation during creep. Both carbide coarsening and dislocation recovery have been regarded as the sources of the hardness difference.

2.4 P92 Power Plant Steel

2.4.1 Compositions of P92 Parent Material

P92 is a ferritic 9Cr-1.75W-0.5Mo steel micro-alloyed with vanadium and niobium, and with controlled boron and nitrogen content. In modern super-critical steam power plants, P92 allows higher operating temperatures and pressures to be employed and therefore higher efficiencies can be achieved. European experience has shown that P92 is suitable for components outside the boiler (i.e. pipes and headers) at steam temperatures up to 625°C (Richardot et al. 2000a).

The chemical composition of grade 92 specified by ASME standards is listed in Table 2.2, along with various reported compositions of P92 from the literature. It can be seen from the difference between the literature average and the ASTM mid-point that some elements are consistently used at either the upper or lower limits of the ASTM specification. Manganese is routinely used at an average of 48% above the ASTM mid-point while nickel is 31% below. As is described in section 2.3.3, both manganese and nickel have the same general effect, so manganese may be used in greater quantities in preference to nickel as it is less expensive. Aluminium is generally kept very low, if it is present at all, as it forms AlN which removes the amount of nitrogen available for the precipitation of useful phases (see 2.3.3). Boron is also generally present in low quantities, although in some cases, it is not reported to be present even though the ASTM states a minimum of 0.001wt%. The greatest standard deviation is seen in the alloying element which is present in highest concentration (chromium), possibly affecting the amount of the beneficial phase $M_{23}C_6$ present and thereby causing a variation in the mechanical properties of different P92 steels.

Table 2.2 ASTM composition of P92 and reported compositions of P92 from the literature

Name	Composition (wt%)														
	C	Mn	P	S	Si	Cr	W	Mo	V	Nb	N	B	Al	Ni	Fe
ASTM min	0.070	0.030				8.500	1.500	0.300	0.150	0.040	0.030	0.001			BAL
ASTM max	0.130	0.600	0.020	0.010	0.500	9.500	2.000	0.600	0.250	0.090	0.070	0.006	0.040	0.400	BAL
ASTM average	0.100	0.315	0.010	0.005	0.250	9.000	1.750	0.450	0.200	0.065	0.050	0.004	0.020	0.200	BAL
M. Hattestrand et al. (1998)	0.110	0.460	0.008		0.040	8.960	1.840	0.470	0.200	0.070	0.050	0.001		0.060	BAL
P. J. Ennis et al. (1997)	0.120					9.100	1.800	0.500	0.200	0.060	0.040				BAL
P. J. Ennis et al. (2000)	0.120	0.470	0.011	0.006	0.020	9.070	1.780	0.460	0.190	0.063	0.043	0.003	0.002	0.060	BAL
K. Sawada et al. (2001)	0.110	0.450	0.012	0.003	0.100	8.820	1.870	0.470	0.190	0.060	0.047	0.002	0.010	0.170	BAL
Y.F. Yin et al. (2003)	0.110	0.460	0.008		0.040	8.960	1.840	0.470	0.200	0.070	0.050	0.001		0.060	BAL
K. Sawada et al. (2002)	0.110	0.450	0.012	0.003	0.100	8.820	1.870	0.470	0.190	0.060	0.047	0.002	0.010	0.170	BAL
K. Rodak et al. (2003)	0.094	0.460			0.210	8.840	1.720	0.470	0.210	0.070				0.260	BAL
Wachter et al. (1995)	0.124	0.470	0.011	0.006	0.020	9.070	1.780	0.460	0.190	0.063	0.043	0.003	0.002	0.060	BAL
B S Lim et al. (2005)	0.100	0.480	0.017	0.006	0.220	9.110	1.750	0.470	0.180	0.056	0.041	0.002	0.010	0.180	BAL
C S Jeong et al. (2005)	0.100	0.480	0.017	0.006	0.220	9.110	1.710	0.470	0.180	0.056	0.0405	0.0029	0.010	0.180	BAL
R Sugiura et al. (2007)	0.090	0.470	0.010	0.001	0.160	8.720	1.870	0.450	0.210	0.060	0.050	0.002		0.180	BAL
B Kim et al. (2008)	0.100	0.480	0.017	0.006	0.220	9.110	1.750	0.470	0.180	0.056	0.041	0.002	0.010		BAL
Literature average	0.107	0.466	0.012	0.005	0.123	8.974	1.798	0.469	0.193	0.062	0.045	0.002	0.008	0.138	BAL
Percentage difference between ASTM & Literature average	7%	48%	23%	-8%	-51%	0%	3%	4%	-3%	-5%	-10%	-40%	-61%	-31%	
Standard Deviation (literature)	0.011	0.011	0.004	0.002	0.086	0.141	0.059	0.012	0.011	0.005	0.004	0.001	0.004	0.072	

2.4.2 Microstructural Features of P92 Steel

Tempered martensite steels are hardened by dislocations, solutes and precipitates. In P92, normalization produces a martensitic structure with a high dislocation density within the martensite laths. The dislocations are introduced during martensitic transformation which involves severe plastic deformation. The martensitic transformation and subsequent annealing forms subgrains within the prior austenite grains. The subgrains are bounded by low-angle boundaries (dislocation networks) as well as high-angle boundaries (Chilukuru et al. 2009). Precipitates at the subgrain boundaries are essential in stabilizing the subgrain structure against coarsening and recrystallization (Abe 2004), while precipitation in the bulk increases the deformation resistance of the subgrain interiors (Yoshizawa et al. 2009). Figure 2.15 shows the martensitic structure of a 9Cr steel after tempering, with the distribution of the two main precipitates $M_{23}C_6$ and MX indicated (Abe et al. 2007).

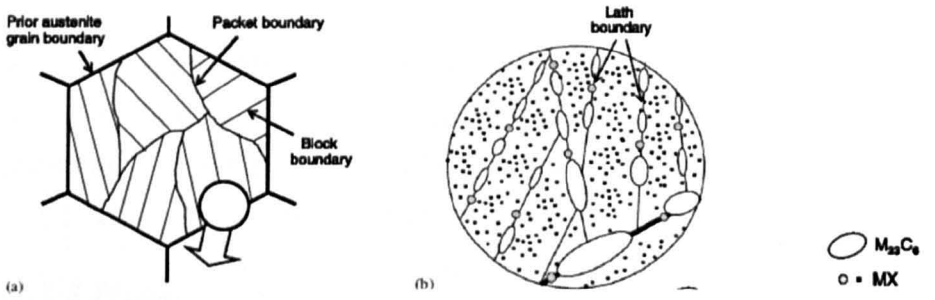

Figure 2.15 Illustration of martensitic 9Cr steel after tempering: (a) subgrain structure; (b) distribution of $M_{23}C_6$ and MX (Abe et al. 2007)

Dispersion strengthening of the alloy is inversely proportional to the mean inter-particle distance and proportional to their volume fraction (Abe et al. 2007). Therefore, optimal creep strength of the steel can be obtained by a dispersion of fine and thermally stable precipitate particles combined with enough solid solution strengthening. Zielinska-Lipiec (Zielinska-Lipiec and Czyrska-Filemonowicz 2007) studied the effect of normalization and tempering on the microstructure of P92 (see Table 2.2 for composition) and the results of their work can be seen in Table 2.3. If the optimal creep strength is given by having fine precipitates, then their work shows that a temper of 715°C (the lowest temperature that they employed) gave the finest particles at all normalization temperatures for which they have data.

Table 2.3 Influence of a heat treatment on microstructural parameters of P92 steel (Zielinska-Lipiec and Czyrska-Filemonowicz 2007)

Temp. Normalization °C	Temp. Tempering °C	Dislocation density, $10^{14}m^{-2}$	Mean subgrain size, μm	Mean diameter $M_{23}C_6$, nm	Mean diameter MX, nm
970	715	8.72 ± 1.21			
970	775		0.38 ± 0.1		
1070	715	8.98 ± 1.15	0.37 ± 0.1	72 ± 16	14 ± 3
1070	775	7.46 ± 0.94	0.42 ± 0.09	81.6 ± 28	16 ± 3
1070	835	2.26 ± 0.58	0.50 ± 0.1	83.7 ± 22	16 ± 4
1145	715		0.37 ± 0.08	53 ± 9	12 ± 3
1145	775		0.42 ± 0.09	68 ± 19	15 ± 4
1145	835	2.12 ± 0.52	0.58 ± 0.12	81 ± 27	12 ± 3

2.4.3 Characteristics of Precipitates

The main types of strengthening precipitates in P92 in the as-received heat-treated conditions are $M_{23}C_6$ and MX, with Laves phase precipitating at long term high temperature exposure.

2.4.3.1 $M_{23}C_6$

$M_{23}C_6$ is the principal precipitate found in P92 in the quenched and tempered condition. A variety of work has been done to characterise the $M_{23}C_6$ produced by normalization and tempering in P92 (Ennis et al. 2000; Zielinska-Lipiec and Czyrska-Filemonowicz 2007). It has been found that when normalized at 1070°C, any $M_{23}C_6$ is completely dissolved, but then forms rapidly during tempering. The carbides precipitate mainly on prior austenite grain boundaries and subgrain boundaries, as was illustrated in Figure 2.15. The size of the $M_{23}C_6$ precipitates in P92 is typically less than 100 nm (the actual size depending upon the details of the heat treatment, as shown in Table 2.3). Compared to previous generations of 9-12%Cr steels such as P91, in which $M_{23}C_6$ is typically between 200 and 380 nm (Anderson et al. 2003), the $M_{23}C_6$ in P92 is much finer. $M_{23}C_6$ contributes to material strengthening by retarding subgrain growth so the finer size of the precipitates in P92 increases its strength relative to previous materials. However, after long term exposure at high temperatures, the precipitates coarsen and this reduces the creep strength.

The $M_{23}C_6$ has a face-centred-cubic (fcc) structure (Sourmail 2001) and is typically $Cr_{23}C_6$ with iron, molybdenum and nickel being able to partially substitute for the chromium. The addition of boron to P92 helps to reduce the coarsening of $M_{23}C_6$. During air cooling after normalising, boron segregates to prior austenite grain boundaries through a non-equilibrium mechanism. Non-equilibrium segregation means that boron atoms have been dragged to the boundary by vacancies, not that there exists a binding energy between boron atoms and the boundary. During cooling from the normalisation temperature, boron starts to diffuse back into the grain on a time scale of one or two minutes. Together with the carbon, the boron then gets incorporated in the growing $M_{23}C_6$ (which could now be referred to as $M_{23}(C,B)_6$, and depending on the distance between the prior austenite grain boundary and the precipitate, more or less boron is available during the growth process that takes place during tempering. For precipitates close to or at the prior austenite grain boundaries, a higher B:C ratio than in the steel as a whole is possible. As boron diffusion and precipitate growth occur over the same time scale, the boron does not affect the number density of $M_{23}C_6$ as nucleation occurs before any boron has diffused to the precipitate. The boron has been reported to decrease the interfacial energy between $M_{23}(C,B)_6$ and the matrix, thus reducing the driving force for coarsening (Abe et al. 2004; Czyrska-Filemonowicz et al. 2003; Golpayegani et al. 2003).

2.4.3.2 MX

The MX precipitate is also found in P92 steel. It has a face-centred-cubic (fcc) structure and precipitates mainly in the subgrain interior (see Figure 2.15). It can take a number of compositions where M = Nb and/or V, X = C and/or N, and the precipitates can be referred to as carbides, nitrides and carbonitrides (Sourmail 2001). There are three main types of MX precipitates that can be found in P92. The first type is NbX which are spherical and relatively coarse. They remain after austenitsation and are randomly dispersed in the steel, due to the niobium content being higher than the limits of the mutual solubility of niobium and carbon and / or nitrogen in austenite at the austenisation treatment temperatures used for P92 (Ennis et al. 1998; Maruyama et al. 2001; Zielinska-Lipiec and Czyrska-Filemonowicz 2007). Secondary MX phases form during tempering and these take the form of NbX and VX. These MX particles are fine and are distributed uniformly in the subgrains. The majority of the secondary

MX are vanadium-rich and are between 12-16 nm in size (Zielinska-Lipiec and Czyrska-Filemonowicz 2007) (see Table 2.3), and compared to the primary MX in P92 which is typically 100 nm (Anderson et al. 2003), these secondary MX precipitates are much finer. The third type of MX precipitate is called a V-wing complex. These occur when the large Nb(C, N) that was undissolved during austenitization act as nucleation sites for the VN that are produced during tempering. The VN tend to form at the edges of the larger Nb(C, N) giving the appearance of a wing hence the term V-wing complex (Hu et al. 2010).

The fine MX particles produced during tempering improve the creep strength of P92 by pinning dislocations (Abe et al. 2007; Klueh et al. 2005), while the coarse NbX that remain at austenitization are able to limit the growth of austenite grains and ensure that the recrystallisation of martensitic laths during tempering does not result in a loss of creep strength (Anderson et al. 2003).

2.4.3.3 Laves Phase

Precipitation of intermetallic Laves phase occurs during creep exposure or isothermal aging at temperatures around 600°C. It typically has a chemical composition $(Fe, Cr)_2(Mo, W)$. The addition of molybdenum and tungsten to P92 steel increases the creep strength of the matrix through solid solution strengthening and, as such, the effect of the Laves phase precipitation on long-term creep strength has been debated as it promotes the depletion of molybdenum and tungsten from solid solution (Hosoi et al. 1986a; Hosoi et al. 1986b; Kunimitsu et al. 1991; Miyahara et al. 1995). Whilst Laves phase has been generally considered detrimental for the creep strength of 9–12% Cr steels because of the reduction in solid solution strengthening, it has been argued that they can contribute to the increase of the creep strength by precipitation hardening under certain circumstances (Hald 1996). More recently, it has been generally argued that fine Laves phase may contribute to the creep strength (Dimmler et al. 2003; Hald 1996; Hald and Korcakova 2003; Korcakova et al. 2001). There are two mechanisms for the nucleation and growth of Laves phase, one of which is that Laves phase precipitates alone on martensite lath boundaries and that such precipitates are coherent with one grain but grow into the adjacent grain which has no rational orientation relationship with them. The other one is that Laves phases are formed in the regions adjacent to $M_{23}C_6$ particles, and then they grow at the expense of the chromium-rich

$M_{23}C_6$ carbides in close vicinity. It has been established that the former of these is the dominant formation mechanism for Laves phase as Laves phases are observed to preferentially locate on the prior austenite grain boundaries and the martensite lath boundaries (Cui et al. 2010).

2.4.4 Mechanisms of transformation

The atomic arrangement in a crystal can be altered (Figure 2.16) either by breaking all the bonds and rearranging the atoms into an alternative pattern (reconstructive transformation), or by homogeneously deforming the original pattern into a new crystal structure (displacive transformation). In the displacive mechanism, the change in crystal structure also alters the macroscopic shape of the sample when the latter is not constrained. The shape deformation during constrained transformation is accommodated by a combination of elastic and plastic strains in the surrounding matrix. The product phase grows in the form of thin plates to minimise the strains. The atoms are displaced into their new positions in a coordinated motion. Displacive transformations can therefore occur at temperatures where diffusion is sluggish. Some solutes may be forced into the product phase, a phenomenon known as solute trapping. Both the trapping of atoms and the strains make displacive transformations less favourable from a thermodynamic point of view. It is the diffusion of atoms that leads to the new crystal structure during a reconstructive transformation. The flow of matter is sufficient to avoid any shear components of the shape deformation, leaving only the effects of volume change. This diffusion is necessary even when transformation occurs in pure iron (Bhadeshia 1999). In alloys, the diffusion process may also lead to the redistribution of solutes between the phases in a manner consistent with a reduction in the overall free energy. Figure 2.17 is a summary of the main transformations that occur in steels.

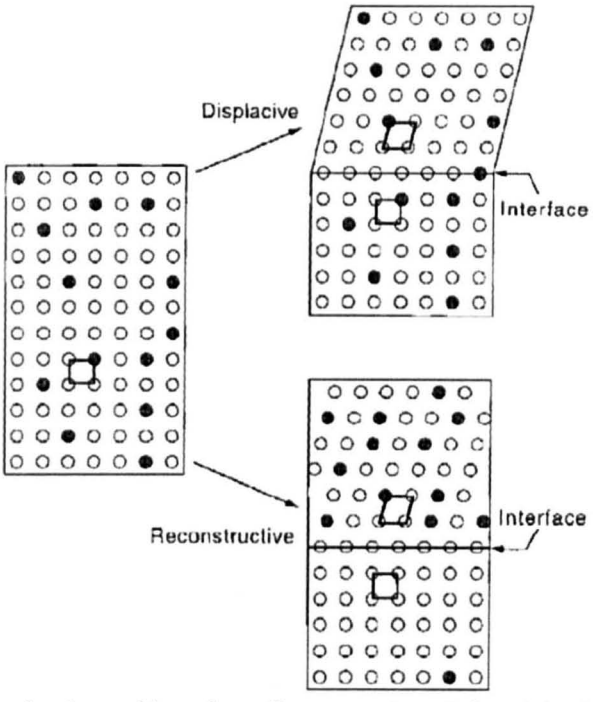

Figure 2.16 Main mechanisms of transformation: parent crystal contains two kinds of atoms; figures on right represent partially transformed samples with parent and product unit cells outlined in bold; transformations are unconstrained in this illustration (Bhadeshia 1999)

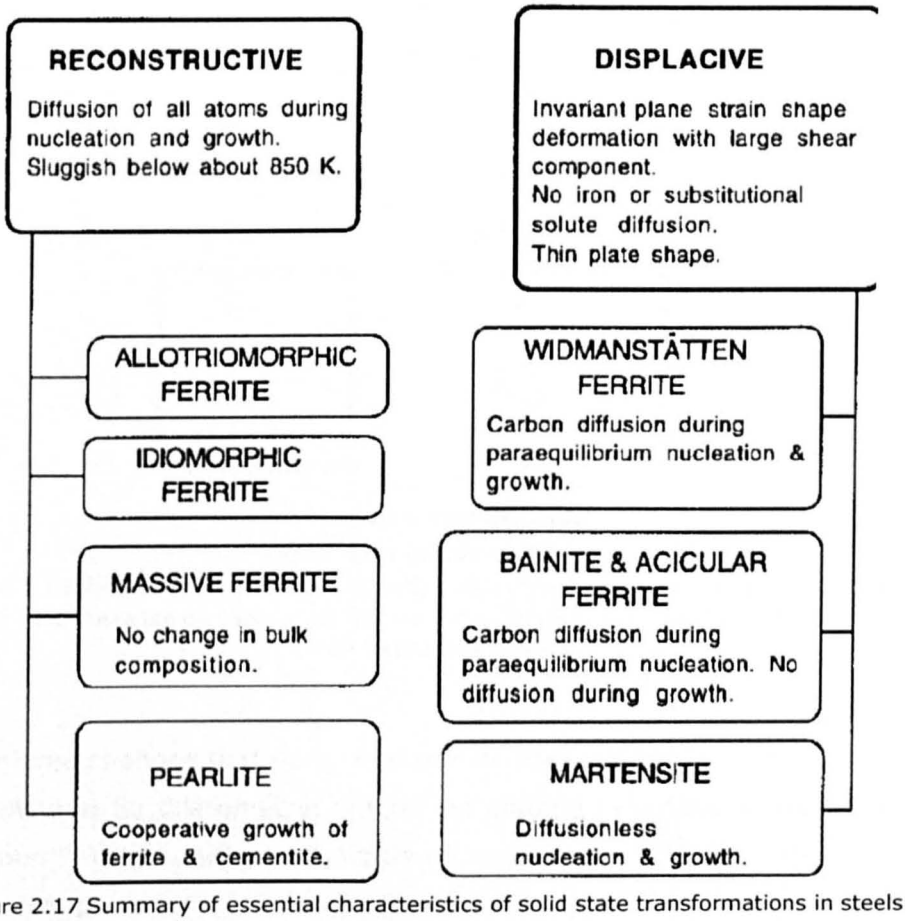

Figure 2.17 Summary of essential characteristics of solid state transformations in steels (Bhadeshia 1999)

The only strain that cannot then be cancelled by diffusion is the volume change due to the difference in densities of the parent and product phases – the strain due to reconstructive transformations in steels is therefore an isotropic volume change. In contrast, displacive transformations typically involve an invariant plane strain shape deformation with a large shear parallel to the invariant plane and a dilatation normal to the plane (the invariant plane is often referred to as the habit plane). They do not involve the diffusion of iron atoms or substitutional solutes. Widmanstätten ferrite, acicular ferrite, bainite and martensite are all products of displacive transformations (Figure 2.17) (Bhadeshia and Honeycombe 2006). Here the movement of iron and substitutional solutes occurs in a coordinated manner, leading to a well defined and reproducible crystallographic relationship between the parent and product phases. It is emphasised that while displacive transformations in steels are associated with a volume change, this change is not isotropic but occurs as a dilatation normal to the habit plane which remains macroscopically undistorted. Also, the volume strain is typically 0.03, which is much smaller than the shear strain which is typically 0.26 (Bhadeshia 2004). The different features of reconstructive and displacive transformations are illustrated in Figure 2.18.

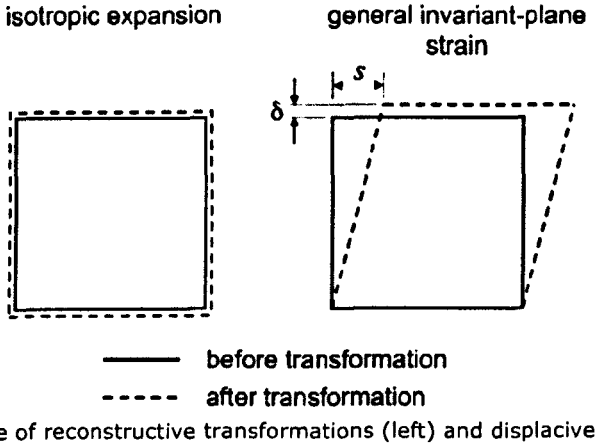

Figure 2.18 Nature of reconstructive transformations (left) and displacive transformations (right) from austenite on cooling: for bainite and martensite s = 0.22–0.26 and δ = 0.02–0.03 (Bhadeshia 2004)

The volume changes that occur in steels as they are heated and cooled can be measured by dilatometry, where the change in length of an unloaded specimen is measured as a function of temperature. Dilatometry is one of the most powerful techniques for the study of solid – solid phase transformations in steels, because it permits the real time monitoring of the evolution of transformations in terms of dimensional changes occurring

in the sample by application of a thermal cycle. The applicability of dilatometry in phase transformation research is due to the change of the specific volume of a sample during a phase transformation. This technique is widely used to study the transformation behavior of steels during continuous heating, cooling, and isothermal holding. By recording the transformations taking place over a range of conditions, it is possible to present the results in a graphical form, which shows the formation temperatures of microstructural constituents that may be obtained for a given cooling or heating condition. Figure 2.19 shows such an experiment (Leblond et al. 1986) – the upper straight line represents the expansion of the body centred cubic phase (ferrite, bainite, martensite) and the lower line that of austenite (γ). Data at locations between the upper and lower lines correspond to the co-existence of the parent and product phases. The transformations occurred at different temperatures upon heating and cooling. The transformation temperature is a function of the cooling rate, steel composition and austenite grain size. The measured coefficient of thermal expansion is larger for austenite ($\sim 23 \times 10^{-6}\ K^{-1}$) than for ferrite ($\sim 15 \times 10^{-6}\ K^{-1}$) (Francis et al. 2007). As a consequence, the volume change due to transformation is greater during cooling than during heating. The volume expansion due to the transformation of austenite can partly compensate for thermal contraction strains arising as a welded joint cools. Each grain of austenite can in general transform into 24 crystallographic variants of bainite or martensite (Bhadeshia and Honeycombe 2006). When all of these form, the effect on a macroscopic scale is that the shear strains average to zero. The volume strain cannot be cancelled in this way since it is always positive with respect to the sample frame, but because of the large number of variants that form, the dilatation observed macroscopically appears isotropic, even though that associated with an individual plate is not (Figure 2.18) (Francis et al. 2007).

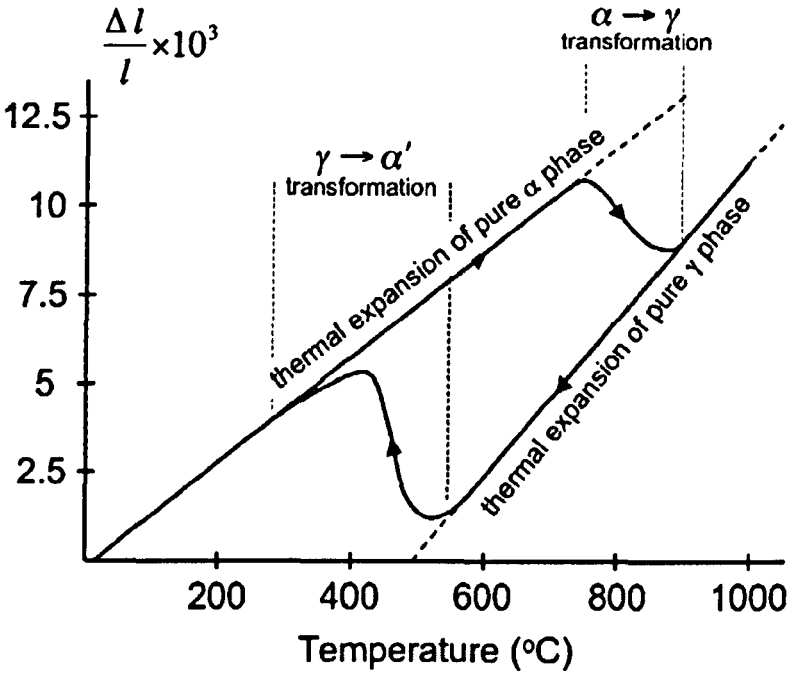

Figure 2.19 Dilatometric diagram of A508 class 3 reactor pressure vessel steel heated at 30 K s-1 and cooled at 2 K s-1 (Leblond et al. 1986)

2.4.5 The α – γ Transformation in 9-12%Cr Steels

Pure iron exists in two crystal forms at atmospheric pressure; one is a body-centred cubic (bcc, α-iron) form that remains stable from low temperatures up to 910°C (the Ae_3 temperature); beyond this temperature, it transforms to a face-centred cubic (fcc, γ-iron) form. The α to γ transformation during heating is accompanied by a volume change of approximately 3% (resulting in a corresponding linear expansion / contraction of 1%), which is associated with a significant contraction on the heating dilatometric curve (Figure 2.19). A study of the constitution and structure of steels must start with the iron-carbon equilibrium diagram, shown in Figure 2.20. Many of the basic features of this system influence the behaviour of even the most complex alloy steels. There are several temperatures or critical points in the iron-carbon equilibrium diagram that are important, both from the basic and from the practical point of view. Firstly, there is the Ae_1 temperature at which the eutectoid reaction occurs, which is 723°C in the binary Fe-C diagram. Secondly, there is the Ae_3 temperature when the final α-iron transforms to γ-iron in heating. For pure iron, this occurs at 910°C, but the temperature of the transformation start is progressively lowered by the addition of carbon. At temperatures between Ae_1 and Ae_3 the microstructure consists of a mix of

α-iron and γ-iron. The Ae_1 and Ae_3 are easily detected experimentally by dilatometry during heating or cooling cycles, but some hysteresis is observed. Consequently, three values for each point can be obtained: (i) Ac values are those measured on heating through the transformation; (ii) Ar values are those measured on cooling through the transformation; (iii) Ae values are theoretical values representing the transformation under equilibrium conditions. It should be emphasized that the Ac and the Ar values are sensitive to the rates of heating and cooling, as well as to the presence of alloying elements.

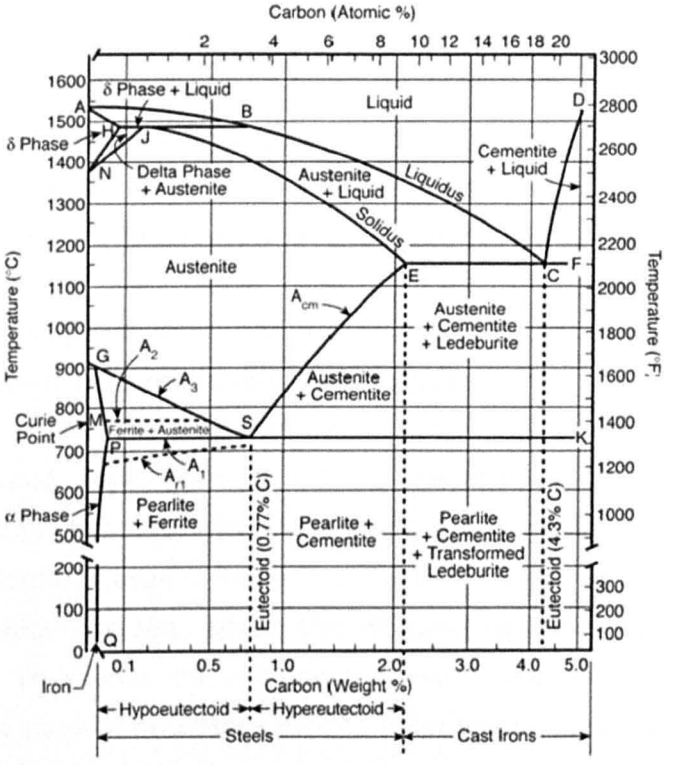

Figure 2.20 The Iron-Carbon phase diagram (Bhadeshia and Honeycombe 2006)

The great difference in carbon solubility between γ- and α-iron (Bhadeshia and Honeycombe 2006) normally requires the rejection of carbon from the α-phase on cooling from the γ- phase. The transformation of γ to α occurs via a eutectoid reaction that plays a dominant role in heat treatment. The eutectoid temperature is 723°C and the eutectoid composition is about 0.8 wt%C. On slow cooling of alloys containing less than 0.80 wt%C, proeutectoid ferrite is formed from austenite in the range 910–723°C with enrichment of the residual austenite in carbon. At 723°C, the remaining austenite, now containing 0.8 wt% carbon, transforms to pearlite, a lamellar mixture of ferrite and iron carbide (cementite). In austenite with

0.80–2.06 wt%C, on slow cooling in the temperature interval from 1147°C to 723°C, cementite first forms progressively depleting the austenite in carbon. At 723°C, the austenite, containing 0.8 wt%C, transforms to pearlite (Bhadeshia and Honeycombe 2006). Ferrite, cementite, and pearlite are thus the principal constituents of the microstructure of plain carbon steels as they are subjected to relatively slow cooling rates to avoid the formation of metastable phases such as martensite and/or bainite.

Rapid quenching of austenite to room temperature often results in the formation of martensite, a very hard structure in which the carbon, formerly in solid solution in the austenite, remains in solution in the new phase. Unlike ferrite or pearlite, martensite forms by a sudden shear process in the austenite lattice that is not accompanied by atomic diffusion, as described in the previous section. The martensite reaction in steels occurs during cooling in a temperature range that can be precisely defined for particular steels. This transformation begins at a martensite start temperature, Ms, which can vary over a wide temperature range from as high as 500°C to well below room temperature, depending on the concentration of γ-stabilizing alloying elements in the steel. Once Ms is reached, further transformation takes place during cooling until the reaction ceases at the Mf temperature. At this temperature, all the austenite should have transformed to martensite, but frequently in practice, a small portion of the austenite does not transform; this is called retained austenite. Large volume fractions of austenite are retained in some highly alloyed steels, where the Mf temperature is well below room temperature. To favour the martensitic reaction over other competing reactions, it is usually necessary for the steel to be rapidly cooled so that the rate of cooling is sufficient to suppress the higher temperature diffusion-controlled ferrite and pearlite formation reactions, as well as other intermediate reactions such as the formation of bainite. The fact that the ferrite and pearlite reactions are essentially high temperature transformations occurring between 720°C and 550°C and that the formation of martensite is a low temperature reaction, reveals that there is a wide range of intermediate temperatures in which neither of these phases forms. This is the region in which fine aggregates of ferrite plates (or laths) and cementite particles are formed. The generic term for this intermediate structure is bainite. Bainite also occurs during continuous cooling at rates too fast for ferrite and pearlite to form, yet not rapid enough to produce martensite (García de Andrés et al. 2002).

2.4.5.1 Continuous Heating Transformations

It is the allotropic nature of iron, and its solubility for carbon that makes possible the large range of transformations, microstructures, and properties of plain carbon steels. The temperatures at which the transformation of austenite commences and finishes at different rates of cooling are of importance for planning and designing many industrial processes. Moreover, there are other transformations, which cause the steel to revert to the austenitic condition, in which the knowledge of the transformation temperatures during heating is vital.

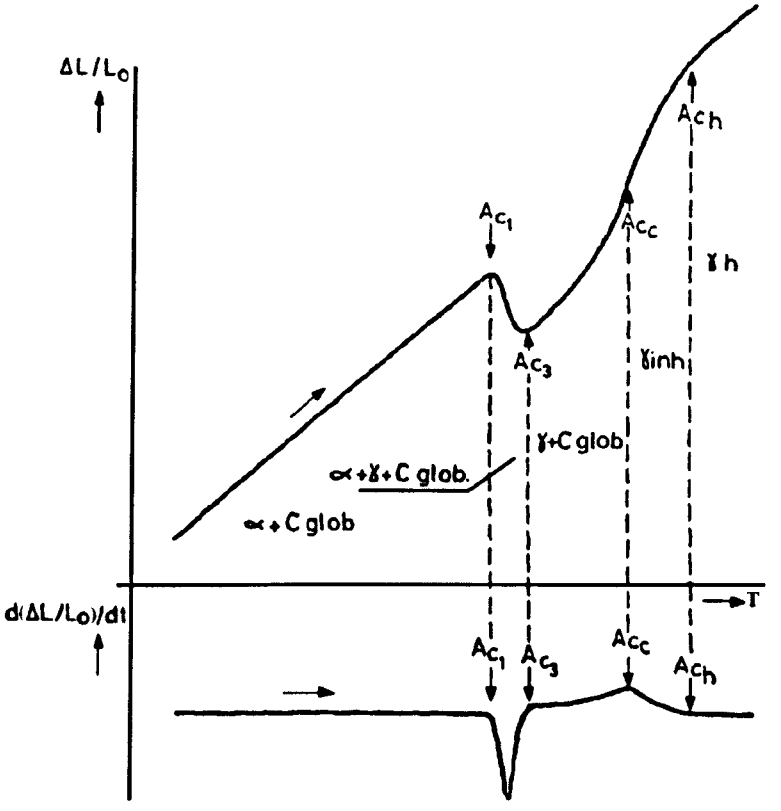

Figure 2.21 Diagram of the heating dilatometric response of α→γ transformation and the carbide dissolution process of martensitic 9-12%Cr steels (García de Andrés et al. 2002)

A schematic diagram showing curves of relative change of length as a function of temperature ($\Delta L/L_0 = f(T)$) and its corresponding derivative ($d(\Delta L/L_0)/dt = f(T)$) are shown in Figure 2.21. This diagram illustrates the contraction that takes place during the ferrite-to-austenite transformation by continuous heating of a martensitic stainless steel with an initial microstructure of ferrite plus globular carbides ($M_{23}C_6$). These dilatometric curves, aside from the α to γ transformation between Ac_1 and Ac_3 temperatures, develop a nonlinear length variation associated with the carbide dissolution process. During heating at temperatures above Ac_3,

there is a continuous increase of slope in the curve $\Delta L/L_0$ = f (T) that corresponds to the progressive dissolution of the carbides in austenite. The point of inflexion of this section displayed as a maximum in the $d(\Delta L/L_0)/dt$ = f (T) curve corresponds to the Ac_c temperature or the temperature at which the carbide dissolution process ends. Since the presence of carbides in the as-quenched microstructure of these steels has a decisive effect on its creep-rupture properties, the study of the carbide dissolution process is important for the optimization of these materials. In this sense, dilatometric analysis plays an important role in the detection of the temperature at which the carbide dissolution process reaches completion during continuous heating (García de Andrés et al. 2002). Once the carbides have been dissolved, significant concentration gradients (in carbon and other alloying elements) exist throughout the austenite phase. As the temperature to which the steel has been heated increases, these concentration gradients are reduced by diffusion, reaching the homogeneity at the Ac_h temperature. As shown in Figure 2.21, dilatometric analysis enables the determination of this temperature at the point where the $\Delta L/L_0$ = f (T) curve starts to display again a linear tendency characteristic in the thermal expansion of a homogeneous phase.

The key transformation points during continuous heating can be summarised as:

- Ac_1 = The temperature at which the ferrite-to-austenite transformation begins during continuous heating.
- Ac_3 = The temperature at which the ferrite-to-austenite transformation ends during continuous heating.
- Ac_c = The temperature at which the carbide dissolution process ends during continuous heating.
- Ac_h = The temperature at which the microstructure becomes a single homogeneous phase during continuous heating.

2.4.5.2 Continuous Cooling Transformations

Examples of experimental critical temperatures for the non-isothermal decomposition of austenite into ferrite and pearlite are displayed on the dilatometric curve of a carbon manganese steel (Fe–0.2C–1.1Mn–0.34Si) in Figure 2.22. The Ar_3 and Ar_1 critical temperatures correspond, respectively, to the start and finish temperatures of the nonisothermal

decomposition of austenite into ferrite plus pearlite. The specific austenite-to-pearlite transformation may not show a clear indication of the transformation start in many instances. This is not due to lack of resolution, but to a masking of the individual reactions by the continued growth of the other phase.

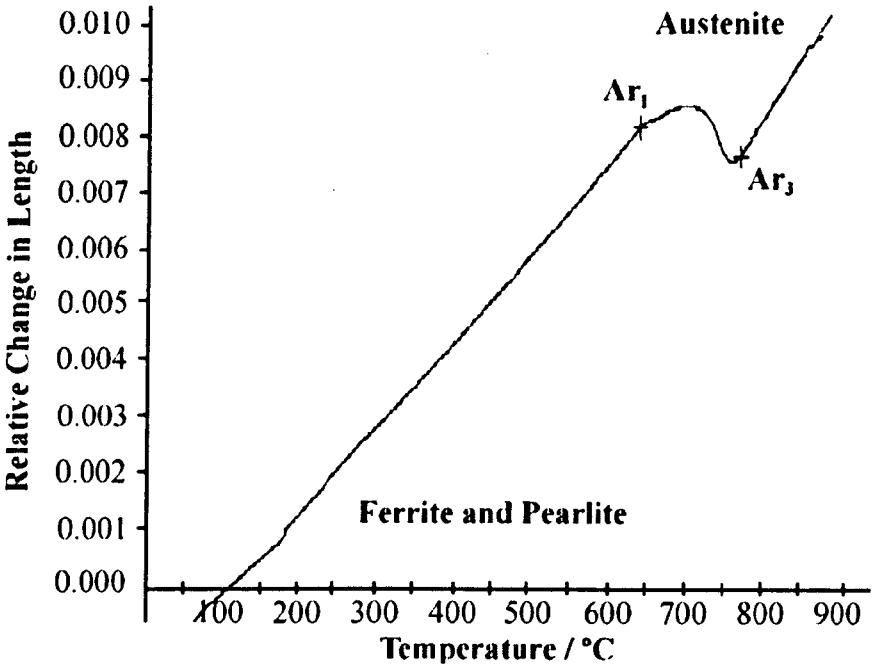

Figure 2.22 Cooling dilatometric curve of a carbon manganese steel (Fe- 0.20C-1.1Mn-0.34Si) obtained at a cooling of 1 K s^{-1} (García de Andrés et al. 2002)

Figure 2.23a shows the dilatometric curve of a low carbon manganese steel (Fe -0.07C-1.56Mn-0.41Si) after rapid cooling (234 K s^{-1}) (García de Andrés et al. 2002). Dilatometric analysis indicates that two different transformations take place during cooling in the steel. Metallographic examination shows that the final microstructure obtained after cooling at a rate of 234 K s^{-1} is composed of bainite and martensite (Figure 2.23b). Since bainite is formed at higher temperatures than martensite, the first volume expansion displayed on the curve corresponds to the transformation of austenite into bainite, whereas the volume expansion shown at the lower temperature corresponds to the transformation of austenite into martensite. The bainite (Bs) and martensite (Ms) transformation start temperatures are, respectively, the temperatures at which the thermal contraction shown by the dilatometric curve deviates from linearity due to the volume expansion associated to the bainite transformation first and the martensite transformation later, and when

transformation is completed (Mf), it returns to linearity (Bhadeshia and Honeycombe 2006).

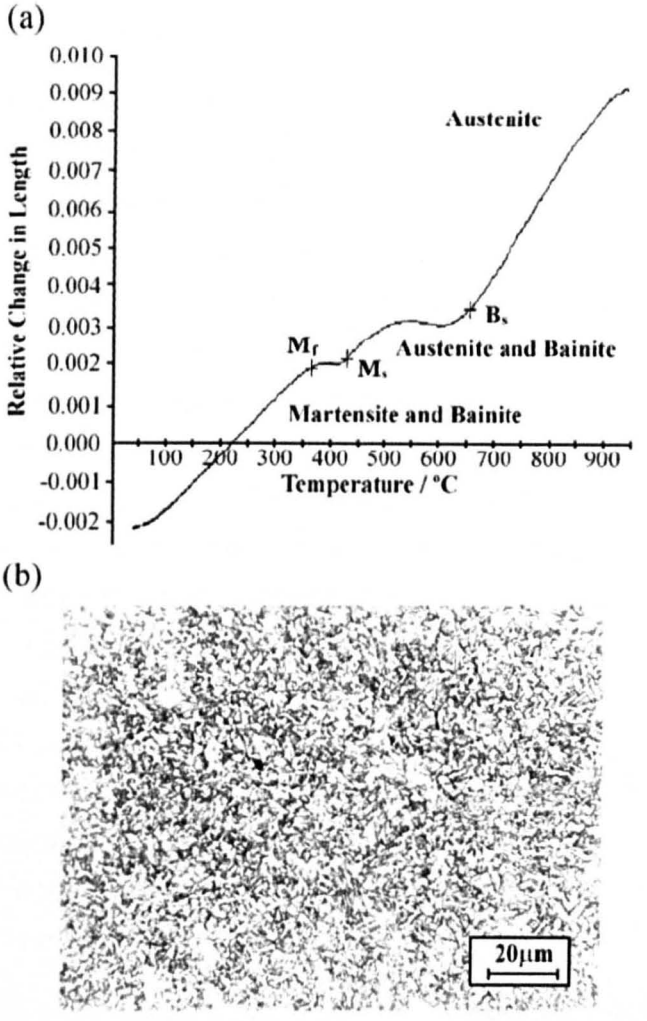

Figure 2.23 (a) Cooling dilatometric curve and (b) microstructure of a low carbon manganese steel (Fe – 0.07C–1.56Mn–0.41Si) after cooling at a rate of 234 K s^{-1} (García de Andrés et al. 2002)

The key transformation points during continuous cooling can be summarised as:

- Ar_3 = The temperature at which the decomposition of austenite to ferrite begins during continuous cooling.
- Ar_1 = The temperature at which the decomposition of austenite to ferrite ends during continuous cooling.
- B_s = The temperature at which Bainite begins to form during continuous cooling.
- M_s = The temperature at which Martensite starts to form during continuous cooling.

- M_f = The temperature at which Martensite finishes forming during continuous cooling.

2.5 Welds in Power Plant Steels

2.5.1 Microstructure of Welds

Fusion welding involves the localised injection of intense heat and its dissipation by conduction into the parent material. The weld microstructure at each location is therefore closely related to the thermal history (Lancaster 1993). The different zones and their characteristics for a single pass weld have been well described (Mannan and Laha 1996; Savage et al. 1976) and are shown in Figure 2.24 (Francis et al. 2007). Regardless of the primary solidification structure, the fusion zone in low alloy steels transforms to austenite at a temperature not far from the solidification point, and then undergoes a solid state transformation to a structure that will depend on both the hardenability of the alloy and the cooling rate. Adjacent to the fusion zone is a heat affected zone (HAZ), a region that is not heated sufficiently to cause melting, but nevertheless is microstructurally altered by the welding thermal cycle. As indicated in Figure 2.24, the HAZ can be subdivided according to the extent to which grain growth and austenitization occur as follows; (i) a coarse grained zone (CGHAZ); (ii) a fine grained zone (FGHAZ); (iii) an intercritical zone (ICHAZ) and (iv) over tempered base metal.

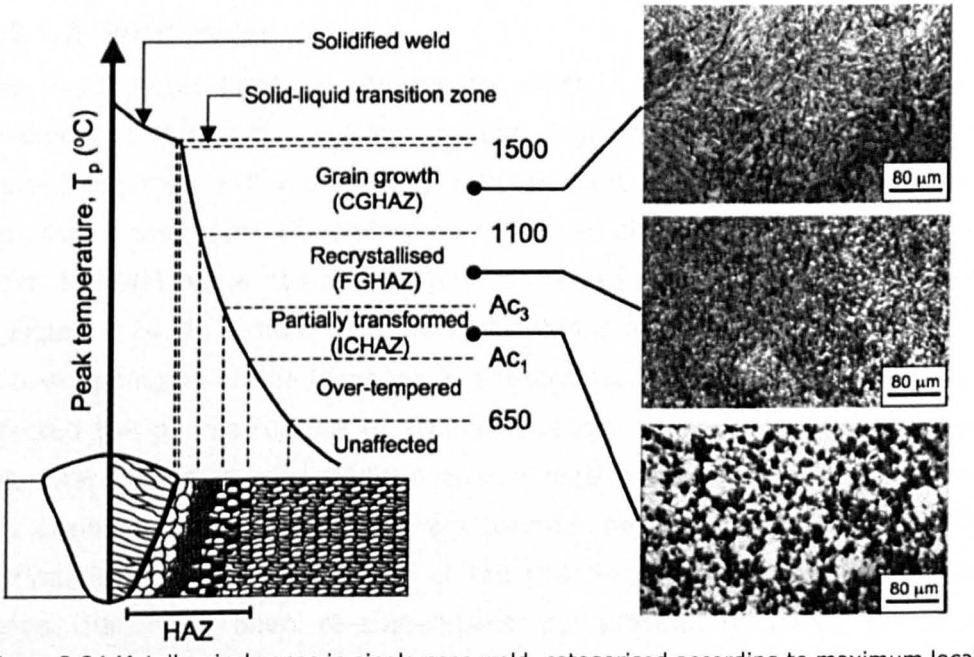

Figure 2.24 Metallurgical zones in single pass weld, categorised according to maximum local temperature: micrographs correspond to weld in 2.25Cr–1Mo steel (Francis et al. 2007)

2.5.1.1 HAZ and regions of HAZ

The heat affected zone (HAZ) is the area of base metal that has not been melted by the weld pass but which has had its microstructure and properties significantly altered by the thermal cycle associated with welding. The thermal history of the HAZ differs depending on its distance from the heat source, giving rise to different microstructures that can be divided into two regions; a high temperature region and a low temperature region. The high temperature region is mainly the coarse grained HAZ (CGHAZ) and the low temperature region consists of the fine grained HAZ (FGHAZ) and the intercritical heat affected zone (ICHAZ), and these regions are shown in Figure 2.24. During welding, the CGHAZ is adjacent to the molten weld pool, so it experiences a very high peak temperature. This peak temperature is much higher than the α to γ transformation temperature Ac_3, so the microstructure is re-austenised and results in the coarse grained microstructure. The number of grain boundary precipitates in the CGHAZ is low as at the high peak temperature, most existing precipitates are dissolved, and rapid cooling does not allow them to re-form. The FGHAZ experiences a peak temperature around the Ac_3 which allows recrystallisation to take place, resulting in a finer grain structure. The existing precipitates in the FGHAZ do not dissolve but rather coarsen. The ICHAZ experiences a peak temperature just above the eutectoid Ac_1 temperature, so the microstructure is a mixture of fine recrystallised grains and the unchanged grain structure of the parent metal.

2.5.1.2 Weld Metal

The weld metal (WM) is the region which undergoes melting and re-solidification during the welding process. Filler metal and parent metal are melted together and well mixed, with element distribution in this region generally thought to be uniform (Francis et al. 2007). In a single-pass weld, the WM has a coarse columnar structure as indicated schematically in Figure 2.24. In a multi-pass weld, the WM is made up of a large number of overlapping weld beads where a repeated heating and cooling cycle has affected the microstructure of adjacent beads, which includes the coarse columnar region, a recrystallised coarse grain region and a recrystallised fine grain region which together are termed the recrystallised region. The recrystallised region is made up of the coarse columnar zone of previous beads that have been re-austenitised by subsequent bead deposition leading to the refined equiaxed structure.

2.5.1.3 Weld interface

The weld interface is defined as the interface between the liquid metal and the heat affected zone. It can be further defined at a finer scale as shown in Figure 2.25 (Savage and Aronson 1966; Savage et al. 1976). What is normally called the fusion line is actually a region with two additional zones between the weld metal and heat affected zone, namely the unmixed zone and the partially melted zone.

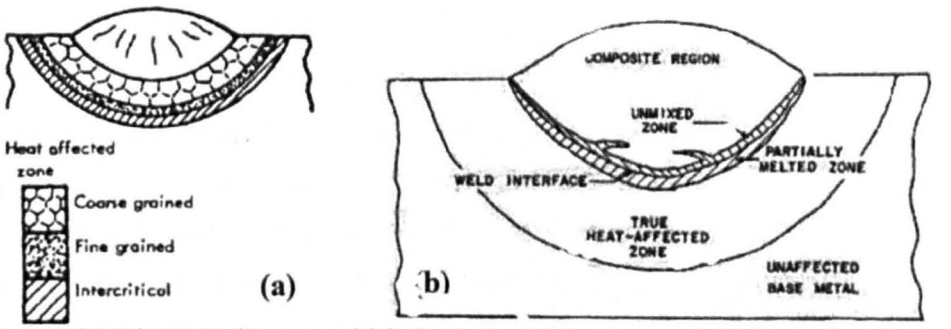

Figure 2.25 Schematic diagrams of (a) classical weld structure and (b) Savage's definition of weld interface region (Savage et al. 1976)(Savage et al. 1976)

Unmixed zone

The unmixed zone is the narrow band consisting of melted and solidified base metal and any composition gradient between the composite region and the parent metal contained in the unmixed zone, where the base metal in this region has been completely melted. Savage (Savage et al. 1976) argues that while molten, the material in this region only experienced lamellar flow, indicating that the liquid at the fusion boundary does not experience mechanical mixing but only diffusional mixing.

The significance of the unmixed zone is given more consideration for the fusion boundary of heterogeneous welds and less for autogenous and homogeneous welds due to their uniform composition. However, it is possible that in an autogenous or homogeneous weld, the resulting composition of the WM may be different from the base metal due to other factors, such as absorption, outgassing, oxidation, and vaporization of certain elements. As such, an unmixed zone may be significant even in these cases (Savage et al. 1976).

Partially melted zone

The partially melted zone is the narrow band region between the unmixed zone and the HAZ, where the base metal has undergone only partial melting during welding. Localised melting is caused by the variation of the

effective melting temperature from place to place, which is due to the point-to-point variations in solute content in the base metal. In the partially melted zone, the grains near the fusion boundary are smaller than those in the nearby region of the HAZ where no localised melting has taken place (Savage et al. 1976).

2.5.1.4 Multi-Pass Welds

Fusion welding of thick walled components necessarily involves many weld passes to fill up the joint. Weld beads covered by other passes then experience multiple heat pulses and a further subdivision of metallurgical zones. Some of the possible combinations of thermal cycles are illustrated in Figure 2.26 (Francis et al. 2007). With regard to the sequence shaded dark grey in Figure 2.26, the initial intercritical heating cycle may not have a significant effect on the final microstructure, since the subsequent cycle introduces a much higher peak temperature at that location. However, other sequences can have significant and detrimental effects. For example, the intercritically reheated CGHAZ is the zone of the CGHAZ which is only partly reaustenitised during a subsequent thermal cycle and is shaded black in Figure 2.26. In some steels, a concentration of austenite stabilisers, such as carbon, can be developed in the regions that are reaustenitised and, upon cooling, these locations transform into hard microstructures associated with poor toughness, the so-called local brittle zones. Given that the austenite in the CGHAZ would have originally been coarse, the decline in toughness in the intercritically reheated CGHAZ can be identified via hardness tests (see section 2.3.4.3).

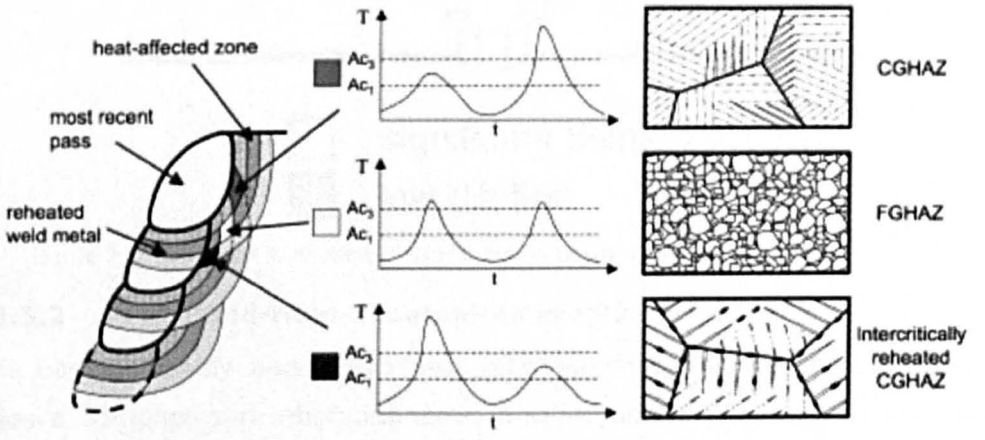

Figure 2.26 Examples of thermal cycles in multipass weld (Francis et al. 2007)

Filler metals for ferritic steels are generally selected to achieve an appropriate balance between strength and toughness, or to mitigate against toughness related problems such as cold cracking (Reddy et al. 2003). Other factors may also be relevant, such as with 9–12%Cr creep resistant steels, where it is important to avoid the formation of δ-ferrite at high temperatures and yet still achieve a complete transformation to martensite at ambient temperature (Onoro 2006). The design requirements for weld filler metals generally necessitate a chemical composition that differs from the parent material. Thus, in a multipass weld, the composition of one weld bead can vary from the next as a consequence of changes in dilution levels. A schematic representation of how dilution might vary in a typical power plant steel weld is given in Figure 2.27. The extent to which dilution might influence microstructure will depend on the mismatch between the compositions of the filler metal and parent material. However, in microalloyed steels, even a relatively small change in composition due to dilution has been shown to significantly affect weld toughness (Hunt et al. 1994).

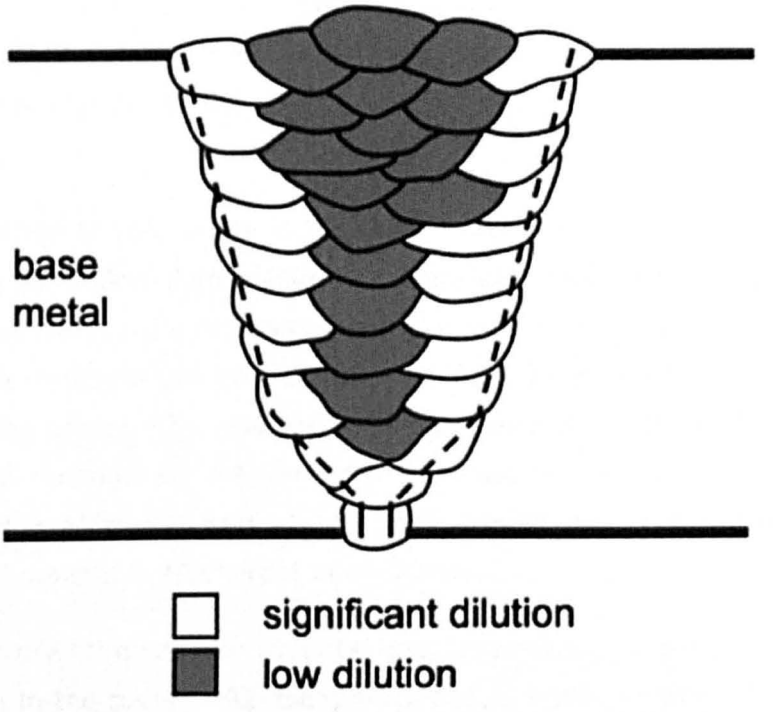

Figure 2.27 Variation in dilution of filler metal in power plant weld (Francis et al. 2007)

2.5.2 Post-Weld-Heat-Treatments in P92

As has previously been described, after welding, the resultant weldment has a complex and inhomogeneous microstructure. This region will have very different mechanical properties to the parent material and if put into

service in the as-received condition, it would be likely that it would suffer heavy damage. Post-weld-heat-treatment (PWHT) of such weld joints is necessary to stabilize the microstructure, improve its toughness and also to relieve residual stresses after welding.

In the 9-12%Cr power plant steels, structures of this type undergo a post weld heat treatment (PWHT) which tempers the martensite formed in the HAZ and produces a complex distribution of precipitates which enhances their resistance to creep deformation (Cool and Bhadeshia 1997). This PWHT is typically carried out at 765°C for the parent P92 with a tolerance range of +/- 15°C (Marshall et al. 2002a), with the minimum PWHT being set in international standards at 730°C to avoid weakening of the materials mechanical properties such as toughness and creep-rupture strength. When selecting the PWHT temperature, it is important to consider the A_1 temperature of the material; if the PWHT temperature exceeds the A_1 temperature (even if transiently), then austenite may re-form in the steel, resulting in the formation in the final product of either untempered, brittle martensite (if the cooling rate from the temperature where austenite is formed is high enough) or soft ferritic regions (associated with slow cooling rates, or extended thermal soaks at temperatures below the austenite stability region), both of which are undesirable. Both of these phases are creep-weak (for different reasons) and will thus promote early component failure.

The presence of soft ferrite is the more likely consequence of inadvertent austenite formation during PWHT. A transient period of reaustenitization (due to temperature overshoot) will result in ferrite being reformed during the sub-A_1 temperature period, be this either the primary soak period, or the cooling period. The relevant welding standards (BSI 1987b) define a maximum cooling rate following PWHT; however the actual cooling rate immediately after the end of the soak period is commonly below the permitted maximum (Richardot et al. 2000a).

There is very little concern that the heat treatment will result in austenite formation in the parent P92 itself, since the A_1 temperatures in the parent are typically between 830-900°C (depending upon the specific composition within the specification) (Richardot et al. 2000a), some 70°C above the target heat treatment temperature. However, there are concerns that the alloy composition may result in other undesirable phase transformation behaviour; Cool and Bhadeshia (Cool and Bhadeshia 1997) conducted work

to examine austenite formation during PWHT of 9Cr-1Mo steels, finding that excessive use of austenite stabilising elements such as nickel renders alloys susceptible to austenite formation. However, it was also found that the excessive use of ferrite stabilisers prevented the steel from been able to fully austenitise at high temperatures, leading to the retention of soft δ-ferrite (Cool and Bhadeshia 1997) in the steel structures.

In addition, it is recognised that microsegregation may exist in weld metals due to their rapid solidification which may result in different parts of the microstructure exhibiting different transformation temperatures (Santella et al. 2003). Nickel and manganese are the primary austenite stabilisers ensuring full austenite formation (without δ-ferrite) during the austenitization and thus a 100% martensite structure on cooling (Knezevic et al. 2008). According to Marshall (Marshall et al. 2002a), the tendency for undesirable reaustenitization of P92 weld metals during heat treatment may be understood by considering the sum of the nickel and manganese levels in the steel; specifically, he proposed that the minimum Ac_1 for P92 weld metal at 1.5wt%(Ni + Mn) is 790°C and thus suggested that 775°C is therefore a safe upper limit for the PWHT temperature assuming that a margin of error of ± 15°C in the PWHT temperature is required.

2.5.3 Creep failure of 9-12%Cr steel welds

Weldment structures generally have lower creep strength than normal bulk steels as a result of their complex and heterogeneous structures formed during the welding thermal cycle. A typical welded structure consists of parent metal, heat affected zone and weld metal (see Figure 2.24) which all have different creep properties. Failure modes of welds during creep have been well studied (Francis et al. 2004; Issler et al. 2004) and have been categorised according to the position of the creep fractures within the weldment;

I. Type I occurs within, and is confined to, the weld metal.
II. Type II occurs within the weld metal but may grow beyond the weld and into the bulk.
III. Type III occurs in the coarse grained HAZ (CGHAZ, Figure 2.24) close to the fusion boundary. It is actually reheating cracking that arises early in life as a result of creep strain absorbed during the decay of residual welding stress exhausting local ductility.

a. Type IIIa also occurs in the CGHAZ but occurs later in life in more ductile regions after long-term loading (Brett 2004).

IV. Type IV occurs in the low temperature HAZ, typically the intercritical HAZ (ICHAZ, Figure 2.24).

Creep cracking has also been found at the inter-bead (weld bead on weld bead) fusion boundaries which differs from type IIIa cracking which occurs adjacent to the fusion boundary of weld bead to parent metal (Allen et al. 2007a).

2.5.3.1 Type IV cracking in ICHAZ

Type IV cracking is considered the most important life-limiting failure mechanism in weldments under creep conditions. It occurs in a circumferential mode just outside the fully transformed HAZ region adjacent to the parent metal. During welding, the ICHAZ is heated to a maximum temperature between the Ac_1 and Ac_3 resulting in partial transformation from α to γ (Gaffard et al. 2005). Upon cooling, any γ transforms to soft ferrite, leading to a microstructure of tempered martensite and soft ferrite. As the peak temperature of the heating cycle is relatively low with a short duration, precipitates do not generally fully dissolve in the austenite whereas in the CGHAZ, they typically do. The resulting microstructure of the ICHAZ has a very fine structure consisting of subgrains with low dislocation density. Hardness measurements reveal that the ICHAZ has a hardness lower than both the rest of the weldment and the parent material (Albert et al. 2003; Wu et al. 2004). After creep exposure, creep cavities form in the ICHAZ resulting in a failure mechanism involving creep of locally constrained regions (Wu et al. 2004). Coarsening of $M_{23}C_6$ and an absence of secondary reprecipitation of fine MX particles during tempering and creep exposure have been identified as major mechanisms accelerating the poor creep response of the ICHAZ (Spigarelli and Quadrini 2002).

2.6 Summary

P92 steel is a high-alloy steel that has been specifically designed for operating at high temperatures (600°C - 650°C) and has found wide use in the power generation industry, particularly since 2005. For the successful installation and use of this advanced steel all aspects of its behaviour, in terms of both metallurgy and in-service behaviour, must be understood.

In normal industrial practice, following welding with P92 fillers, post-weld heat treatment is carried out, and there is a desire to perform this heat treatment close to the A_1 temperature of the materials involved to develop what are considered to be the best mechanical properties in the weld and heat affected zone. As such, it is important to accurately know the A_1 temperature of the materials being heat treated. There are gaps in the knowledge as to how each of the elements in the material, rather than just the obvious elements such as manganese and nickel, affect the transformation temperature, A_1, and the rate at which austenite could form during PWHT. This gap in the knowledge of how composition affects the A_1 temperature is applicable to both welds and parent material.

Specifications for weld metals (and parent metal) define a range of compositions, but do not offer any guidance on how variations within that specification may affect the final material properties. As precipitation strengthening is important to the creep resistance of P92, it is important to understand how the levels of precipitates may vary even within the specification.

The creep failure associated with welds has been regarded as a critical issue in the studies of power plant steels, and there is also little guidance on how the composition variations often necessary for successful welding affect the creep rupture performance.

In light of this, the current thesis will seek to examine and seek a greater understanding of the behaviour of welds in P92 steel so that their in-service behaviour may be better understood, focussing on the response of the material to post-weld heat treatments (PWHT), the optimum weld consumable composition and the microstuctural development during creep-rupture. From this, alloy specifications of weld consumables may be improved, quality checks on P92 used by industry could better ensure the fitness for service of a material if an accurate composition is known and

enable manufacturers to further tailor compositions to produce the strongest possible material. Furthermore, the design and selection of P92 material that will not undesirably transform during heat treatments could be enhanced.

The outcomes of this thesis should enable a better understanding of P92 parent metal and welds and provide results that are immediately applicable and useful to the power generation industry through the collaboration that SuperGen provides.

3 Experimental Work

3.1 Material and specimen preparation

3.1.1 Weld pad preparation

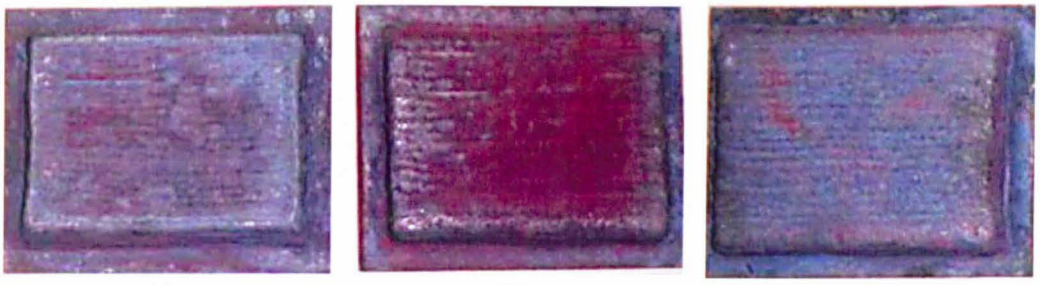

(a) (b) (c)

Figure 3.1 The three weld 200mm x 150mm weld pads (a) A, (b) B and (c)

As depicted in Figure 3.1, three ~200 x 150 x 30 mm multipass weld pads were made by Doosan Babcock Energy Ltd. (UK), by depositing 4 mm diameter flux-coated consumable stick electrodes (A, B or C) onto carbon-manganese steel base plates using the manual metal arc (MMA) procedure with DC+ polarity and a current of 160-170 A. The resulting heat input was around 1.5 kJ mm^{-1}. Approximately 20 runs were made per layer, and each pad consisted of at least 10 layers. The deposition was performed in the 200 mm direction only, at speeds between 140-180 mm/min with a weld bead overlap of around 50%.

A preheat/interpass temperature between 200-300°C was maintained throughout the welding process, measured using temperature indicating crayons. Chipping/wire brushing between passes (to remove slag) was performed where necessary. After welding, a post-weld heat treatment of 760°C was applied for 2 hrs.

3.1.2 Specimen preparation

Standard 50mm gauge-length, ridged, uniaxial (Figure 3.2) specimens were removed from the weld pads using electric discharge machining (EDM) so that the test loading axis was transverse to the welding direction.

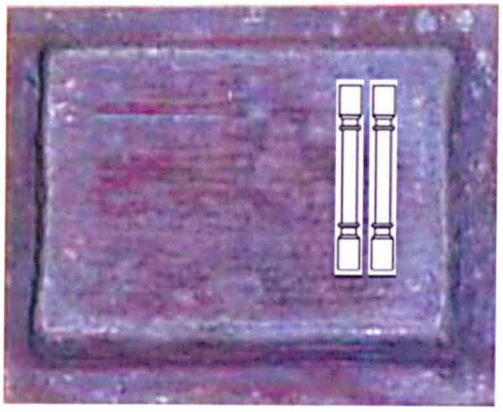

(a)

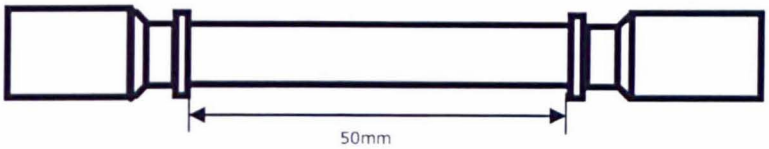

(b)

Figure 3.2 (a) Orientation of creep specimen removal (schematic only, not to scale) and (b) schematic of the creep specimen

To help ensure consistent test results and to avoid the effect of dilution from the steel base plates, material close to the weld start and stop edges of the pads and material comprising the innermost and outermost beads was not used. The majority of the specimens were creep tested in-house and were 130 mm long with a 10 mm diameter gauge section, based on BS 3500: Part 3. However, a small number of creep tests were performed by Corus UK Ltd. and these specimens were 88 mm long with a 6.25 mm diameter gauge section, based on ASTM E21 & E8. The results do not seem to have been affected by the different gauge cross section sizes, although it is known that smaller sections can introduce more scatter in the results of inhomogenous materials such as weld pads (Evans, R W and B Wilshire. 1985). Where tests have not been carried out in-house, this is indicated in the results.

Creep tests were performed in air at three different temperatures and nominal stress conditions, given in Table 3.1. Constant uniaxial tensile loading was applied in the direction of the specimen axis, transverse to that of welding. Strain measurement over the gauge length was regularly logged using output from extensometers attached via the specimen ridges.

Table 3.1 Weld metal creep test parameters

Weld Metal	Temp. (°C)	Stress (MPa)
A	625	150
A *	625	150
B	625	150
C	625	150
A	625	170
B	625	170
C	625	170
C (rpt)	625	170
A *	670	90
B	670	90
C	670	90

* - tested by Corus UK Ltd., (rpt) - repeat

The uniaxial creep tests were performed on the Denison Creep Testing Machine. The basic frame of the machine is a 2 m × 2 m 'L' shape, the vertical section having 4 × ϕ50 mm columns and the horizontal section consisting of a lever system whereby the load is applied.

The graduated load lever is linked to the bottom lever which in turn connects, through knife edges, with the lower loading bar (within the afore-mentioned columns).

Since the lengthening of the specimens allows the load lever to gradually fall to its lower limit, a 'strain take-up' system comes into operation from time to time to prevent this happening. It is triggered by the end of the load lever pressing on a micro-switch which in turn causes a DC motor-drive screw system to draw the upper loading bar upwards. Since the upper loading bar is connected through the specimen to the lower loading bar, the load lever is gradually raised to its highest working position and as this occurs another micro-switch causes the strain take-up motor to be switched off. The whole of this operation is very slow, taking about half an hour and hence the load on the specimen remains steady.

All of the specimens have been machined with knife-edge flanges. Conventional extensometer 'legs' are fitted to these flanges and at the lower ends of the legs linear voltage displacement transducers produce, via a conditioning unit, a DC voltage which is proportional to strain. The voltage is then fed to a computer-based data-logging system.

A 3-zone muff type furnace is lowered to surround the specimen which previously has had three thermocouples spot welded to it. Each of the three furnace zones, together with its thermocouples, forms an independent control loop via a Eurotherm electronic controller and its associated thyristor.

Both specimen 'caps' have their threads cleaned of debris by a M16 tap in order to avoid torsional effects when the specimen is fitted to the loading bars. The lower cap is screwed onto the lower bar and the specimen is then itself screwed into the M16 hole. Then the upper cap is screwed into the top of the specimen so that it almost goes beyond the lower end of the thread. This procedure allows the top cap to have full thread engagement on both the specimen and the upper loading bar, when fitting is completed.

Three thermocouples are then prepared by using three 1 m lengths of thermocouple wire. One end of each piece is connected to the controller input while the other is tightly twisted and spot welded to the appropriate position on the specimen (two outside the gauge length and one in the middle). Then the extensometer legs are fitted carefully, ensuring that the specimen knife edge flanges fully engage with the 'V' shaped grooves at the top of the assembly.

After a final inspection to ensure that everything is correctly positioned, the furnace is lowered so that its centre coincides with that of the specimen.

In order to avoid any damage to the specimen it is essential that whilst heating up to the test temperature, the strain take up system (S.T.S.) is operating. For this reason a minimum over balance is set on the load lever and the S.T.S. is switched on with the gear train pin engaged (a modification to the loading machine stops the furnace from being switched on whilst the S.T.S. is switched off).

In less than 2 hours the specimen should have reached the required temperature. When this is achieved the loading lever is temporarily supported by a prop close to its free end. The gear train pin is then removed and the manual S.T.S. wheel is turned anti-clockwise about 5 to 10 turns. This will ensure that the knife edges are at minimum disengagement so that when the load is manually wound on there is no jolting as contact is re-established. With the loading lever firmly propped,

the moveable weight is wound along the lever to the position where the scale indicates the appropriate force.

The strain transducers are finally positioned so that their plungers are almost fully retracted and intercept values are keyed into the logger to ensure that zero strain is displayed. Then the manual S.T.S. wheel is steadily wound clockwise to bring the loading lever knife edges into contact and soon after this has occurred the load lever should rise from the prop and the latter is carefully removed.

After starting the test, it is only necessary to periodically check that progressive strain increase is displayed and that the load lever has not 'bottomed'. When the load lever reaches the bottom after a period of testing time, this will show that the specimen has failed.

3.2 Characterisation Methods

3.2.1 Sample Preparation

All creep tested specimens were sectioned using electric discharge machining (EDM) through the specimens parallel to stress axis so that the plane of the cross-section lay normal to the welding direction, while sections of the weld pad were machined using EDM and a cut-off wheel. Sectioned samples were mounted using cold mounting epoxy resin for large specimens for examination via optical microscopy (OM) and hardness tests. Hot mounting with conductive phenolic mounting resin black was employed for smaller specimens for all forms of microscopy. Cross-sections of the samples were ground and polished with SiC papers and loose diamond abrasives down to a 1μm finish for OM and scanning electron microscopy (SEM), with a further polish to a 0.06μm finish with colloidal silica for electron back-scatter diffraction (EBSD) analysis. Samples for OM and SEM were etched with alcoholic ferric chloride (5g $FeCl_3$, 2ml HCl, 95ml ethanol) for 20 seconds to reveal the microstructure. Samples that underwent heat treatment had any surfaces that were to undergo examination ground back by ~1 mm before polishing in order to avoid regions that may have undergone decarburisation.

3.2.2 Optical Microscopy

Optical microscopy (OM) was used for the examination of samples up to magnifications of x40. OM is primarily used to obtain macro-scale information on the weld structure and montages of the microstructure were generated using Adobe Photoshop and multiple images. Scale markers are displayed on individual images.

3.2.3 Micro-hardness Measurement

Micro-hardness of specimens was measured using a Leco M-400 tester with a Vickers indenter. The indentation time was 15 seconds and hardness values are obtained by measuring diagonals of hardness indents and using Equation 3.1 to convert to Vickers hardness readings;

$$H_v = \frac{2F\sin\frac{\theta}{2}}{d^2} \approx \frac{1.854F}{d^2}$$

Equation 3.1

where F is the load in kgf, θ = 136°, d is the arithmetic mean of indent diagonals in mm and therefore H_v is the Vickers hardness in kgf/mm^2. The force used and spacing of indents is stated when results are presented. The hardness tester was calibrated using a calibration block of known hardness. For hardness traverses, each reading is taken from a single point. For bulk hardness the values are an average of five points.

3.2.4 Scanning Electron Microscopy (SEM)

The scanning electron microscope (SEM) uses a high-energy electron beam, which scans a sample surface, for imaging. The electrons interact with atoms in the sample to produce signals that provide information about the sample. Secondary electron (SE) signals provide information concerning the topography and surface structure of the sample, while back-scattered electrons (BSE) provide information about element distribution with contrast being related to the mean atomic number of the material. Characteristic X-rays were used to identify and quantify composition using the energy dispersive X-ray (EDX) analysis method. A Philips XL-30 equipped with a field emission gun (FEG), which facilitates imaging at higher magnification that that of a traditional tungsten filament SEM (by producing an electron beam that is smaller in diameter, more coherent and with a much greater current density/brightness), was used. Specimens for examination in the SEM must be conductive and so, as

stated in 3.1.1, samples were hot mounted in conductive phenolic mounting resin.

Samples were imaged using a 20 kV accelerating voltage and a working distance of 10 mm unless otherwise stated. Laves phase precipitates were quantified according to the method presented by Korcakova et al. (Korcakova et al. 2001) which relies on the contrast between these precipitates and the matrix that is evident in BSE images. The method presented by Korcakova et al. uses the image analysis software ImageJ to convert the BSE images into a binary image which, due to the high contrast, results in the Laves phase been clearly defined from the rest of the material. The software can then count the number and mean size of the precipitates. This method could not be used for the MX and $M_{23}C_6$ phases due to their low contrast with the matrix. To count the size and number of these precipitates, ImageJ was again used but the precipitates had to be manually identified first before the image was turned binary. The difference between the MX and $M_{23}C_6$ phases was determined by their location an relative size based on the description of their morphology in section 2.4.2. While transmission electron microscopy (TEM) is a more usually used method for the counting and sizing of precipitates, Korcakova et al. demonstrated that these methods which use SEM images gave comparable results and were much less time consuming, allowing a greater (and therefore, more representative) area of the material to be examined in the same time. For the sizing and counting of precipitates 40 images per sample were evaluated.

3.2.5 Electron Back-Scatter Diffraction (EBSD)

Electron back-scatter diffraction (EBSD) is a microstructural-crystallographic technique, which allows crystallographic information to be obtained in an SEM fitted with a backscatter diffraction camera. When the electron beam impinges on a tilted crystalline sample, the diffracted electrons form a characteristic diffraction pattern on a fluorescent screen which can be analysed to provide information such as grain morphology, crystal orientation and grain boundary misorientations. EBSD examination was carried out at Loughborough University using an EDAX Pegasus combined EBSD and EDX system attached to a LEO 1530-VP FEGSEM.

Special care must be taken when preparing samples for EBSD examination; diffraction electrons escape from only a few tens of

nanometres from the sample surface, and so it is essential to remove all mechanical distortion which is generally produced during grinding and polishing. To this end, following polishing down to a 1 μm finish with diamond abrasives, an additional final polishing stage using colloidal silica was then carried out to remove residual surface damage. The colloidal silica polish is a chemo-mechanical polish that combines the effect of mechanical polishing with etching. This polishing stage was conducted for at least 30 minutes to achieve the desired surface finish. The EBSD examination used a 20 kV accelerating voltage and an aperture size of 30 μm. The sample was tilted at 70° with respect to the horizontal.

As producing high resolution images with EBSD can be time consuming, a series of low quality images were first taken at 5 locations in the samples to ensure that any final image would be representative of the microstructure.

3.2.6 Dilatometry

The Ac_1 temperature of the three weld metals and the P92 steel was measured by dilatometry, carried out using a thermomechanical analyser (TA Instruments Q400) with a sample size of ~ 5 x 5 x 15 mm and a heating rate of 100°C/hour unless otherwise stated in order to simulate the rate used in industrial PWHT; the sample dilatation was measured using a glass probe resting on top of the sample. The Ac_1 temperature was derived from the dilatometric traces, being identified as the point at which the gradient of the line on heating (associated with thermal expansion) began to decrease (associated with the contraction associated with the phase transformation from ferrite to austenite). Dilatometry is discussed in detail in section 2.4.5. The dilatometer was calibrated using an iron-carbon calibration block of known transformation temperature. For the determination of the initial Ac_1 temperature, three samples per material were used, and for the examination of the effect of holding temperature three samples per temperature were used.

3.3 Modelling

Thermodynamic modelling of phases expected in the steels as a function of composition and temperature was carried out using Thermo-Calc 5 for Windows with the TCFE6 Steel and Fe-alloys database (Foundation of Computational Thermodynamics and Thermo-Calc Software AB, Stockholm, Sweden). Thermo-Calc is a software package used to perform thermodynamic and phase diagram calculations for multicomponent systems in materials science and engineering. Calculations are based on thermodynamic databases produced by expert evaluation of experimental data using the CALPHAD method. The CALPHAD method is based on the fact that a phase diagram is a representation of the equilibrium thermodynamic properties of a system, which are the sum of the properties of the individual phases. It is thus possible to calculate a phase diagram by first assessing the thermodynamic properties of all the phases in a system.

TCFE6 is the steel and Fe-alloy database for Thermo-Calc and can be applied in steel and Fe-alloy design and engineering. The TCFE6 database includes data for molar volume calculation of density and lattice parameter (for cubic structures), coefficient of thermal expansion and/or relative length change.

Thermo-Calc can be used for all kinds of calculations of thermodynamic properties, equilibrium and partial/local-equilibrium quantities, chemical driving forces, and for various types of stable/meta-stable phase diagram and property diagrams of multi-component systems. Thermo-Calc deals with systems that are in equilibrium, i.e. in a state stable against internal fluctuations in a number of variables such as temperature and composition. If the work that can be exchanged with the surroundings is limited to pressure-volume work, then the state of equilibrium of a system can be obtained by assigning values to exactly N+2 state variables where N is the number of components of the system. The output of phase diagrams can show the phases present in terms of mole fraction, mass fraction and volume fraction.

The modelling started with defining the system, which, in this work amounts to defining the elements contained in the steel with the TCFE6 database. The phases which are considered in the calculation can be selected from the full list of possible phases. The concentration of each

element is defined under a temperature and pressure to obtain the equilibrium. In all calculations, pressure was kept at atmospheric pressure.

For the production of phase property diagrams, the initial inputs were the chemical composition (with iron left to make up the balance of the system), pressure and an initial temperature. To produce the phase property diagram, a temperature range must also be defined which in this case was 500°C to 2000°C. The number of steps (iterations) in the calculation must also be defined, and for all phase property diagrams this was set at 50. An increased number of steps can increase the accuracy of the results but also increases calculation time. Initial calculations used steps of 10, 50, 100, 200 and 500. The 10 step calculations gave different transition temperatures, while use of all the other numbers of steps gave the same results. Therefore 50 steps was chosen as the calculation gave reliable accuracy in the shortest time. The potential phases included in the calculations must also be defined, and the list of phases included is shown in section 4.1. For the production of graphs, the resulting data were exported to Microsoft Excel.

4 Results

4.1 Weld Consumable Composition and Modelling

Table 4.1 P92 alloy specification ranges (Richardot et al. 2000b), along with compositions of the parent P92 and weld metals (Weld Metal A, Weld Metal B and Weld Metal C) studied in this work.

	Element, wt% (balance iron)															
	C	N	B	Si	Mn	P	S	Cr	Mo	Ni	Al	Co	Cu	Nb	V	W
P92 min	0.07	0.03	0.001	-	0.3	-	-	8.5	0.3	-	-	-	-	0.04	0.15	1.5
P92 max	0.13	0.07	0.006	0.5	0.6	0.02	0.01	9.5	0.6	0.4	0.04	-	-	0.09	0.25	2.0
Parent P92	0.1	0.47	0.0034	0.45	0.45	0.015	0.002	8.62	0.33	0.27	0.019	-	-	0.076	0.21	1.86
WMA	0.11	0.047	-	0.2	0.78	0.011	0.005	8.73	0.45	0.64	-	-	0.04	0.043	0.199	1.66
WMB	0.09	0.048	-	0.42	0.99	0.011	0.006	8.74	0.49	0.42	-	-	0.04	0.08	0.23	1.59
WMC	0.1	0.025	0.007	0.23	0.59	0.013	0.009	9.82	1.41	0.7	-	1.09	0.02	0.05	0.25	-

Table 4.1 shows the measured compositions of the three weld deposit materials, provided by the Supergen industrial sponsors, that were initially examined for use with P92. The P92 alloy specification is also shown, as is the composition of the parent P92 that the weld consumable will be used with later in the work programme. The weld metals were chosen to encompass the range of compositions that can be seen in power plant welds. All are commercially available, with WMA and WMB having been derived from the P92 specification, while WMC is based on creep-resistant alloy B2 and has been included due to its potentially greater creep strength. In order to understand what phases may be expected to make up the microstructures of the weld metal derived from each of the consumables (under equilibrium conditions), thermodynamic modelling was used. The measured composition of each weld metal type was input into the program ThermoCalc along with the phases (and crystal structures) that were to be included in the calculation as follows;

- Face Centred Cubic (FCC)
- Body Centred Cubic (BCC)
- Laves Phase
- $M_{23}C_6$

- M_6C
- MnS
- M_3P
- AlN
- BN
- Liquid, Gas (for calculations that are near melting temperatures)

where FCC is the crystal structure of the MX precipitates and austenite; identification of which phase is being predicted can be achieved by examining the predicted composition and phase fraction. Ferrite is represented by the body centered cubic phase. Only phases that have been observed in the literature for 9Cr steels are included in the calculation.

It is worth noting at this point that the formation of martensite, the desired matrix in P92 steels, cannot be predicted in ThermoCalc as it is the product of a non-equilibrium displasive transformation (see section 2.4.4). Instead ThermoCalc predicts α-ferrite; the transformation to martensite in actual P92 material is facilitated by rapid cooling from temperatures above A_1.

4.1.1 Weld Metal Phase Fraction Diagrams

Figure 4.1 shows the phase property diagrams for the three weld metal types selected over a temperature range from 500-2000°C, thereby encompassing possible service temperatures, post-weld-heat-treatment conditions and the high temperature conditions experienced during welding. The phases predicted to be present are shown in the figure legends with the primary phases being low temperature α-ferrite, γ-austenite, high temperature δ-ferrite and liquid above 1500°C. From these phase diagrams, the Ae_1 temperature and the temperature at which δ-ferrite will begin to form on heating can be derived and these are shown for the three weld metal types in Table 4.2.

Table 4.2 Ae_1 and δ-ferrite start temperatures, as calculated by ThermoCalc

Weld Metal	Ae_1, °C	δ-ferrite Start Temperature, °C
A	758	1274
B	769	1224
C	771	1244

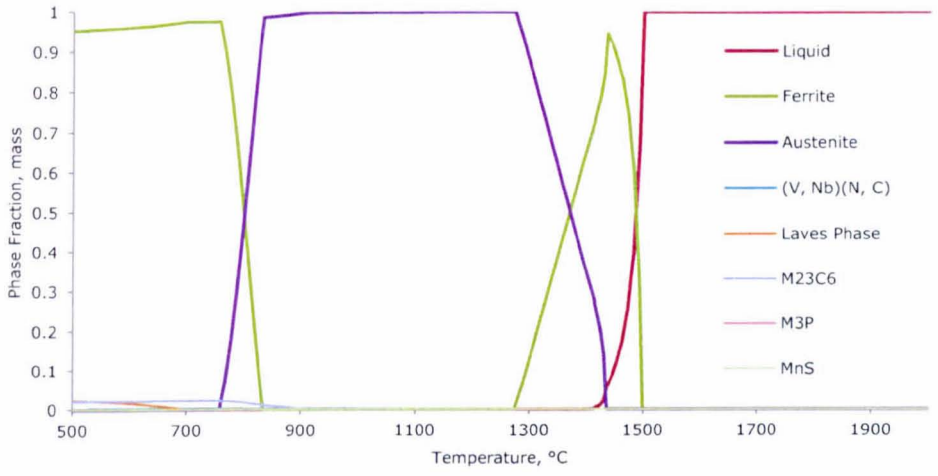

(a)

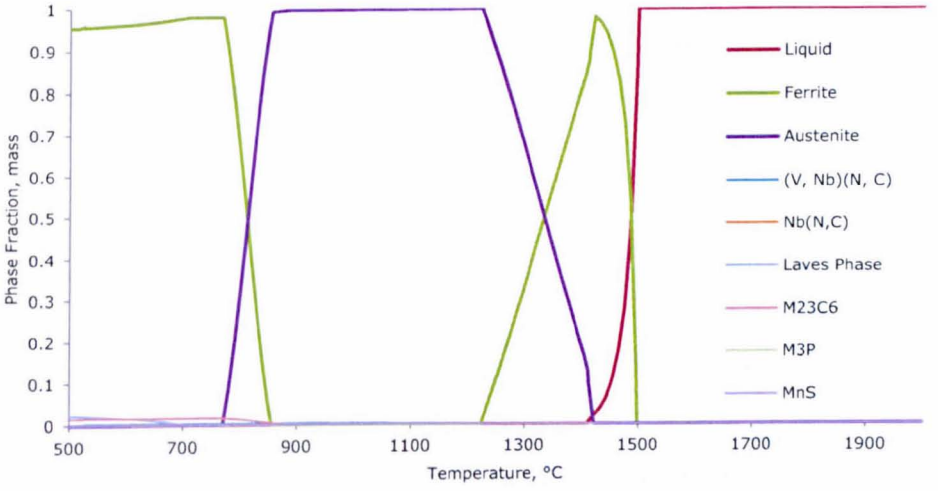

(b)

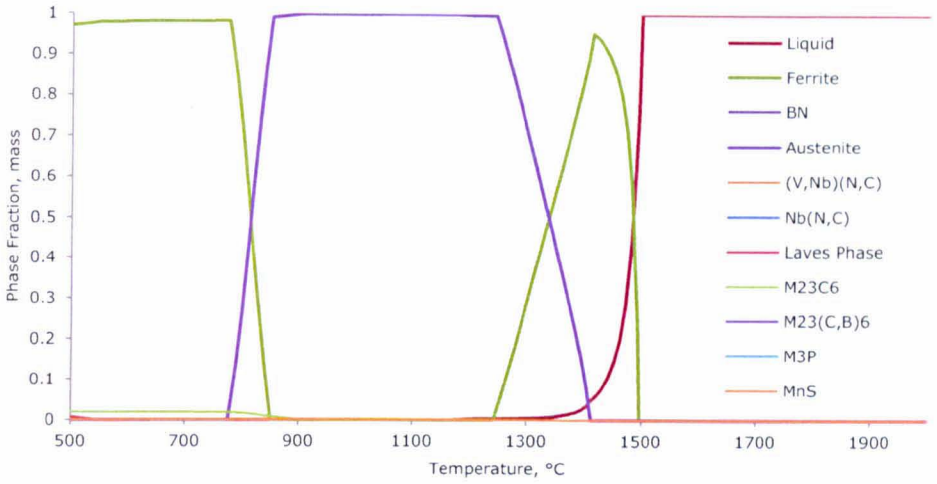

(c)

Figure 4.1 Predicted phase fraction diagrams for the three weld metals (a) WMA (b) WMB (c) WMC at thermodynamic equilibrium

4.1.2 Precipitate Phase Fraction Diagrams

Figure 4.2 shows the phase fraction diagrams for the three weld metals, with just the precipitate phases being considered. All weld consumables are predicted to contain a form of MX, $M_{23}C_6$, Laves Phase and the impurity phases M_3P and MnS. Both WMB and WMC contain two forms of MX, while WMC also has BN and an additional form of $M_{23}C_6$.

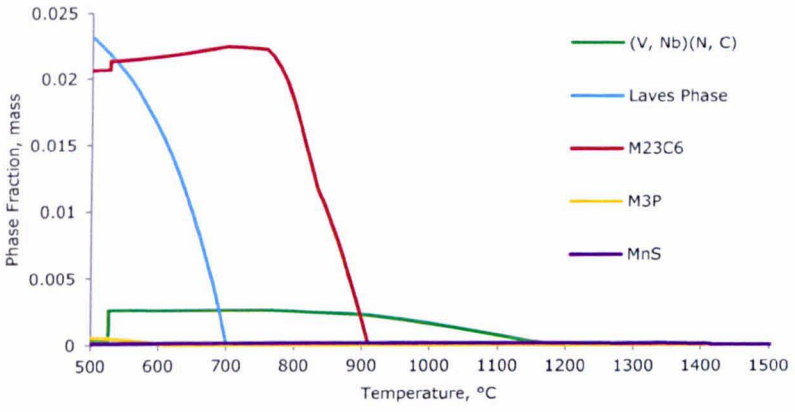

(a)

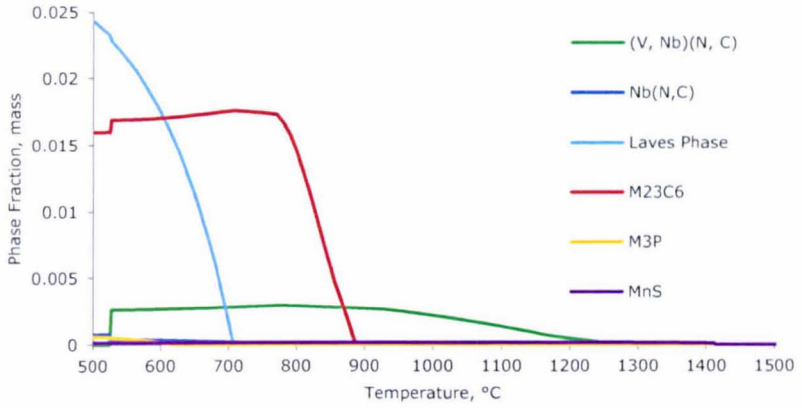

(b)

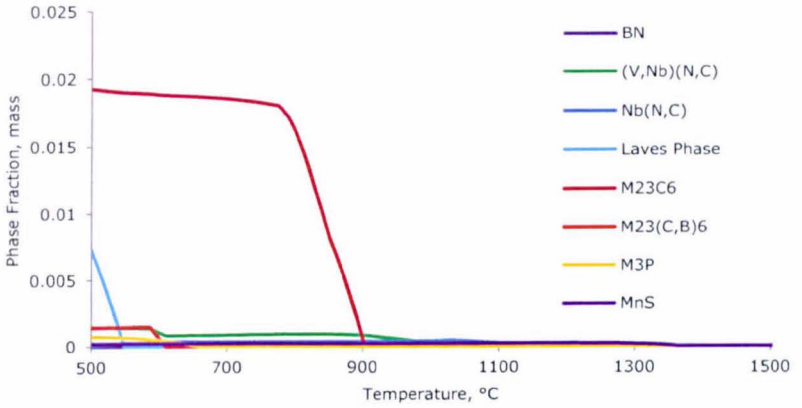

(c)

Figure 4.2 Predicted phase fraction diagrams for the precipitate phases in the three weld metals (a) WMA (b) WMB (c) WMC at thermodynamic equilibrium.

4.1.2.1 Predicted composition of MX

The composition of the MX phases predicted in the three weld metal types are presented in Figure 4.3, showing that the most prevalent form is expected to be (V,Nb)(N,C) in all three weld metal types, while WMB and WMC are predicted to contain a small amount of MX in the form Nb(N,C).

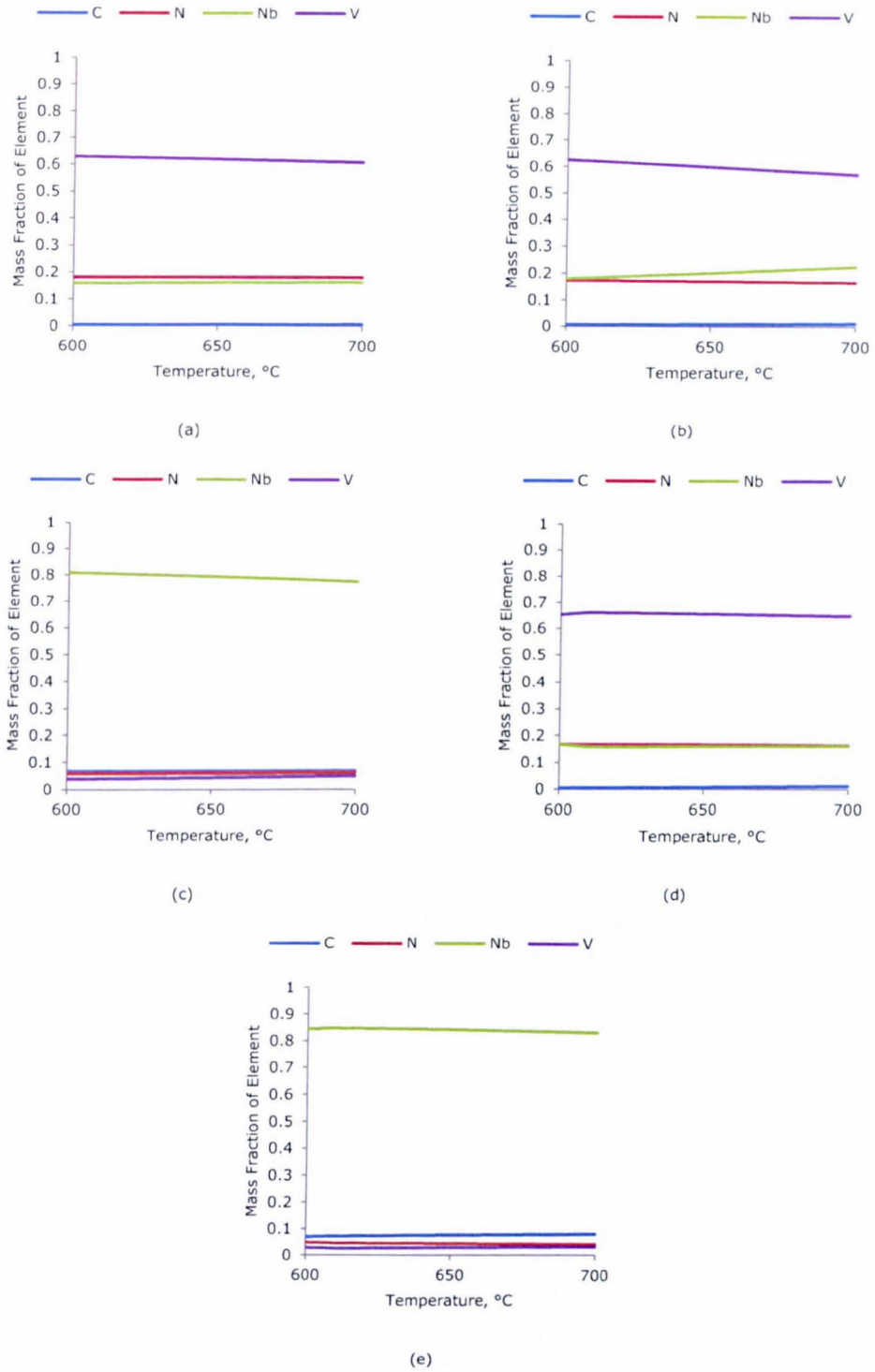

Figure 4.3 Predicted composition of MX phases in the three weld metals (a) (V,Nb)(N,C) in WMA, (b) (V,Nb)(N,C) and (c) Nb(N,C) in WMB, (d) (V,Nb)(N,C) and (e) Nb(N,C) in WMC

4.1.2.2 Predicted composition of $M_{23}C_6$

Figure 4.4 shows the predicted composition of $M_{23}C_6$ in the three weld metal types, showing them to be chromium-rich while the additional form of this phase in WMC is predicted to contain predominantly boron as their non-metallic element, hence it is referred to as $M_{23}(C,B)_6$.

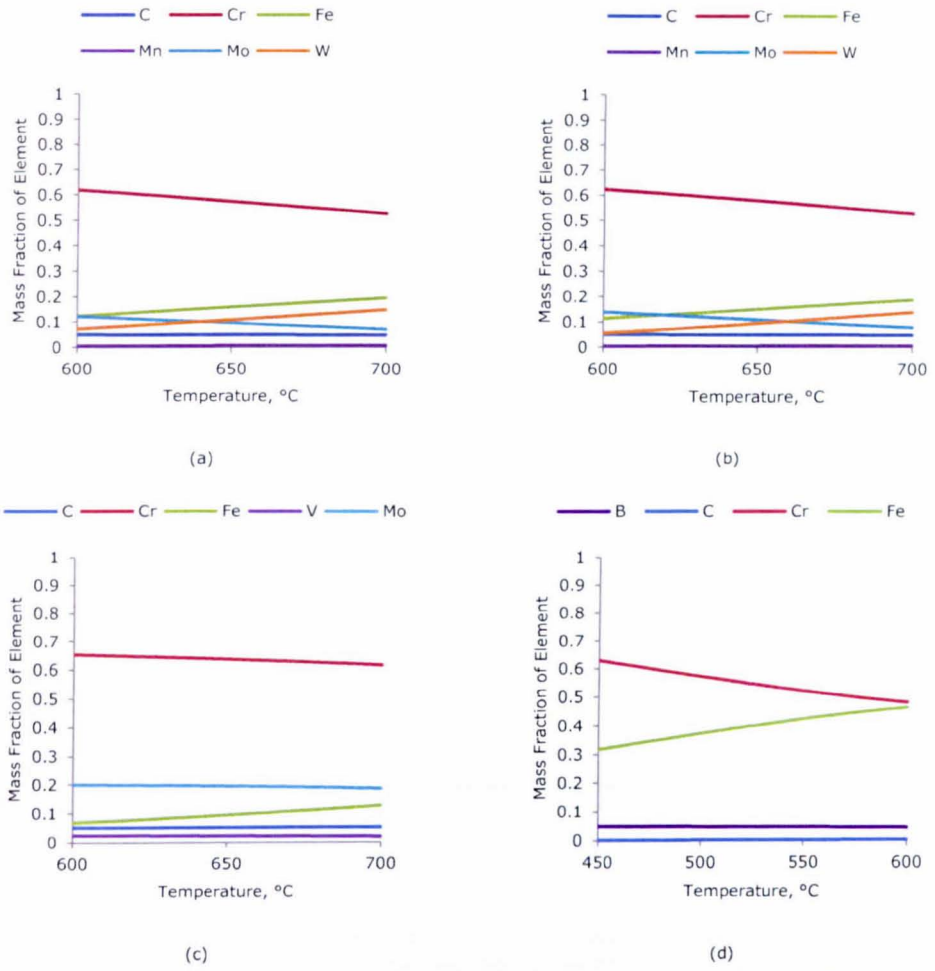

Figure 4.4 Composition of $M_{23}C_6$ phases in the three weld metal types (a) in WMA, (b) in WMB, (c) and (d) in WMC due to the presence of $M_{23}(C,B)_6$

4.1.2.3 Predicted composition of Laves Phase

Figure 4.5 shows the predicted composition of the intermetallic Laves Phase in the three weld metal types indicating that in WMA and WMB, it is tungsten rich while WMC contains a molybdenum rich form.

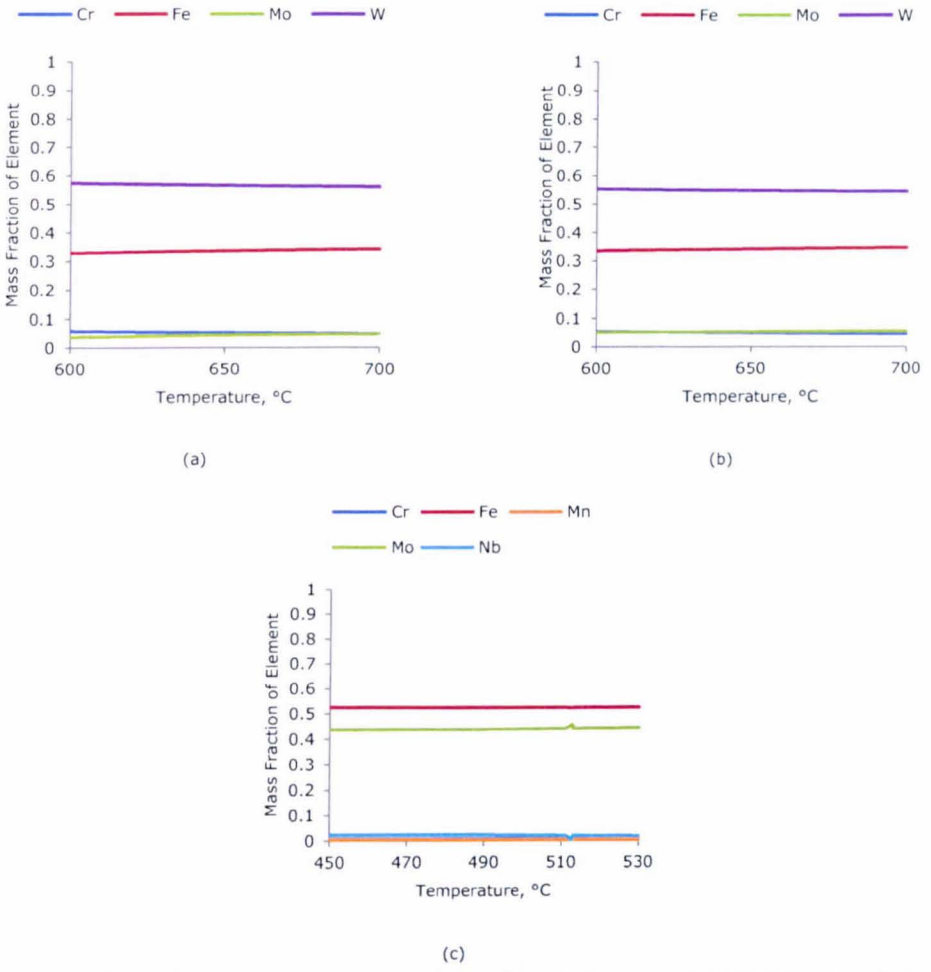

Figure 4.5 Composition of Laves Phase in (a) WMA, (b) WMB and (c) WMC [for WMC the Laves phase is predicted to be unstable above 530°C by ThermoCalc]

4.1.3 The Effect of Element Variation on Precipitation

As the precipitate levels and types have been seen to differ in the two P92-similar weld consumables WMA and WMB, the sensitivity of the equilibrium precipitate fraction and make-up to element variation was investigated by thermodynamic calculation using ThermoCalc. Using the composition of WMA as a base individual elements were varied, utilising ranges for each of the elements as defined by the P92 alloy specification minimum values and maximum values (see Table 4.1). Each element was varied individually, with iron making up the balance. Figure 4.6 shows the effect of niobium content on the predicted fractions of the MX precipitates at 625°C. Figure 4.7 shows the elements that affect the precipitate fractions of the $M_{23}C_6$ and Laves Phases, with again, the predictions being made for a temperature of 625°C.

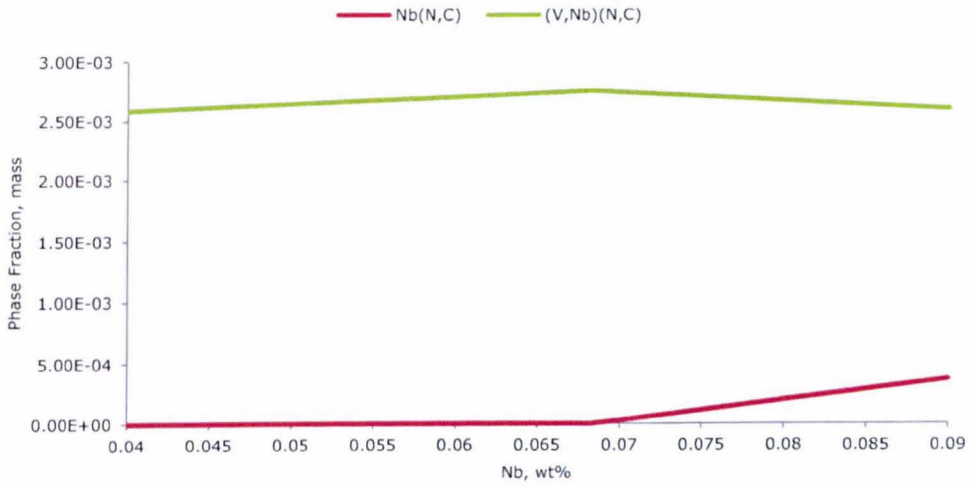

Figure 4.6 Phase fraction of the two types of MX as Nb content varies within the limits for P92 (all other elements at WMA levels), at a constant temperature of 625°C

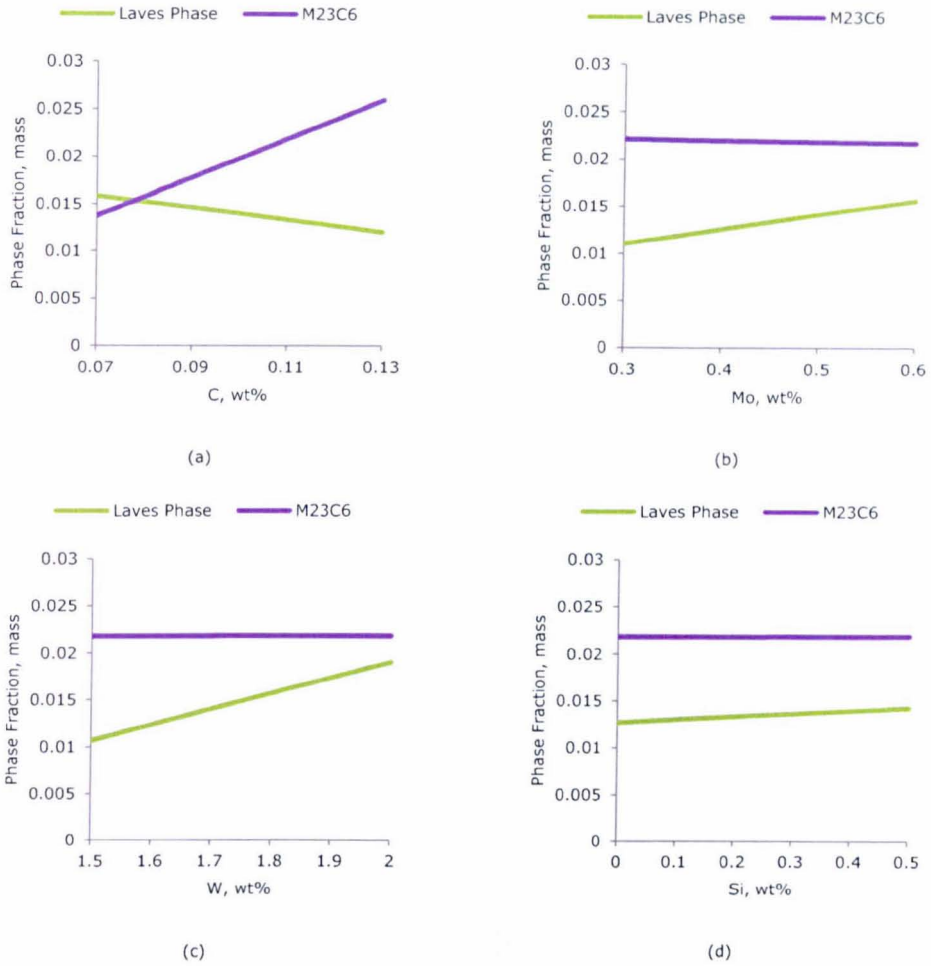

Figure 4.7 The effect of element variation on the precipitate fractions of Laves Phase and $M_{23}C_6$ at 625°C. Elements were varied within the P92 specification limits with the composition of WMA as a base. Only those elements that significantly affected precipitate fractions are shown

4.2 Weld Pad Microstructural Characterization

4.2.1 Optical Microscopy

Figure 4.8 shows OM images of the three weld metals in the as-received state (deposited and heat treated) sectioned perpendicular to the welding direction, which all have the expected martensite microstructure.

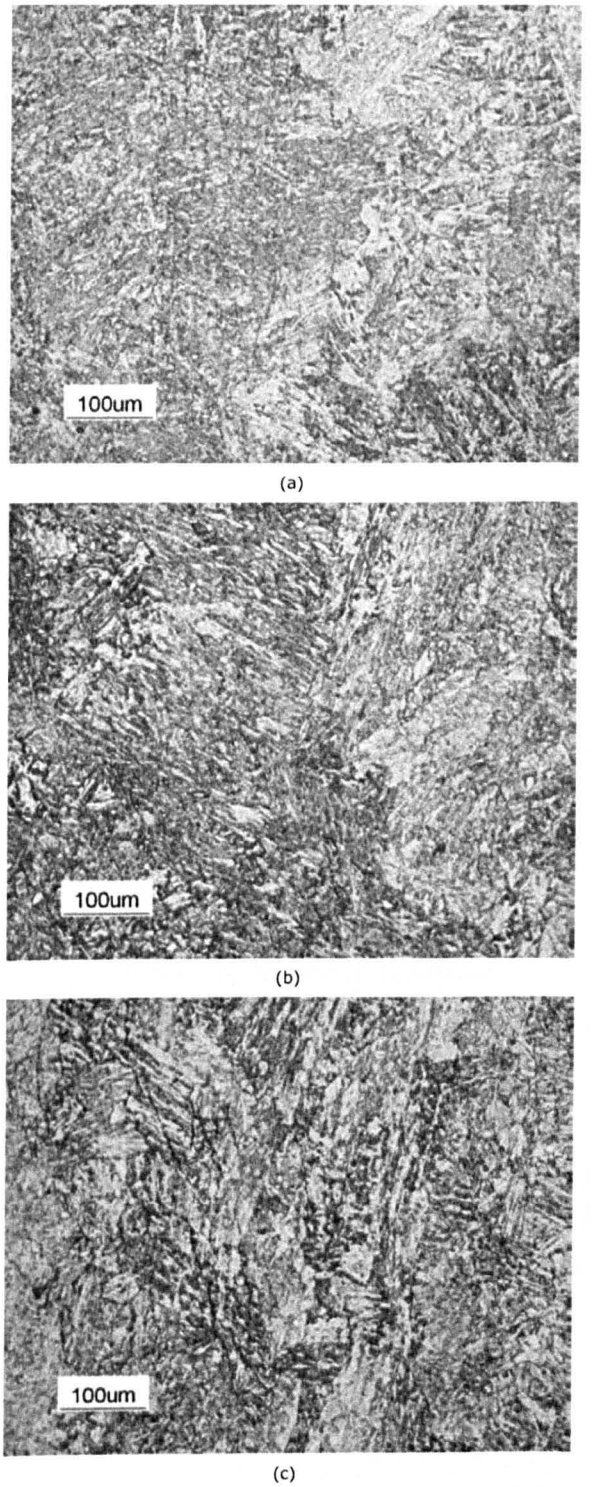

Figure 4.8 Optical micrographs of (a) WMA, (b) WMB, (c) WMC in the as-received (deposited and heat-treated) state

4.2.2 Hardness

Figure 4.9 gives a hardness profile for the three weld metals sectioned perpendicular to the welding direction over a distance of 15 mm which encompassed three weld beads, with intervals of 1mm between indents and a load of 200 gf. The average hardness was 294.2 kgf mm^{-2} for WMA, 280.8 kgf mm^{-2} for WMB and 297.4 kgf mm^{-2} for WMC. Notably, as well as being the material with the lowest hardness, WMB also had the greatest variation in hardness, with some very low hardness values being measured in this material.

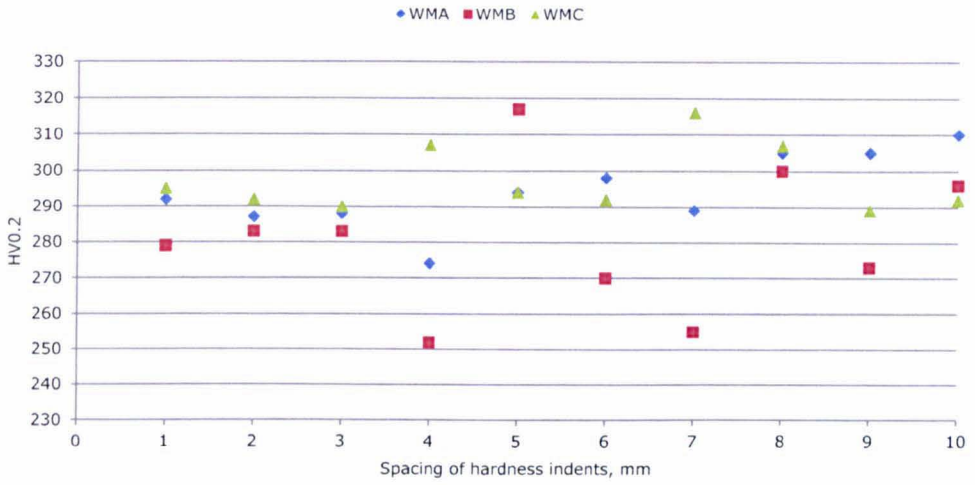

Figure 4.9 Hardness profiles of the three weld metals across three weld beads, with 1mm spacing between indents

4.2.3 SEM Characterization

Figure 4.10 shows SEM images (both BSE and SE images of the same regions) that were taken in order to characterize the precipitates present in the three weld metals in the as-received condition. BSE imaging shows that precipitates have a similar contrast to the matrix, especially the larger precipitates. EDX analysis revealed the larger precipitates to be chromium rich, indicating that these are $M_{23}C_6$. The other precipitates were too small to be analysed by EDX, but based on thermodynamic predictions and comparison with the literature (Abe et al. 2007; Sourmail 2001), it can be surmised that they are MX particles. No Laves phase was observed.

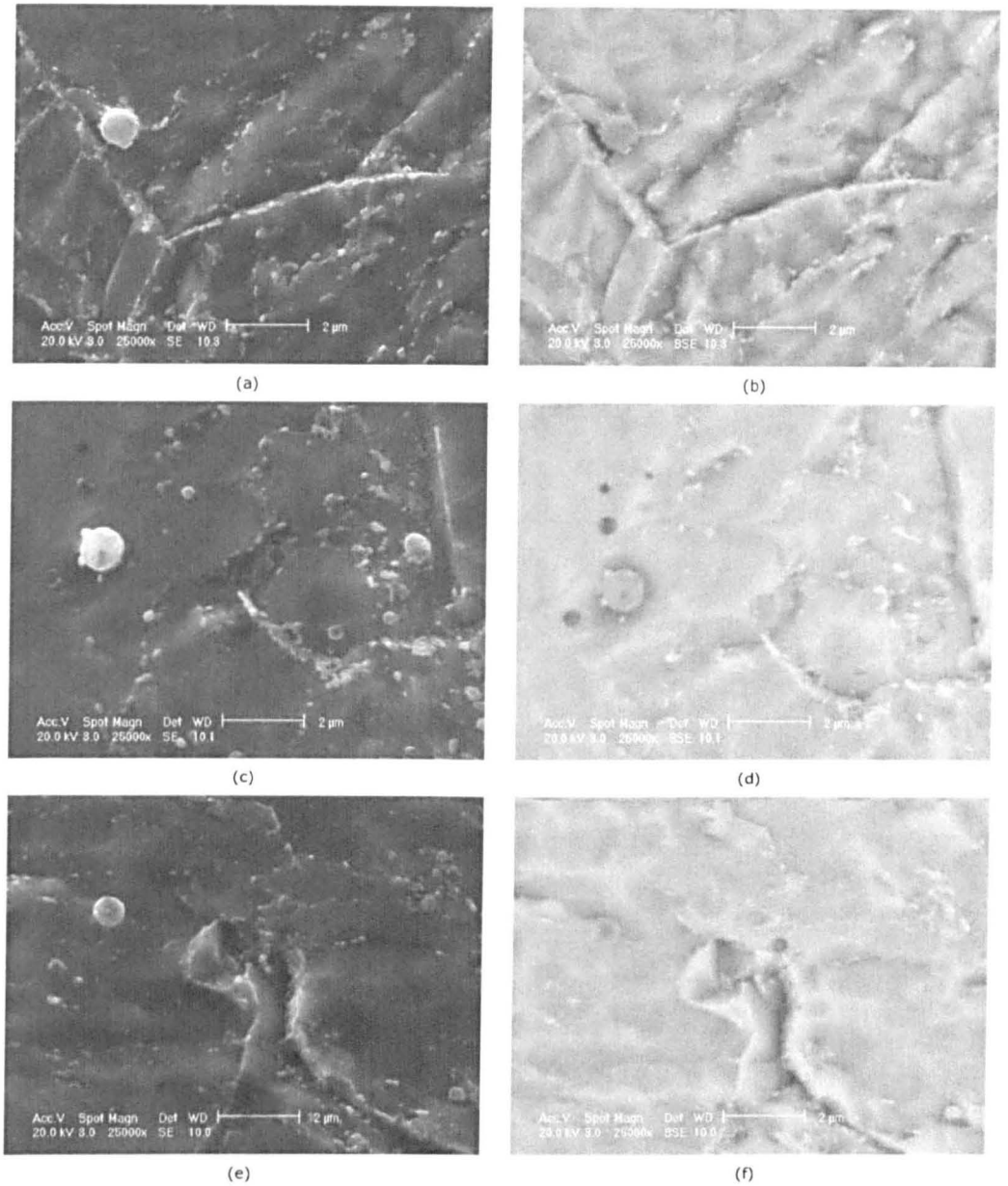

Figure 4.10 Pairs of SE and BSE images showing precipitation, large precipitates are $M_{23}C_6$ and smaller precipitates are MX. (a) and (b) WMA, (c) and (d) WMB, (e) and (f) WMC. Dark regions in the BSE images are a result of porosity

4.3 Austenite Formation During PWHT

Following modelling and initial characterisation of the three weld metals, the post-weld-heat-treatment conditions were investigated. The importance of PWHT was described in section 2.5.2, in particular the PWHT conditions which are currently recommended for welds in P92 steels. Initially, dilatometry was used to measure the Ac_1 of the three weld metals for comparison with the measured Ae_1 (4.3.1.1). Following this, ThermoCalc thermodynamic modelling was used to investigate the effect of individual elements on the A_1 temperature resulting in an equation to calculate the Ae_1 for weld consumables for use with P92 (4.3.1.4). The effect of PWHT temperatures on the α to γ transformation was investigated using a combination of ThermoCalc thermodynamic modelling (4.3.2.1), experimental simulation of PWHT and measurement of phase changes using dilatometry (4.3.2.2) and microstructural investigations of the resulting microstructures (4.3.2.3).

4.3.1 The Effect of Composition on A_1

4.3.1.1 Weld Metal Ac_1 and Ae_1

Figure 4.11 shows the measured dilatometric curves of the three weld metals, with their Ac_1 temperatures indicated (Ac_1 values where determined using the method shown in Figure 2.21). The results of dilatometric measurement of Ac_1 and equilibrium calculations of Ae_1 using ThermoCalc are shown in Table 4.3 (the Ae_1 values being taken from Table 4.2), along with the data for the parent P92, the composition of which can be found in Table 4.1. These data have been plotted (see Figure 4.12) as a function of the (Ni + Mn) content in order to investigate whether the recommendation that (Mn + Ni) < 1.5wt% (see section 2.5.2) is a sufficient condition to avoid the possibility of reaustenitization in these steels during PWHT (Marshall et al. 2002a) as it will ensure that the A_1 temperature will be above the selected PWHT.

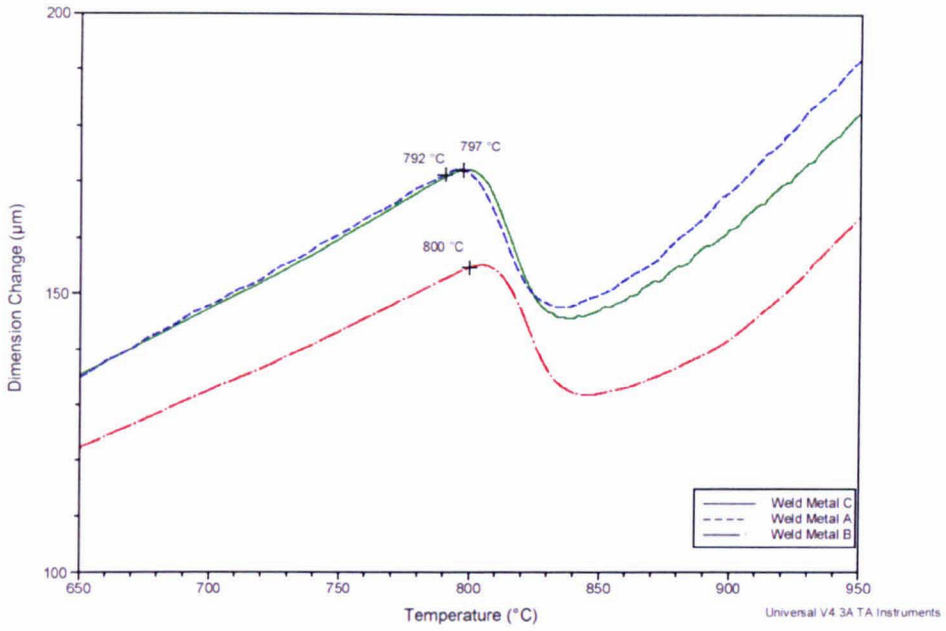

Figure 4.11 Dilatometric measurement of thermal expansion for the three weld metals examined in this work, with Ac_1 temperatures highlighted

Table 4.3 Ac_1 temperatures (measured by dilatometry) and Ae_1 temperatures for the parent P92 and three weld metals employed in this work. Ae_1 temperatures are determined from a single calculation in ThermoCalc where the phase fraction of austenite is set to 0.

	Ae_1 / °C	Ac_1 / °C
Parent P92	819	830
WM A	758	792
WM B	769	800
WM C	774	797

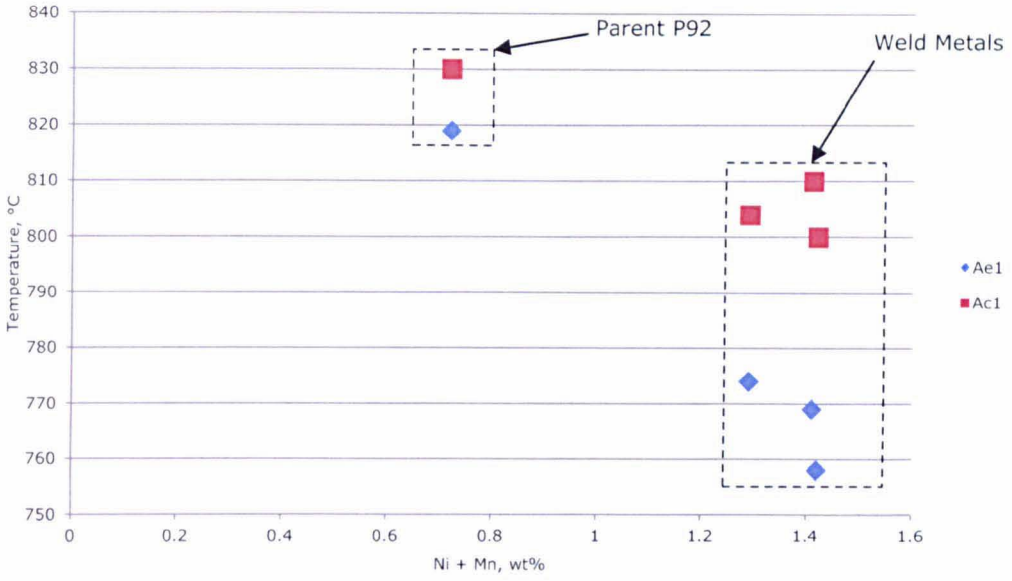

Figure 4.12 Ac_1 temperatures (measured by dilatometry) and Ae_1 temperatures (predicted with ThermoCalc) as a function of the (Ni + Mn) content of the steel for the parent P92 and the three weld metal types examined in this work

4.3.1.2 The Effect of Material Starting Condition and Heating Rate on the Ac_1

The parent P92 steel used in the investigations had already undergone a full normalizing and tempering heat treatment before the Ac_1 shown in Table 4.3 was measured. In order to investigate any possible effects that the previous heat treatments may have on the measured Ac_1, a heat treatment cycle was performed in which the steel was austenitized (Ac_1 being measured during the heating stage), cooled to form an untempered structure, then reaustenitized (with the Ac_1 being measured again on heating). The results of this experiment are shown in Figure 4.13.

The same experiment was repeated on a sample of WMA and the results are shown in Figure 4.14. The trendlines of the data were produced using an 8 point moving average.

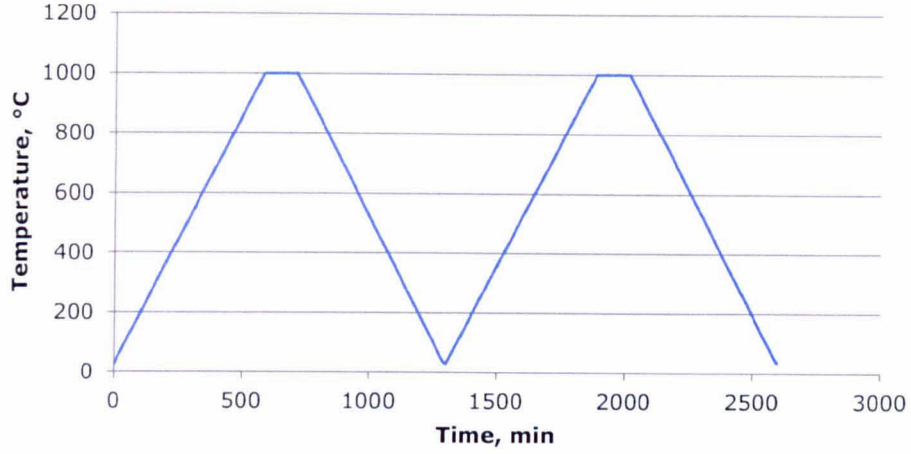

(a)

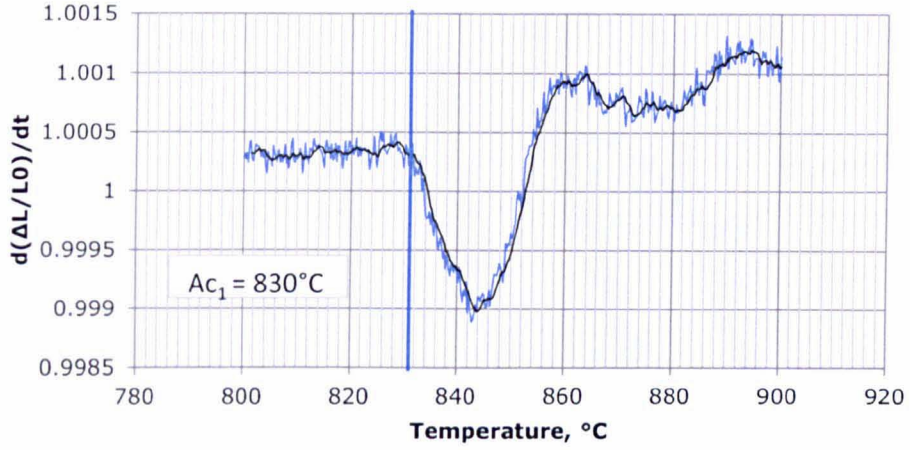

(b)

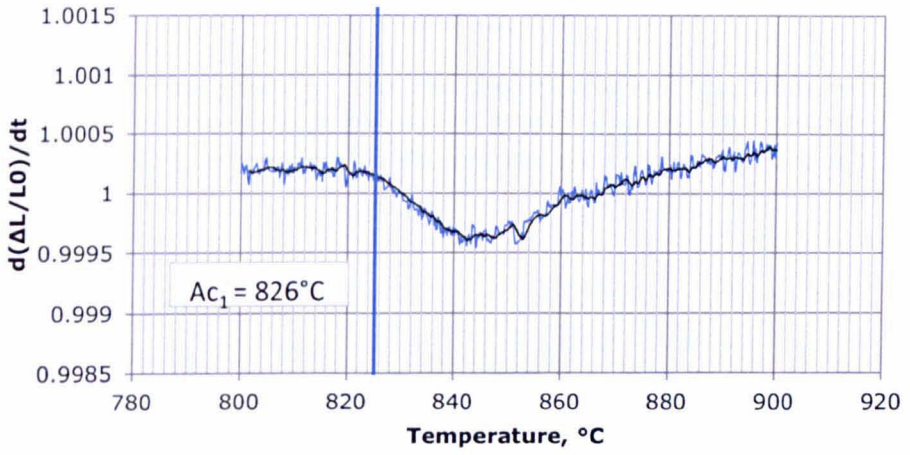

(c)

Figure 4.13 Thermal cycle (a) and Ac_1 measurement of parent P92 during (b) the first heating cycle and (c) the second heating cycle

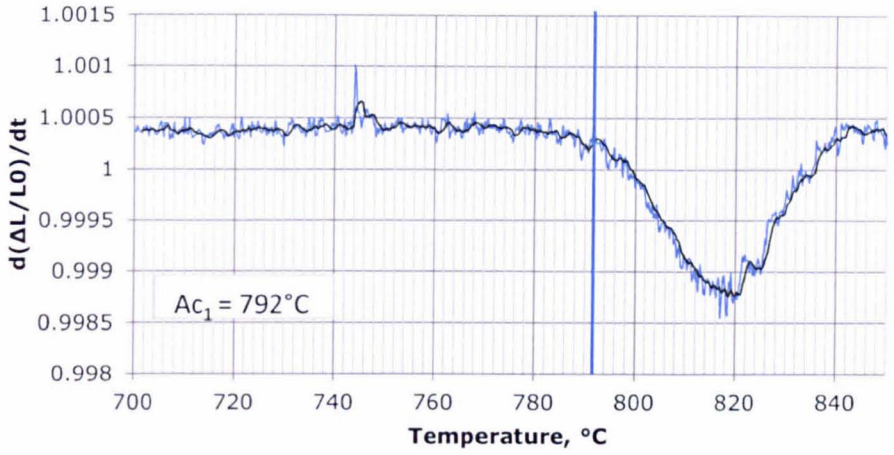

(a)

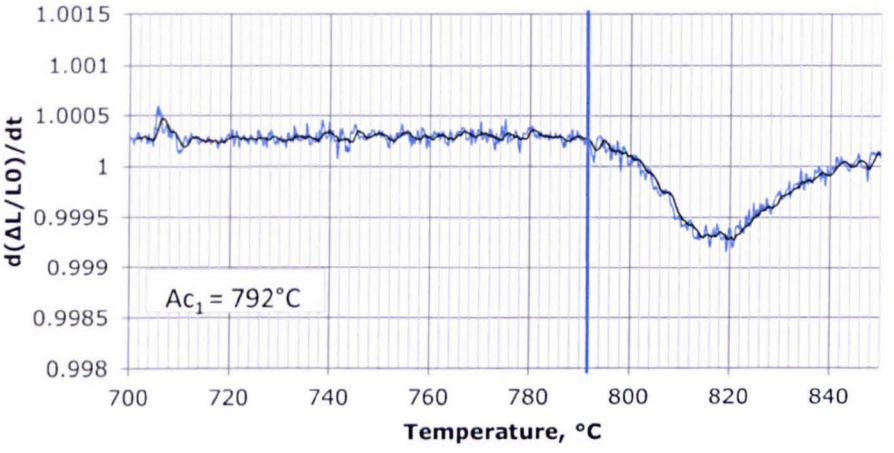

(b)

Figure 4.14 Ac_1 measurement of WMA during (a) the first heating cycle and (b) the second heating cycle

The effect of the heating rate on the measured Ac_1 value was also investigated for the parent metal and WMA. Heating rates of 100°C/hr, 50°C/hr and 20°C/hr were used. The results are shown in Figure 4.15.

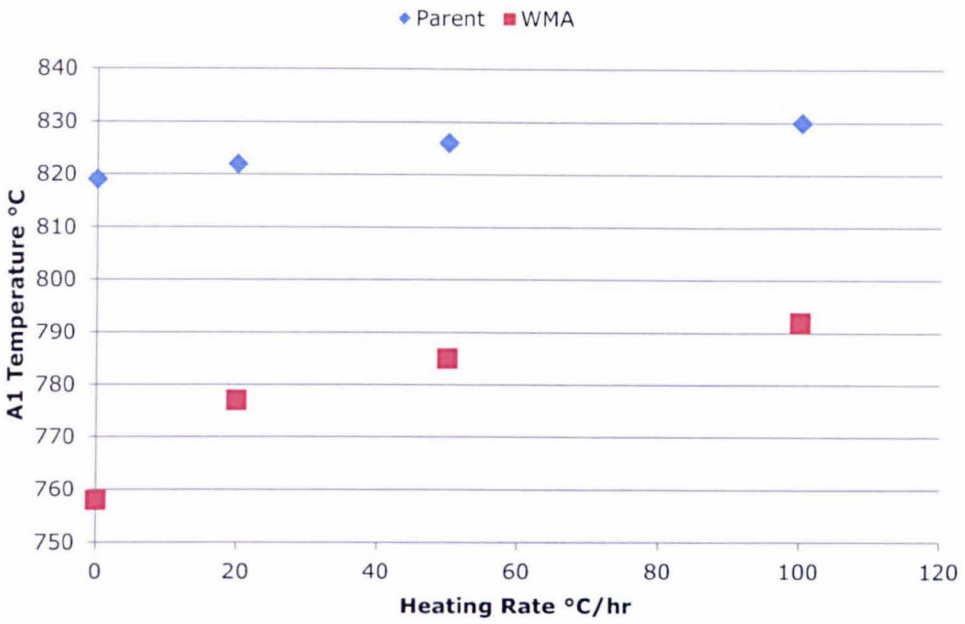

Figure 4.15 The effect of heating rate on measured Ac_1 temperature for parent P92 steel and weld filler metal (WMA) chosen for later creep tests. The values with a heating rate of zero represent the calculated Ae_1 values.

4.3.1.3 The Effect of Element Variation on Ae_1

ThermoCalc was used to investigate which elements have the greatest effect on the predicted A_1 temperature. Initially, a base composition for P92 steels was required for which a baseline Ae_1 temperature could be defined. Table 4.4 shows the allowed minimum and maximum compositions of each element according to the parent P92 specification with increased limits for manganese and nickel, as well as additional elements such as cobalt and copper that are present in weld metals (Richardot et al. 2000a). The base composition from which the variations of elemental compositions were to be made was defined as being the mid-point of each elements range and is also identified in Table 4.4. Using this composition, a base value for the Ae_1 was established as being 800.6°C. The compositions of individual elements were then varied in turn to their maximum and minimum allowable compositions according to the specification limits indicated in Table 4.4 while all other elements remained at the base value with the iron content making up the balance, and the Ae_1 temperature of these compositions predicted using ThermoCalc. The influences of the individual elements (across the range of the specification composition for the element) are shown in Figure 4.16.

Table 4.4 Minimum and maximum compositions of each element according to the parent P92 specification with increased limits for Mn, Ni and the addition of Co and Cu. The selected composition was used as a base from which to investigate the effect of individual elements on Ae_1 when varied between the maximum and minimum.

Name	C	N	B	Si	Mn	P	S	Cr	Mo	Ni	Co	Cu	Nb	V	W
Weld minimum	0.07	0.02	0.001	0.001	0.3	0.001	0.001	8.5	0.3	0.001	0.001	0.001	0.04	0.15	1.5
Weld maximum	0.13	0.07	0.007	0.5	1.0	0.02	0.01	10.0	1.5	0.7	1.1	0.04	0.09	0.25	2.0
Selected composition	0.1	0.045	0.004	0.25	0.65	0.011	0.006	9.25	0.9	0.351	0.551	0.021	0.065	0.2	1.75

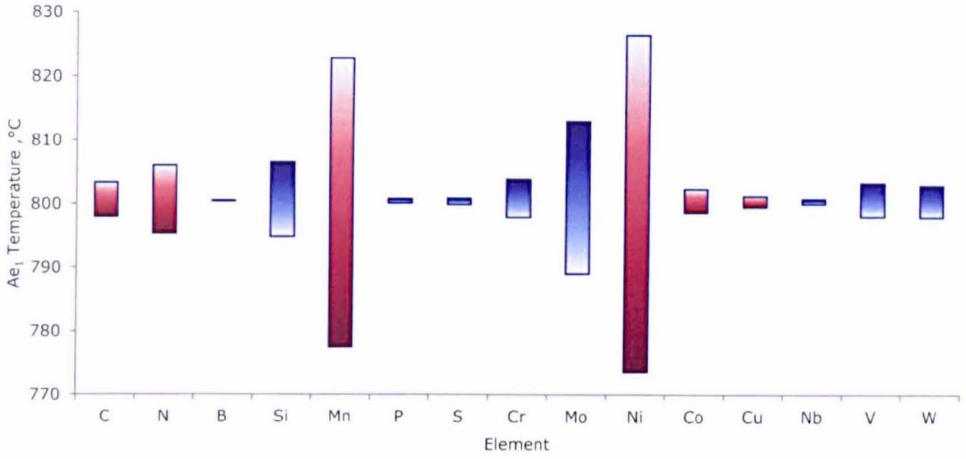

Figure 4.16 Effect of individual element variation from their base levels to the P92 specification limits on the Ae_1 temperature. Dark shading within the bars indicates the element at its maximum allowable composition whilst the light shading within the bar indicates its minimum composition. Red bars are austenite stabilizers, blue are ferrite stabilizers.

It is shown that in all cases, the values of the Ae_1 temperature predicted with ThermoCalc varied approximately linearly with the composition of individual element between the minimum and maximum values defined for that element in the specification (the method used was the same as that published by Santella (Santella 2010). In addition, simultaneous variations of multiple elements were also conducted; it was shown that the variation in Ae_1 with each element was essentially independent of variations made in other elements. Accordingly, the Ae_1 temperature sensitivity for each element within the compositional range could be calculated independently, and values for these are shown as the element coefficients in Equation 4.1. The elements that have a negative Ae_1 temperature sensitivity result in reduction in the Ae_1 temperature with increasing element composition in the alloy and vice versa.

4.3.1.4 An Equation for Calculating Ae_1 in P92

Equation 4.1 predicts the Ae_1 temperature for any alloy within the compositional range shown in Table 4.4, as follows:

$$Ae_1(°C) = 809.7 - 99.5C - 196.4N - 67.4Mn - 78.8Ni - 9.85Co - 47.2Cu + 20B + 10.9Si + 35.8P + 95.6S + 3.7Cr + 19.7Mo + 31.4Nb + 53.8V + 10.6W$$

Equation 4.1

where the symbols indicate the composition (wt%) of that alloying element in the alloy in question (within the range for P92 steels as defined in Table 4.4). The equation was derived by first using ThermoCalc and the selected composition in Table 4.4 to calculate a value of Ae_1 (corresponding to 809.7°C). Following this, each element was individually varied to its maximum allowable value and minimum allowable value and the corresponding Ae_1 calculated. In this way, elements that increased or decreased the Ae_1 temperature were identified. The element coefficients correspond to the increase/decrease in Ae_1 temperature that a 1 wt% increase in that element would give. Table 4.5 shows a comparison of the Ae_1 temperatures directly calculated using ThermoCalc compared with those calculated with Equation 4.1 (itself generated from ThermoCalc outputs) for the compositions of the materials of interest in this work (shown in Table 4.1) and for two parent P92 steels where a detailed composition was available in the literature. It is again notable that across the three weld consumables employed in this work, a difference in the Ae_1 values of 13°C is predicted by Equation 4.1, which is slightly higher than the 8°C difference in measured Ac_1 as shown in Figure 4.12.

Table 4.5 Comparison of Ae_1 temperatures of seven compositions of P92 steel both from use of Equation 4.1 and by direct calculation with ThermoCalc

Name	Ae_1 eq. 4.1(°C)	Ae_1 TCW (°C)
Selected Comp.	800	800
Parent P92 Sawada (Sawada et al. 2001b)	816	819
P.J. Ennis (Ennis et al. 2000)	821	817
WMA	828	821
WMB	758	758
WMC	769	769
	771	774

4.3.2 PWHT Temperature Dependence

Due to the difference between the calculated values of Ae_1 and measured value of Ac_1 for the range of materials examined (see Figure 4.12), an investigation into the use of calculated Ae_1 and measured Ac_1 temperatures as a means to identify suitable conditions for PWHT was conducted. Samples from WMA were machined into specimens for dilatometry (see section 3.1.6) and a cycle simulating a PWHT was conducted which involved heating at a rate of 100°C/hour, holding at a set temperature for 180 min and then cooling at 50°C/hour (these rates were determined using BSI "2633:1987 Specification for Class I arc welding of ferritic steel pipework for carrying fluids" and discussions with Supergen industrial partners). The hold temperatures selected were 760°C (typical of PWHT for these weld types) and then a range of higher hold temperatures (namely 770°C, 780°C, 800°C, and 820°C) chosen to examine the role of hold temperature on the austenitization of the welds and the subsequent microstructural characteristics following cooling to room temperature. The use of these temperatures was designed to provide insight into the effects of PWHT at erroneously high temperatures on the weld metal properties.

4.3.2.1 Thermodynamic Modelling of the α→γ Transformation

Figure 4.17 shows the transformation of ferrite to austenite as calculated by ThermoCalc for WMA, showing that under equilibrium conditions these test temperatures lie between Ae_1 and Ae_3 (volume fraction is presented to enable comparison with dilatometer results).

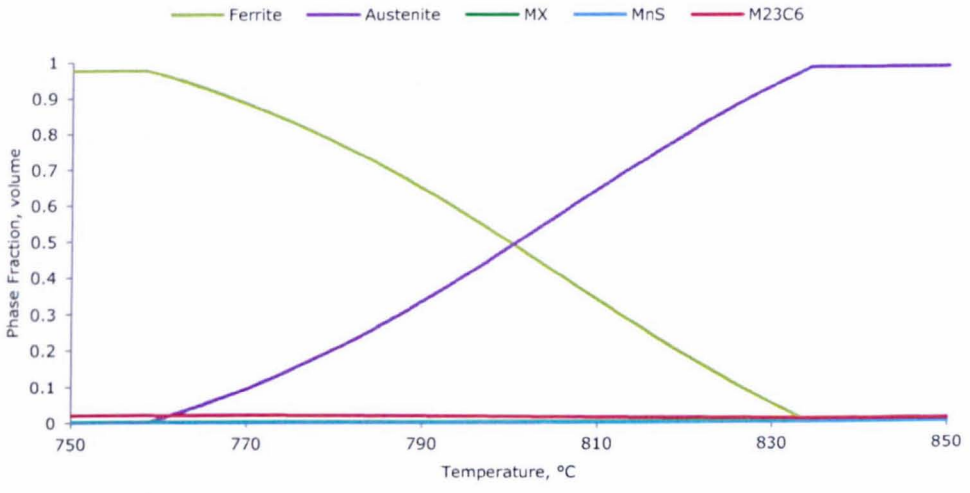

Figure 4.17 The transformation of ferrite to austenite under equilibrium conditions, as calculated by ThermoCalc for WMA

4.3.2.2 Measurement of Austenite Formation During PWHT

In order to experimentally quantify the phase fractions of ferrite and austenite from the dilatometric curves, the lever rule was used. This involves first determining the thermal expansion of ferrite and austenite. A sample of WMA was heated at a rate of 100°C/hr from room temperature to 1000°C in order to ensure that complete transformation had taken place. The length change was measured using the dilatometer and the result of this is shown in Figure 4.18. Temperature is shown on the x-axis while strain, derived from the change in length ΔL divided by the original length L_0, is on the y-axis. The thermal expansion of the individual phases is represented by the extended linear sections.

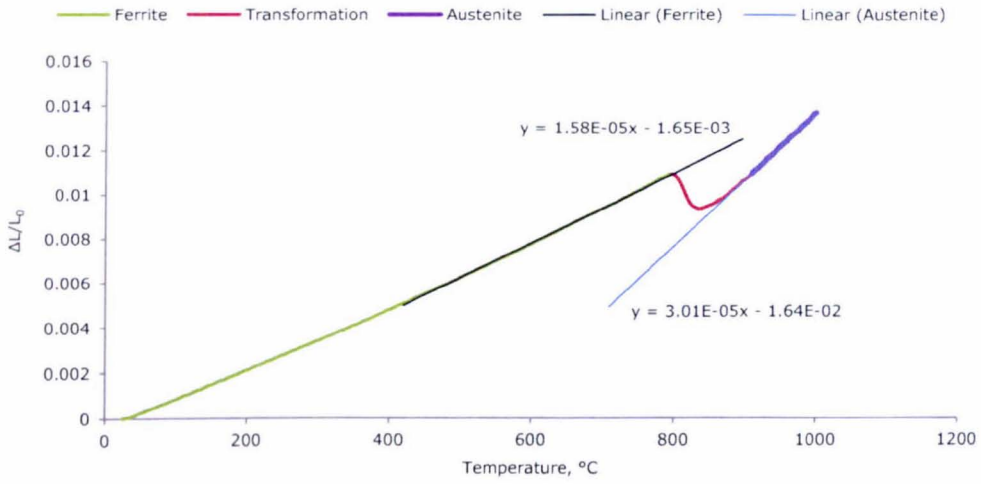

Figure 4.18 Thermal expansion during continuous heating at 100°C/hr of ferrite and austenite for WMA samples

The following figures show the dilatometer curves at the tested hold temperatures.

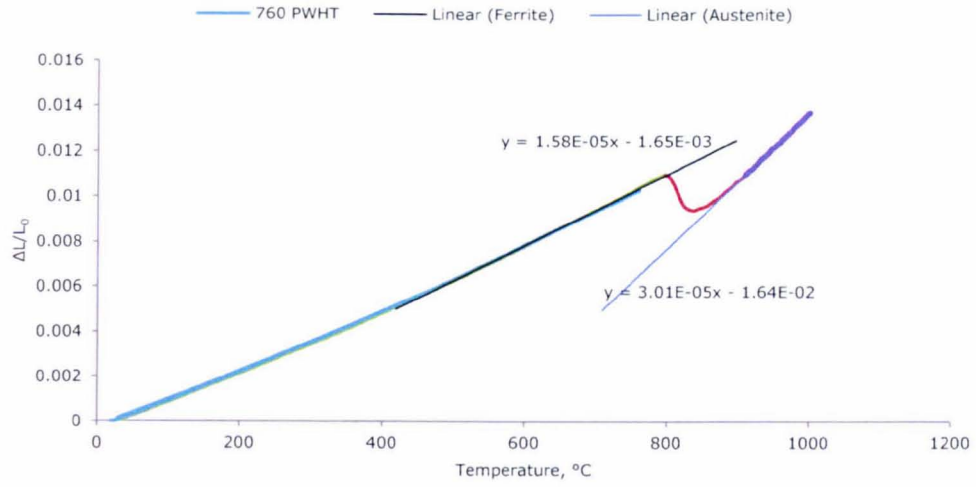

Figure 4.19 Dilatometer curve of the 760°C PWHT of WMA. The dilatometry data for an equivalent sample heated through to 1000°C (From Fig. 4.18) is also plotted for comparison.

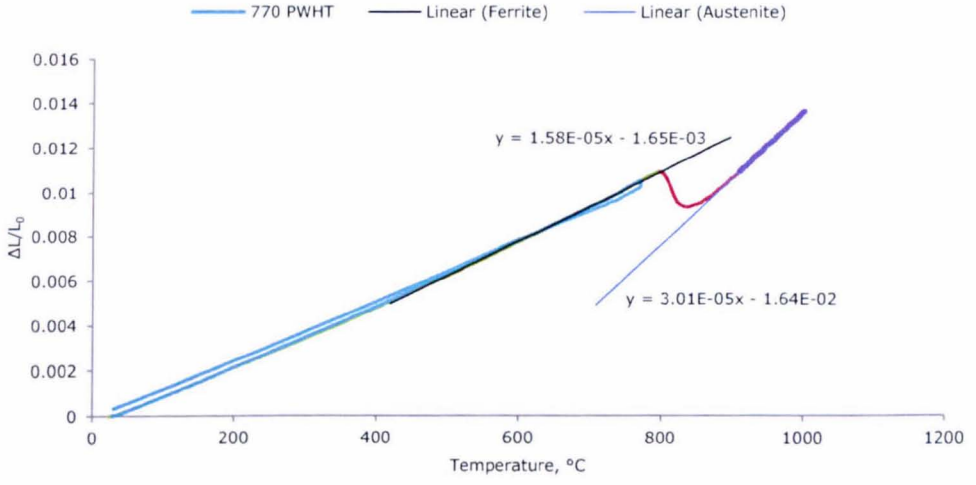

Figure 4.20 Dilatometer curve of the 770°C PWHT of WMA. The dilatometry data for an equivalent sample heated through to 1000°C (Figure 4.18) is also plotted for comparison.

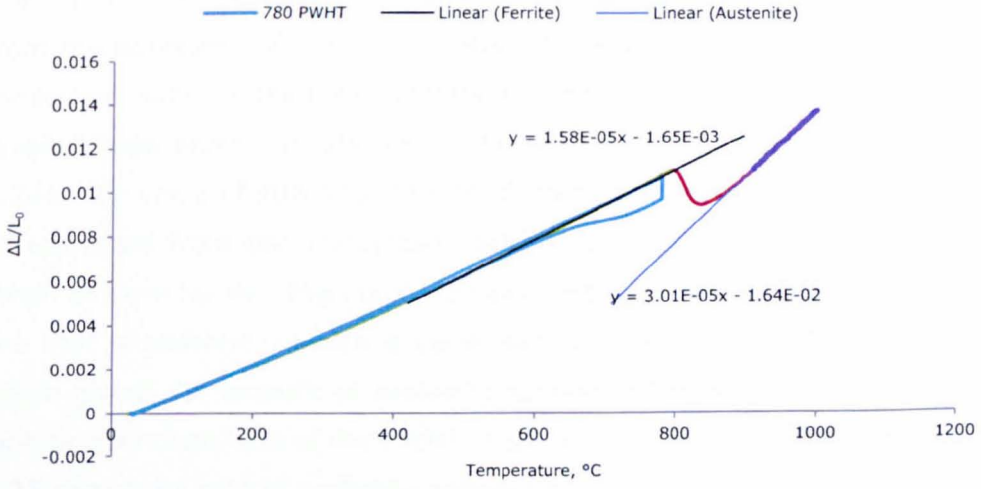

Figure 4.21 Dilatometer curve of the 780°C PWHT of WMA. The dilatometry data for an equivalent sample heated through to 1000°C (Figure 4.18) is also plotted for comparison.

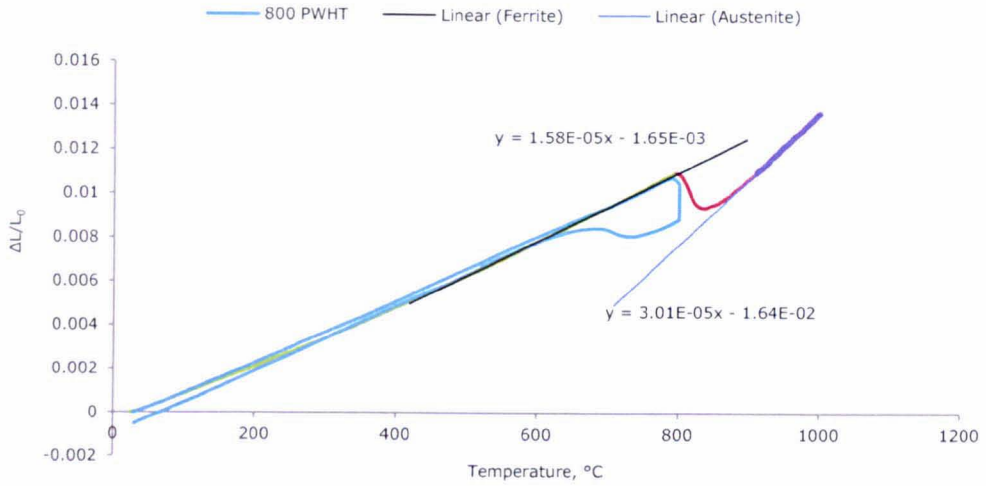

Figure 4.22 Dilatometer curve of the 800°C PWHT of WMA. The dilatometry data for an equivalent sample heated through to 1000°C (Figure 4.18) is also plotted for comparison.

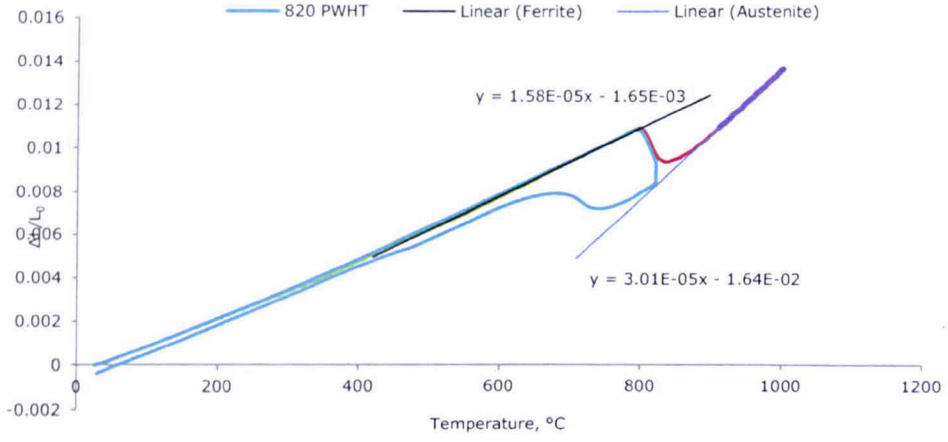

Figure 4.23 Dilatometer curve of the 820°C PWHT of WMA. The dilatometry data for an equivalent sample heated through to 1000°C (Figure 4.18) is also plotted for comparison.

The value of strain for pure ferrite and pure austenite can be calculated from the equations of linear expansion. A line can then be drawn between these two lines or their extrapolations (the ferrite-austenite tie-line at a given temperature) as shown in the schematic diagram below (Figure 4.24). The value of strain for the PWHT sample after the 180 min hold can be extracted from the dilatometer data. This value is subtracted from the strain of pure ferrite. The resulting value represents the portion of the tie-line that is austenite, which is converted to a percentage of the line as a whole giving the amount of austenite formed in the weld metal during the high temperature hold of the PWHT. Table 4.6 shows the results and Figure 4.25 shows the rate of austenite formation.

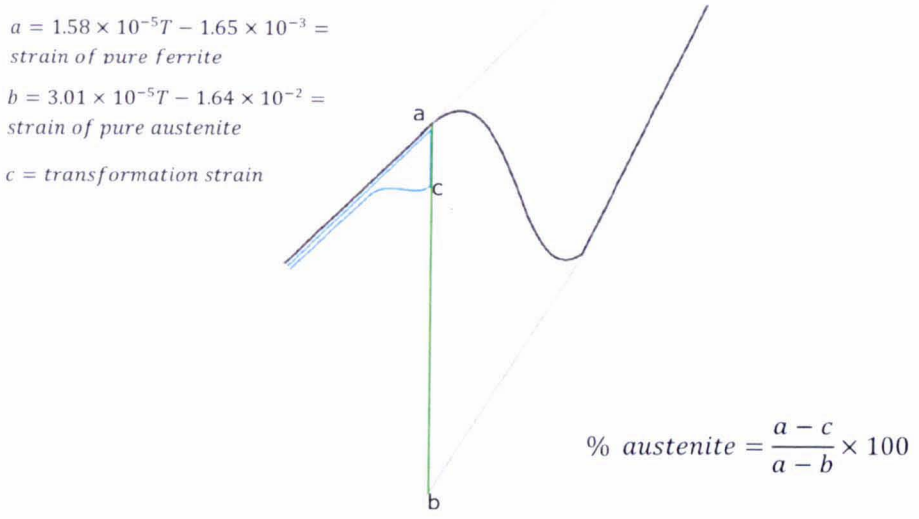

Figure 4.24 Schematics showing how the value of strain for pure ferrite and pure austenite can be calculated from the equations of linear expansion and then used to calculate the percentage of austenite at that temperature

Table 4.6 Amount of austenite after 180min at the hold temperature, before cooling

PWHT Conditions, °C	% Austenite	% Austenite predicted by ThermoCalc
760	1.5	1.5
770	8.3	9.9
780	29.5	31.6
800	61.3	63.7
820	84.4	88.4

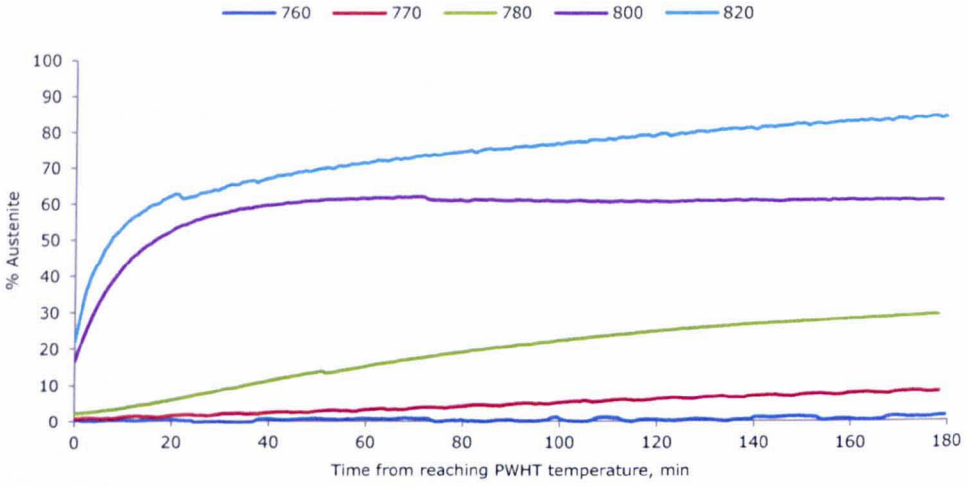

Figure 4.25 The rate of austenite formation upon reaching the specified PWHT temperature

4.3.2.3 Microstructure Following PWHT

Hardness tests were carried out following the simulated PWHT and the results of this are shown in Figure 4.26. Ten indents were taken at a spacing of 1 mm along the vertical axis of the samples. The average hardness was 263.5 kgf mm^{-2} for 760°C, 256.1 kgf mm^{-2} for 770°C, 237.8 kgf mm^{-2} for 780°C, 213.8 kgf mm^{-2} for 800°C and 208.3 kgf mm^{-2} for 820°C. Figure 4.27 shows optical images of the microstructures of the weld metals. In order to identify material that transformed to austenite, EBSD imaging of the microstructures was carried out and the results of this are presented in Figure 4.28 showing the mostly martensitic microstructure at 760°C (a) developing to an equiaxed microstructure at 820°C (d).

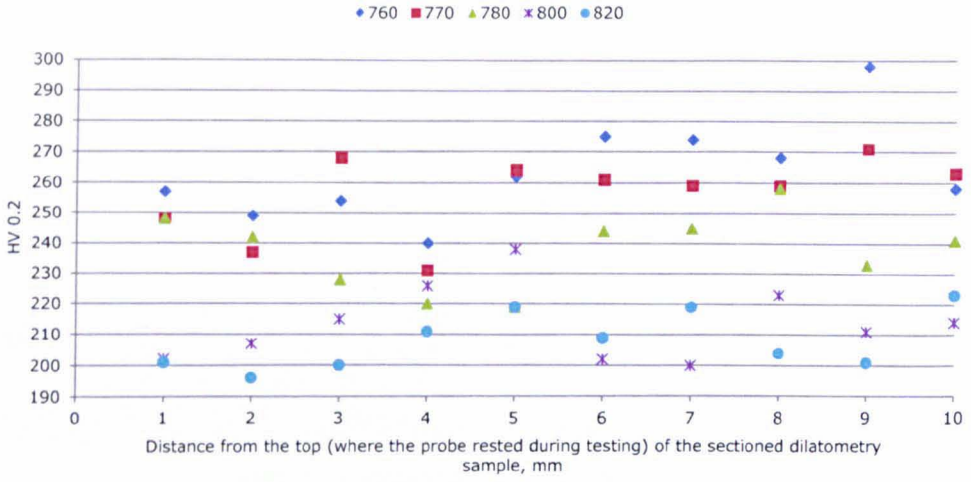

	Temperature, °C				
	760	770	780	800	820
Mean Hardness	263.5	256.1	237.8	213.8	208.3
Standard Deviation	16.3	13.2	12.6	12.2	9.4

Figure 4.26 Hardness profile of the weld metal after the simulated PWHT. The numbers in the legend indicate the hold temperature in °C

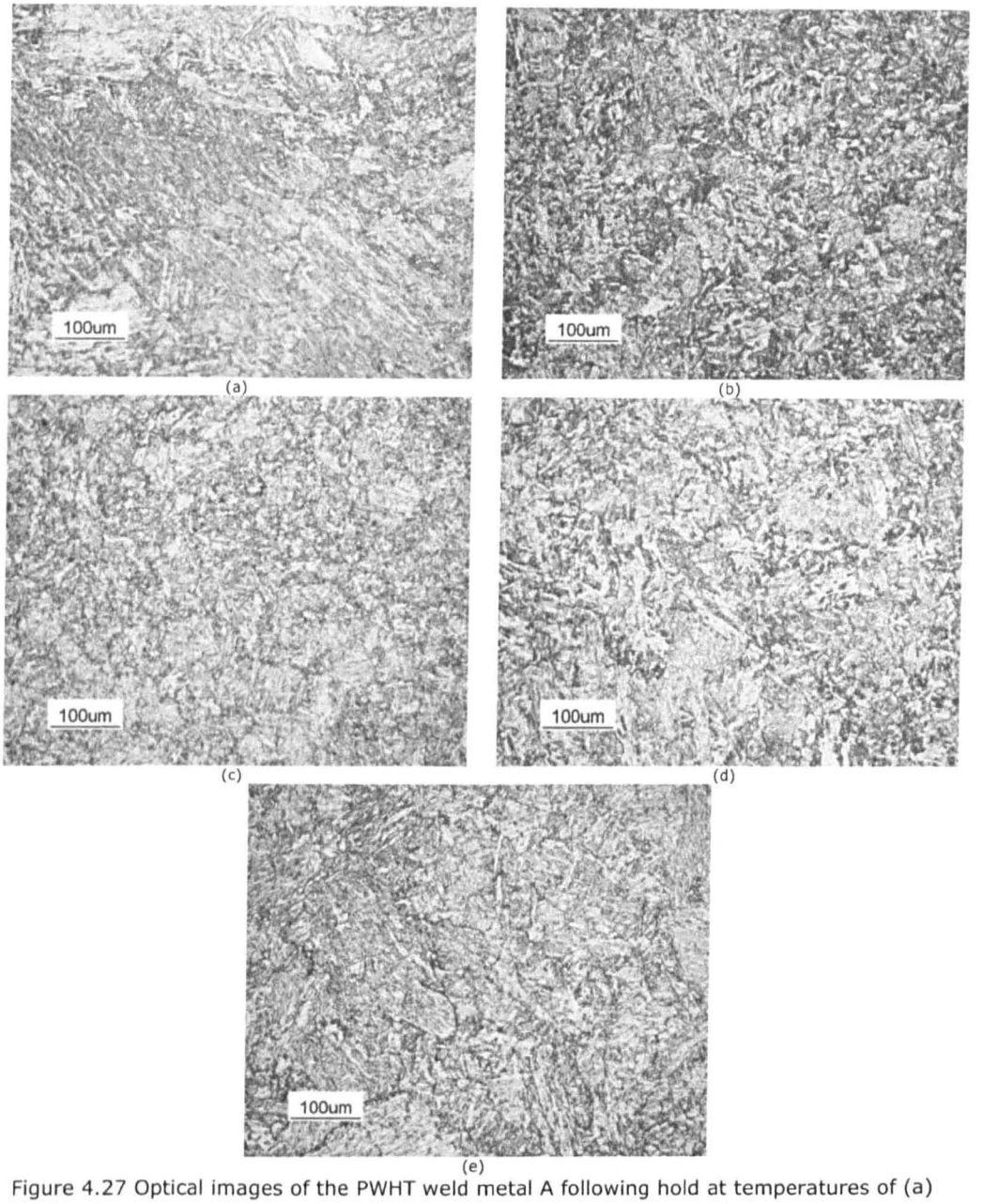

Figure 4.27 Optical images of the PWHT weld metal A following hold at temperatures of (a) 760°C, (b) 770°C, (c) 780°C, (d) 800°C and (e) 820°C . Each image shows a clearly visible martensite microstructure but limited visible evidence of other transformation products

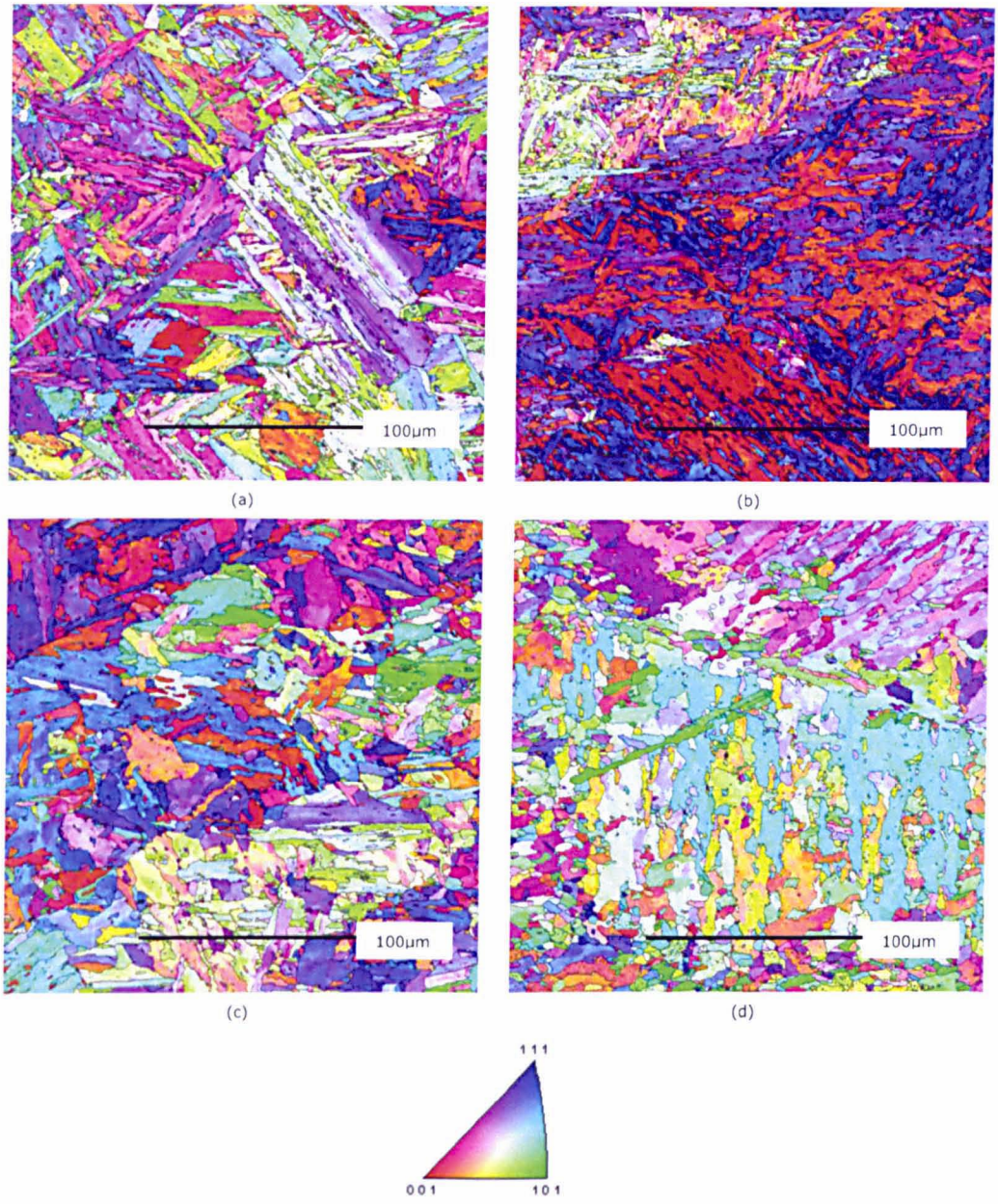

Figure 4.28 200µm x 200µm inverse pole figure EBSD images of the weld metals after PWHT at (a) 760°C, (b) 770°C, (c) 780°C, (d) 820°C; (e) shows the inverse pole figure key. Using EBSD clearly shows a more equiaxed grain structure in (c) and (d) resulting from transformation to austenite during PWHT and recrystallisation during cooling

4.4 Weld Consumable Creep Testing

4.4.1 Creep Test Results

Creep tests were performed in air at three different temperatures and nominal stress conditions, given in Table 4.7. Constant uniaxial tensile loading was applied in the direction of the specimen axis, transverse to that of welding. Strain measurement over the gauge length was regularly logged using output from extensometers. The recorded rupture times and failure strains are presented in Table 4.7, and the full set of strain-time curves can be seen in Figure 4.29.

Table 4.7 Weld metal creep test results

Weld Metal	Temp. (°C)	Stress (MPa)	Rupture Time (h)	Failure Strain (%)
A	625	150	2240	10
A *	625	150	1669	9
B	625	150	1301	4
C	625	150	1609	21
A	625	170	1090	15
B	625	170	656	7
C	625	170	696	16
C (rpt)	625	170	574	15
A *	670	90	983	14
B	670	90	668	3
C	670	90	865	14

* - tested by Corus UK Ltd., (rpt) - repeat test

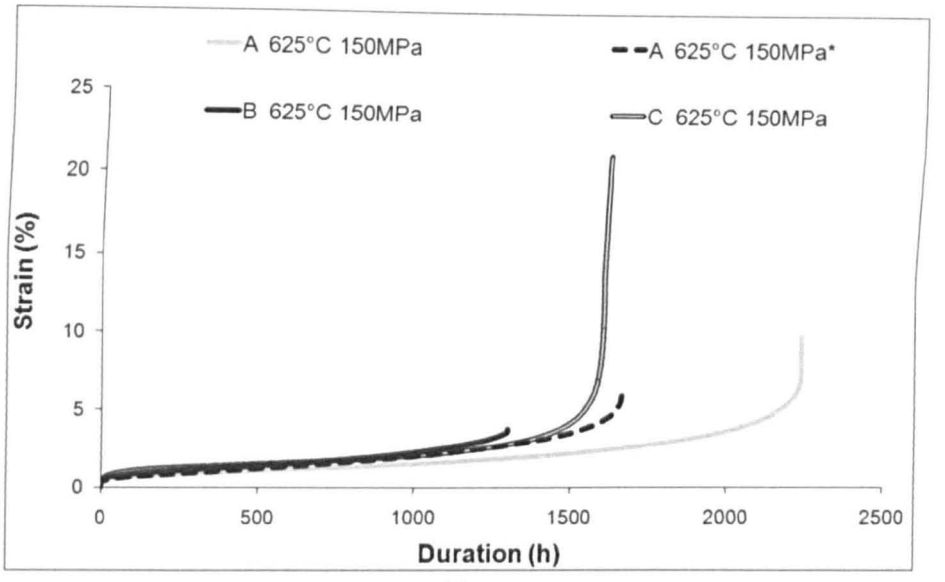

(a)

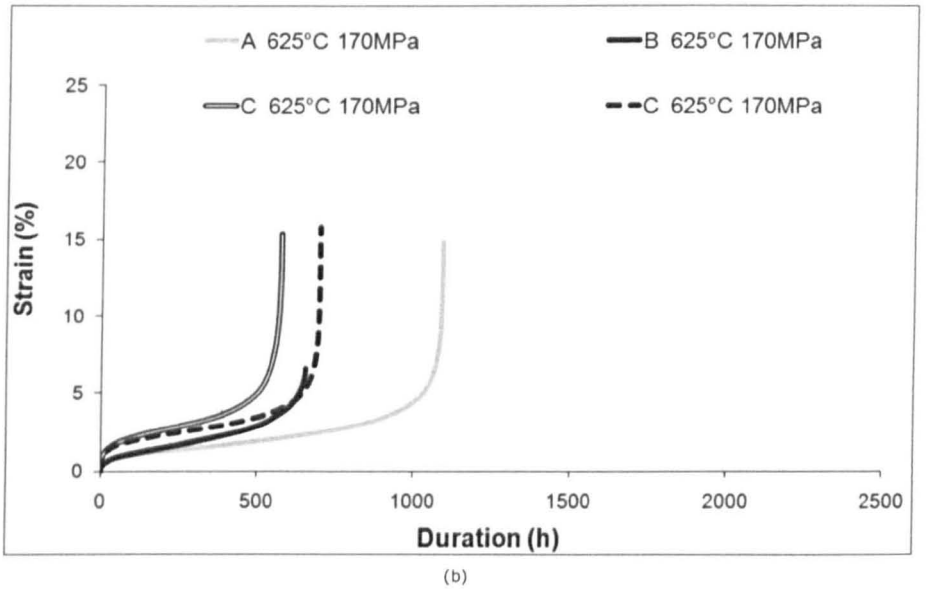

(b)

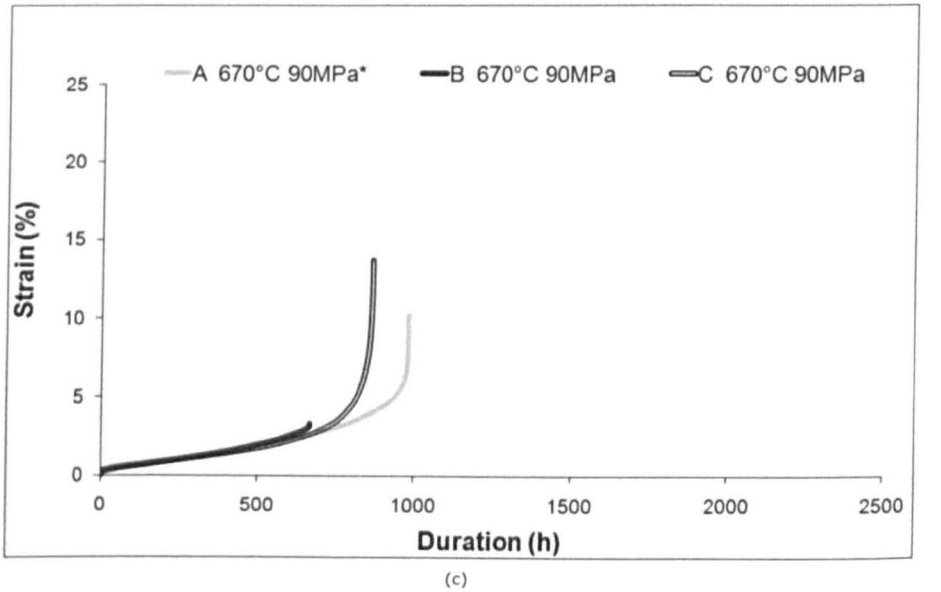

(c)

Figure 4.29 Strain-time curves for all creep test conditions; (a) 625°C 150MPa, (b) 625°C 170MPa and (c) 670°C 90MPa

It was found that specimens removed from the weld pad made using consumable electrode A (i.e. WMA) gave consistently longer rupture times for all test conditions. WMB had the shortest time to rupture, exhibiting only 60% of the creep life of weld metal A at the higher stress (150 and 170MPa) tests, with little tertiary creep and comparatively poor ductility. WMC exhibited a decrease in the time to rupture at the highest stress (170MPa), and an unusually high amount of primary creep strain (Figure 4.29b). A repeat test confirmed the consistency of the markedly different primary creep behaviour of WMC at 625°C/170 MPa. This repeat test also gives an indication of the amount of scatter present in the results.

As to be expected, the time to rupture of all three weld metals decreased with increasing temperature, and the rupture times at 625°C/170 MPa and 670°C/90 MPa are broadly the same. At 670°C under a more realistic power plant operating stress of 90 MPa (but at a much higher temperature than would be experienced in a plant environment), the rupture times of the three weld metals are relatively closer together; however, the failure strain of WMB remained significantly lower than that of WMA and WMC.

Minimum creep strain rate, $\dot{\varepsilon}_{\min}$ and time to rupture, t_r, are often found to be related through the Monkman-Grant equation (Equation 4.2):

$$(\dot{\varepsilon}_{\min})^a \cdot t_r = k_{MG}$$

Equation 4.2

where k_{MG} is the Monkman-Grant constant for the material and a is material constant, typically about 1.0. If a material conforms to this relationship, this may be regarded as evidence that the controlling mechanisms for deformation and fracture are essentially the same over the range of test conditions examined (Anderson et al. 2003).

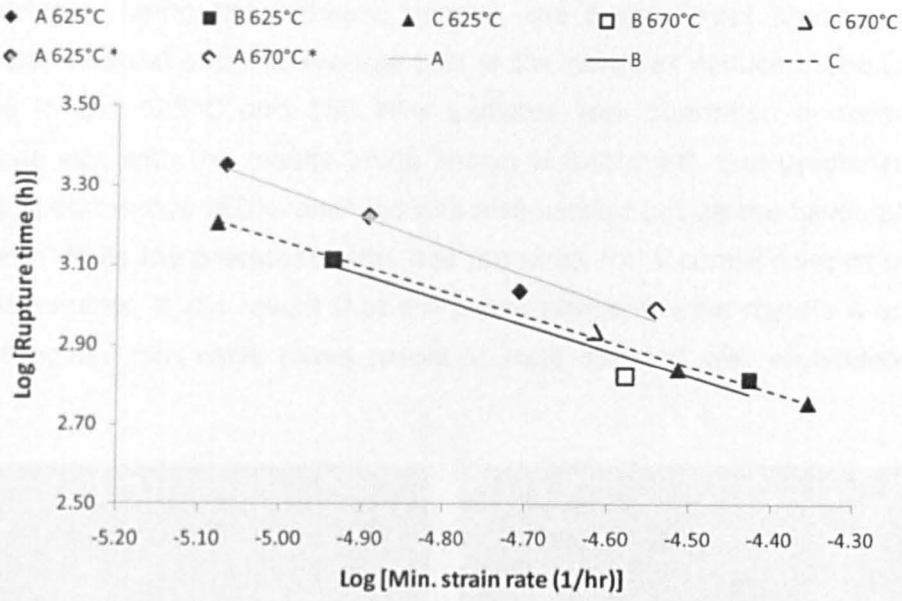

Figure 4.30 Creep rupture times against minimum strain rates (log-log) for weld metals A, B and C

Figure 4.30 shows the data plotted in the form of Equation 4.2. It can be seen that over the limited range of test conditions examined, all three weld metals exhibit the same creep mechanisms and predictions of rupture time could be made using the minimum strain rate and the Monkman-Grant relation. It is also evident from Figure 4.30 that WMA exhibited a greater rupture time for the same minimum strain rate compared to WMB and WMC.

4.4.2 Microstructure Following Creep

Following creep rupture, microstructural examination of the failed creep specimens was performed parallel to the applied stress. Figure 4.31 shows the microstructures of the three weld metals after testing at 625°C and 150 MPa. The weld metals under all test conditions contained MX, $M_{23}C_6$ and Laves phase. In Figure 4.31 pairs of secondary electron (SE) and back scattered electron images (BSE) are shown. BSE images help differentiate precipitates; Laves phase has a high contrast to the matrix, showing high brightness (due to its high mean atomic number), while $M_{23}C_6$ has a contrast level similar to that of the matrix. The smaller precipitates are MX. Of particular interest was any difference in the size and precipitation of Laves phase between the three weld metals. A method described by Korcakova (Korcakova et al. 2001) enables the quantification of Laves phase using SEM images. Due to the high mean atomic number of Laves phase (due to high concentrations of tungsten and molybdenum), it appears much brighter on BSE images compared to the matrix and other

precipitates. Using the software ImageJ, the bright Laves phase can be isolated, counted and the average size of the particles deduced. The Laves phase in the 625°C and 150 MPa samples was quantified in terms of average size with the results being shown in Table 4.8. Energy-dispersive X-ray spectroscopy (EDX) analysis was also carried out on the Laves phase present. While the precipitate size was too small for accurate compositional measurements, it did reveal that the Laves phase in weld metals A and B was tungsten-rich while Laves phase in weld metal C was molybdenum-rich.

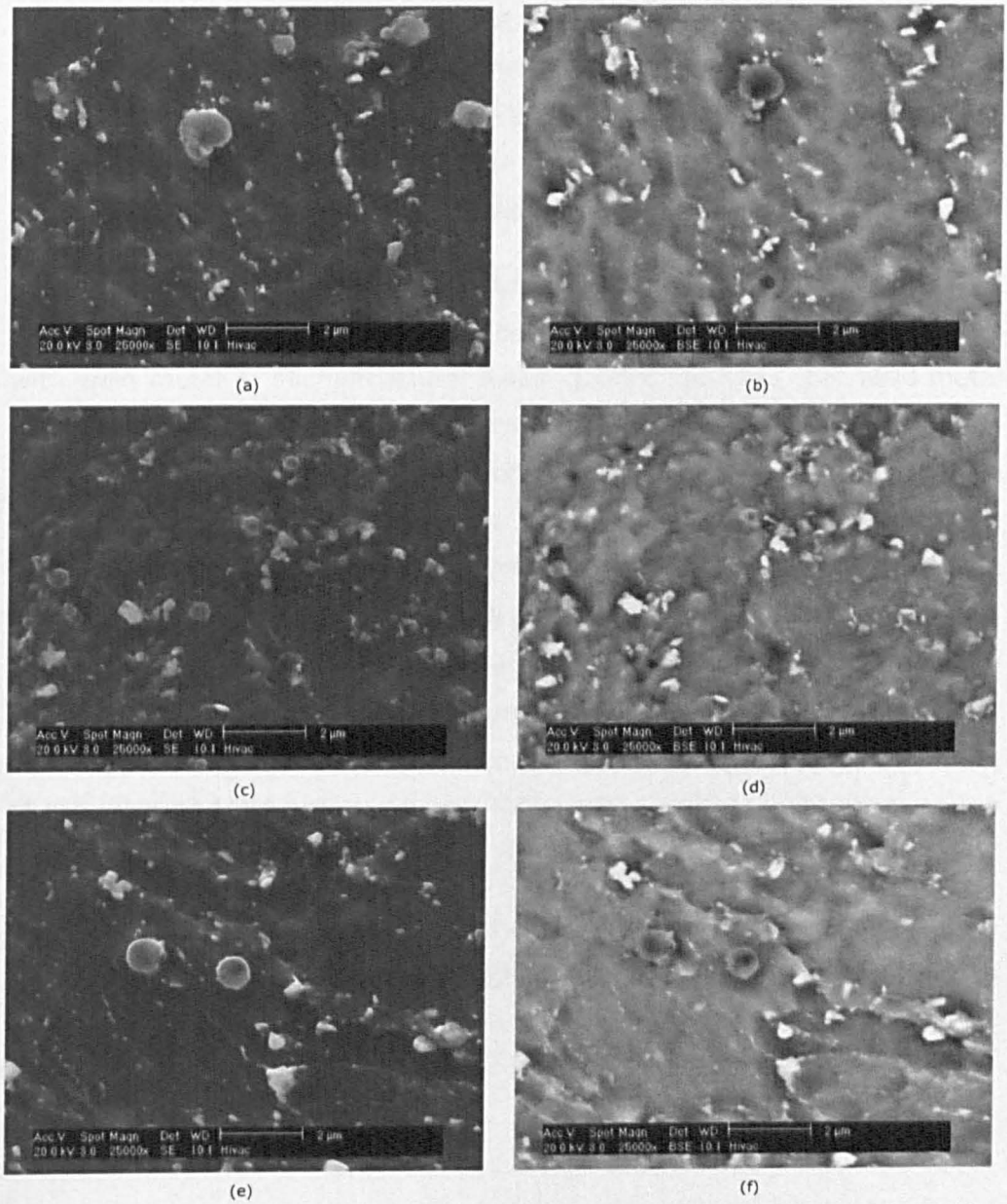

Figure 4.31 SE and BSE images of precipitation in the three weld metals A (a) and (b), B (c) and (d), C (e) and (f) after creep rupture at 625°C and 150MPa. Spherical precipitates with low contrast to the matrix in BSE images are $M_{23}C_6$, precipitates with a high contrast to the matrix in BSE images are Laves Phase, small precipitates with low contrast to the matrix in BSE images are MX.

Table 4.8 Approximate quantification of Laves phase in the three weld metals following creep testing at 625°C and 150MPa

Weld Metal	Number of Particles Measured	Approximate Mean diameter (nm)
A	1051	852
B	998	750
C	888	845

It should be noted for Table 4.8 that using SEM to quantify and measure precipitates of this size introduces uncertainty; the signals produced by the electron beam have a minimum resolution of approximately 1μm so anything smaller then this cannot be accurately measured. Therefore the mean diameter and number of particles measured are indications only.

Creep rupture tests showed that weld metal B had a low rupture strength compared to the other weld metals, despite close compositional similarities with weld metal A. Microstructural investigations revealed that weld metal B contained dense regions of precipitate-free zones near the fracture in all tests, with these precipitate-free zones exhibiting heavy creep damage (Figure 4.33). Figure 4.32 shows a precipitate free zone (PFZ) in the sample tested at 625°C and 150 MPa; creep damage is clearly visible within the PFZ and is highlighted well using back scattered electron images where damage shows up as black regions. For the specimen as a whole, cracks of the type observed in Figure 4.32 are localised to these PFZs, indicating a causal link between these two features. The initial examination of the weld pad did not reveal any PFZs, although the initial examination took only a small section of the weld pad.

Hardness tests were carried out on the PFZ and the bulk specimen in weld metal B following creep testing at 625°C and 150 MPa. Figure 4.34 shows that the PFZs are harder than the bulk of the creep specimen.

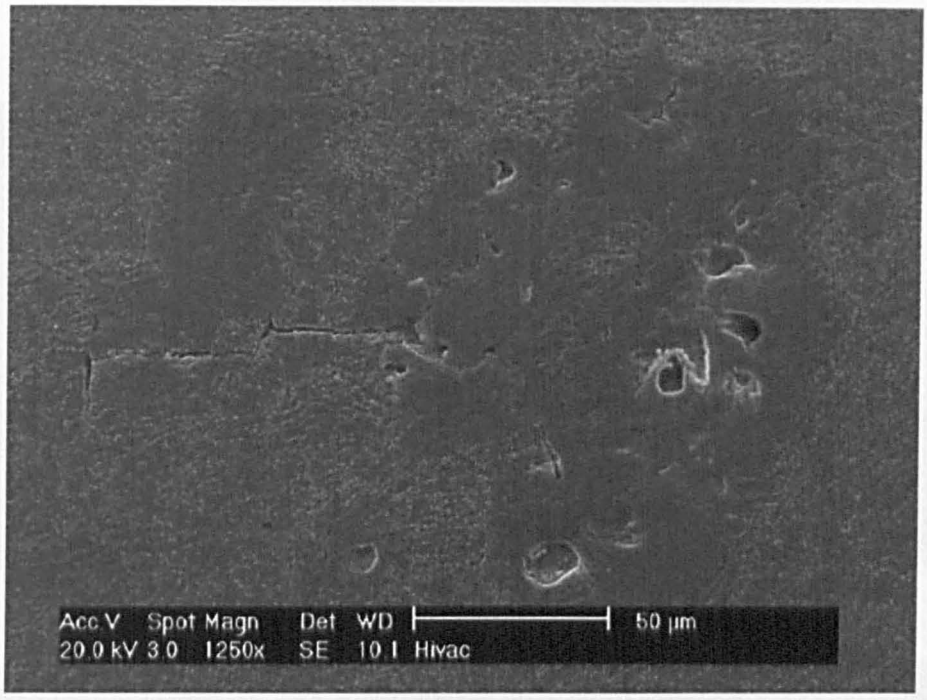

(a)

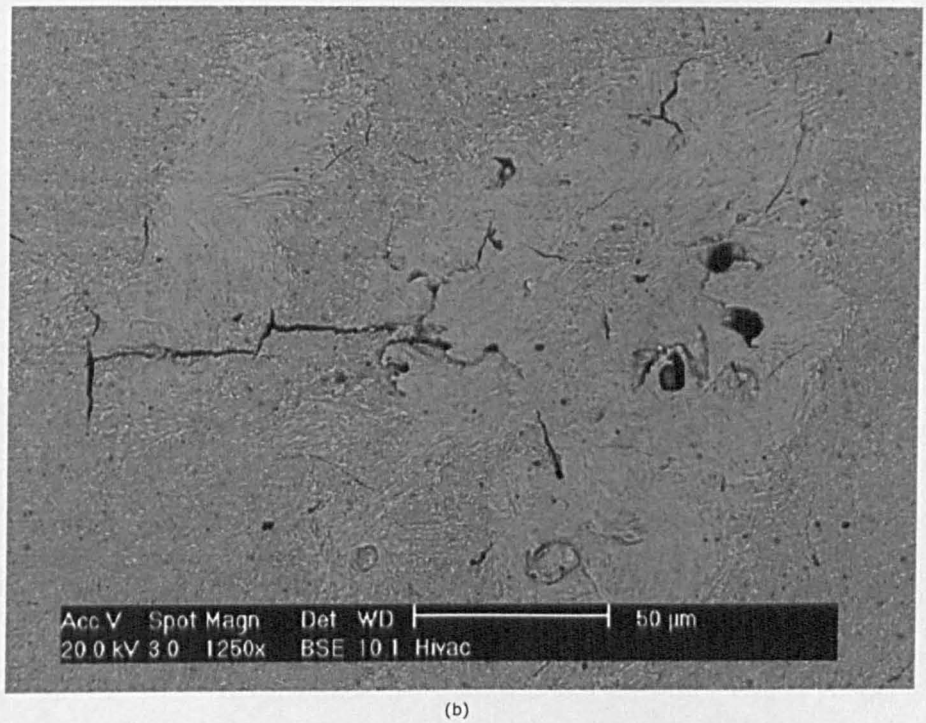

(b)

Figure 4.32 SE (a) and BSE (b) images of creep damage in weld metal B concentrated in precipitate free zones

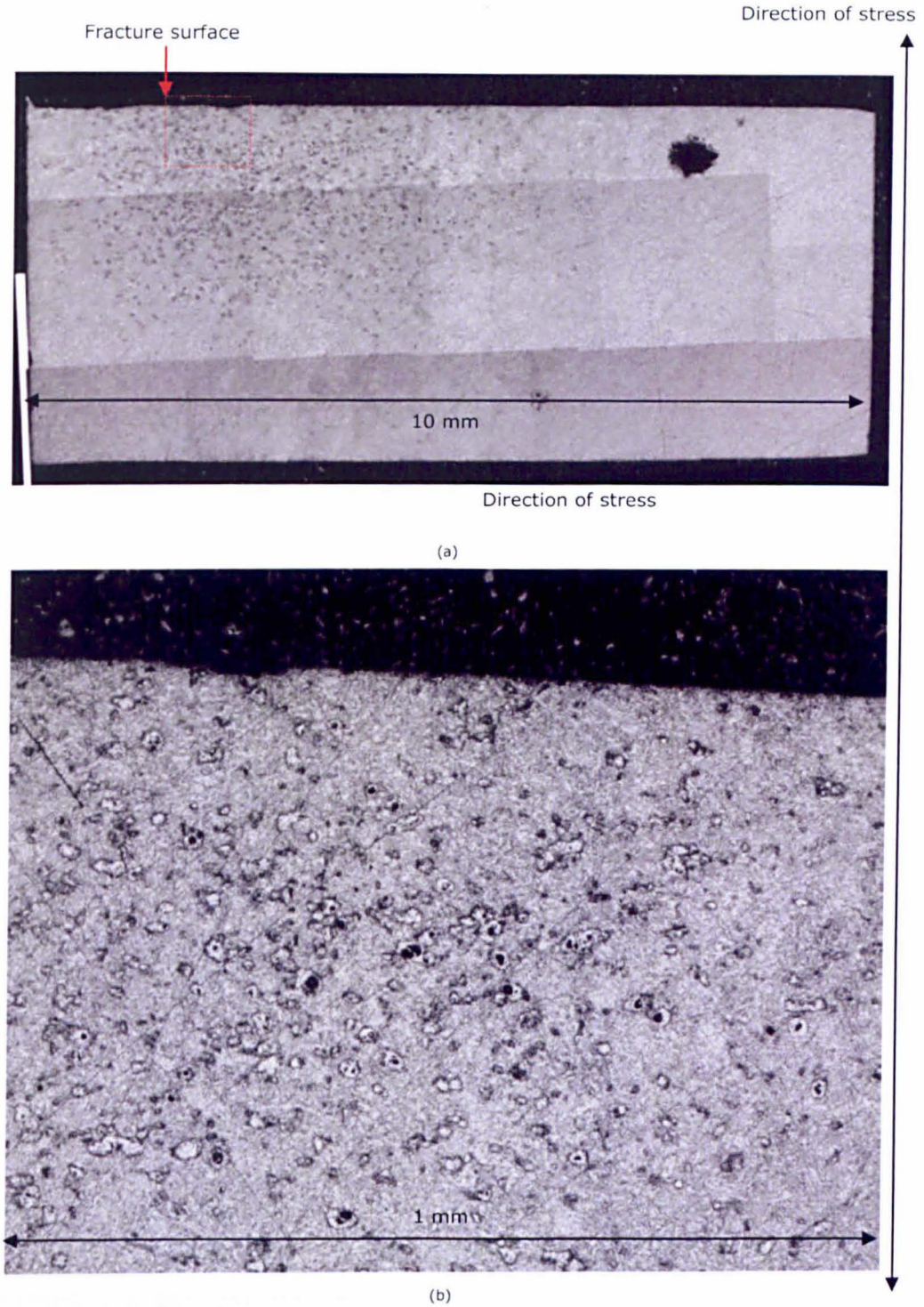

Figure 4.33 Optical images of precipitate free zone (PFZ) in weld metal B tested at 625°C and 150 MPa showing (a) PFZ concentrated near the fracture surface and (b) damage concentrated in PFZ near to the fracture surface as indicated in (a)

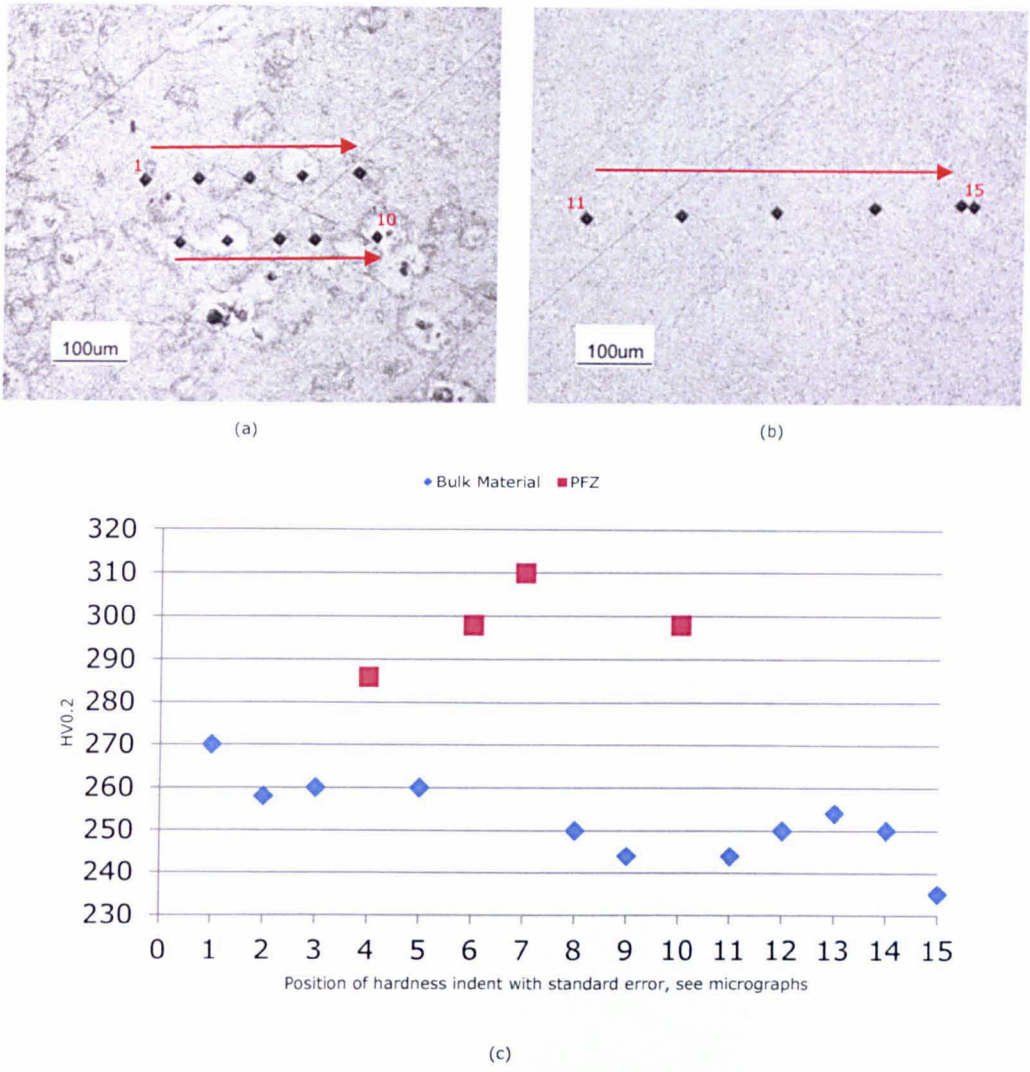

Figure 4.34 Hardness indents in (a) precipitate free zone (PFZ) and (b) the bulk specimen in weld metal B tested at 625°C and 150 MPa showing that (c) the PFZ are harder than the bulk of the creep specimen (only the first indent at point 15 is shown, the repeated indent is ignored)

Selected area EDX analysis was carried out on the PFZs and the surrounding bulk material at a number of locations (Figure 4.35, Table 4.9). The EDX analysis was carried out on 10 pairs of PFZ and bulk material regions and the average compositions taken in order to identify any patterns. Areas with minimal creep damage were chosen in order to minimise any possible effect of creep voiding on the results. Elements such as sulfur and phosphorus were excluded from the analysis due to their small wt% and the difficulty in accurate measurement of the compositions of these elements. It should be noted that elements such as tungsten are also difficult to measure in EDX due to the intensity of the peaks being low and overlapping with other elements therefore the mean compositions of the two regions are only indicators of the composition difference.

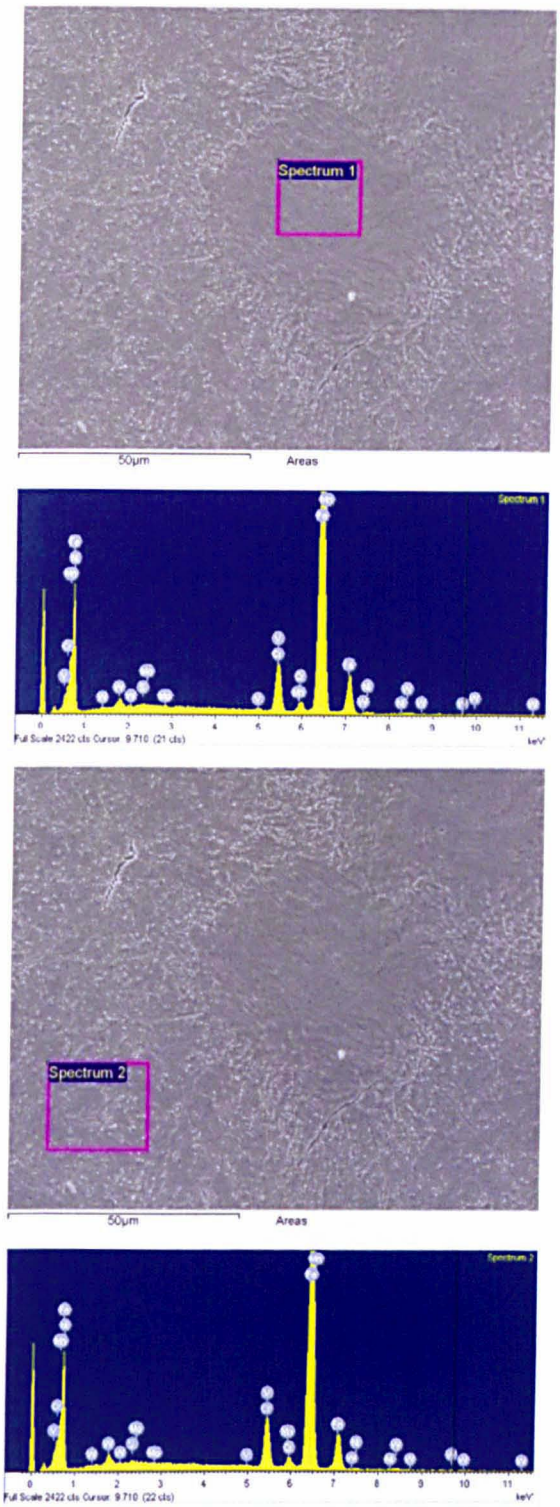

Spectrum	Si	V	Cr	Mn	Fe	Ni	Nb	Mo	W
Spectrum 1	0.27	0.33	8.52	1.12	86.27	0.58	0.34	0.73	1.95
Spectrum 2	0.59	0.07	9.06	1.03	86.22	0.69	0.11	0.59	1.61

Figure 4.35 Method used for EDX analysis of PFZ and surrounding bulk material in order to identify any compositional differences (elements are given in wt%)

Table 4.9 EDX analysis of PFZ and bulk pairs in weld metal B following creep testing at 625°C and 150 MPa

Bulk Spectrum	Si	V	Cr	Mn	Fe	Ni	Nb	Mo	W
1	0.37	0.20	8.92	1.03	86.64	0.49	0.06	0.55	1.75
2	0.36	0.22	8.79	0.97	86.54	0.47	0.06	0.57	2.13
3	0.38	0.18	8.67	1.00	86.63	0.52	0.08	0.65	1.89
4	0.41	0.16	9.00	1.03	86.40	0.47	0.10	0.56	1.87
5	0.28	0.20	8.92	0.91	86.45	0.38	0.05	0.58	2.24
6	0.34	0.16	8.91	1.08	86.38	0.36	0.05	0.42	2.38
7	0.29	0.27	9.00	0.98	86.44	0.49	0.04	0.54	1.95
8	0.44	0.17	8.81	1.02	86.63	0.36	0.03	0.56	2.06
9	0.35	0.18	9.03	1.10	86.41	0.39	0.04	0.57	2.02
10	0.33	0.24	8.85	1.07	86.27	0.40	0.04	0.55	2.26
Mean	**0.36**	**0.20**	**8.89**	**1.02**	**86.48**	**0.43**	**0.06**	**0.56**	**2.06**
Standard Deviation	**0.05**	**0.04**	**0.11**	**0.06**	**0.13**	**0.06**	**0.02**	**0.06**	**0.20**

PFZ Spectrum	Si	V	Cr	Mn	Fe	Ni	Nb	Mo	W
1	0.39	0.27	8.85	1.08	86.16	0.45	0.02	0.72	2.08
2	0.50	0.32	8.95	1.09	85.67	0.51	0.11	0.81	2.05
3	0.41	0.19	8.94	1.17	86.13	0.42	0.02	0.44	2.31
4	0.33	0.22	9.19	1.02	85.18	0.51	0.16	0.68	2.71
5	0.43	0.27	9.19	1.07	85.21	0.55	0.11	0.56	2.61
6	0.35	0.31	9.00	1.06	85.43	0.43	0.09	0.69	2.63
7	0.45	0.16	8.86	1.15	85.94	0.36	0.07	0.77	2.37
8	0.38	0.19	9.02	0.99	86.24	0.51	0.22	0.44	2.45
9	0.41	0.24	9.18	1.12	85.40	0.54	0.06	0.70	2.48
10	0.34	0.24	8.91	1.15	85.59	0.55	0.05	0.60	2.57
Mean	**0.40**	**0.24**	**9.01**	**1.09**	**85.70**	**0.48**	**0.09**	**0.64**	**2.43**
Standard Deviation	**0.05**	**0.05**	**0.13**	**0.06**	**0.40**	**0.06**	**0.06**	**0.13**	**0.23**

5 Discussion

5.1 Consumable Composition and Modelling

Figure 4.1 indicates that all three weld metals are predicted to go through the expected transformation process during the solidification stage of the welding process as follows; liquid/ δ-ferrite -> δ-ferrite /austenite -> austenite -> austenite/α-ferrite -> α-ferrite (this sequence excludes other phases such as carbides, nitrides etc). Table 4.2 indicates that the transformation temperatures for all three compositions are different, the reasons for which will be discussed later. Figure 4.2 shows the thermodynamic predictions of the precipitation behaviour and of particular interest is the region between 500°C and 700°C as the operating temperatures for P92 steels in power plants lie in this range. All three compositions are predicted to contain minor amounts (<0.1wt%) of the impurity phases M_3P and MnS. WMA and WMB have P92-similar compositions so are predicted to form the precipitates phases $M_{23}C_6$, MX and Laves phase that are found in the parent P92. WMC has a composition based on steel B2 rather than P92 although the major precipitate phases in this steel are similar to P92.

It should be noted that the compositions ahown in Table 4.1 have been determined from the weld pads. The composition of the weld consumable before use would have varied as during welding some elements will have oxidised, therefore the amount measured in the completed weld pad may be less then would be measured if the weld consumable was analysed.

All three contain the phase MX; however WMA and WMB are predicted to contain more MX than WMC, while WMB and WMC are predicted to contain two different types of MX. Both types are predicted to have an FCC crystal structure which is in accord with the literature (Sourmail 2001). The composition of the two types of MX was investigated using ThermoCalc and the results of this are presented in Figure 4.3. The MX in WMA is predicted to contain primarily vanadium with smaller amounts of niobium as the metal, and primarily nitrogen with small amounts of carbon as the non-metal. Figures 4.3 (a), (b) and (d) reveal that all three weld compositions are predicted to contain this form of MX and also indicate that it is also the most prevalent. The second form of MX predicted to be present in WMB and WMC is rich in niobium with small amounts of vanadium as shown in

Figure 4.3 (c) and (e). It is also only predicted to present in small amounts as shown in Figure 4.3. These predictions are in line with similar observations in the literature; Sourmail (Sourmail 2001) showed that MX can take a number of compositions where M = Nb and/or V, X = C and/or N, and can be referred to as carbides, nitrides and carbo-nitrides. Sourmail described three types of MX precipitates that can be found in P92. The first type is NbX that remains after austenitsation due to the niobium content being higher than the limits of the mutual solubility of niobium andcarbon and / or nitrogen in austenite at the austenisation treatment temperatures used for P92 (Ennis et al. 1998; Maruyama et al. 2001; Zielinska-Lipiec and Czyrska-Filemonowicz 2007). This is predicted as being present in WMB and WMC and can be linked to niobium levels in these two weld metals being higher than those in WMA (see Table 4.1). Sourmail also described secondary MX phases forming during tempering and these have been observed to take the form of NbX and VX, the majority of which are vanadium-rich (Zielinska-Lipiec and Czyrska-Filemonowicz 2007). Whilst all three weld metals are predicted to contain this form of MX (Figure 4.2), the amount present in WMC is lower. This can be explained by the lower amount of nitrogen in this composition, which is at approximately half the level present in the weld metals WMA and WMB. While Sourmail describes these MX precipitates as being either NbX or VX, the results of thermodynamic modelling shown in Figure 4.3 reveal compositions that are more complex, with either niobium or vanadium taking a dominant role in the two forms but never being totally alone.

A mention should be made of the third type of MX precipitate that Sourmail described, namely a V-wing complex. These occur when the large NbX precipitates that remain undissolved during austenitization act as nucleation sites for the VX that is produced during tempering, forming the V-wing complex. The presence of this type of MX cannot be predicted by ThermoCalc but it is possible that it could be present in both WMB and WMC as both of these are predicted to contain the residual NbX at the austenitising temperatures that could act as a nucleating site for a V-wing complex (Figure 4.3).

The level of niobium needed to induce the formation of NbX was also investigated using ThermoCalc, the result of which is shown in Figure 4.6. Here the niobium content was varied within the limits of the P92 specification (see Table 4.1) while the other elements were held at the

levels present in WMA. Figure 4.6 reveals that if the niobium levels were to rise above 0.067wt%, the formation of NbC could be expected. The other MX forming elements, namely carbon, nitrogen and vanadium are at similar levels in WMA and WMB, but the niobium level in WMA is 0.043wt%, ~ half of that in WMB (0.08wt%); this suggests that niobium levels are likely to control the formation of NbX.

Both forms of MX are desirable in the steel. The fine MX precipitates produced during tempering improve the creep strength of P92 by pinning dislocations (Abe et al. 2007; Klueh et al. 2005), while the coarse NbX particles that remain at austenisation are able to limit the growth of austenite grains and ensure that the recrystallisation of martensitic laths during tempering does not result in a loss of creep strength (Anderson et al. 2003). The action of NbX could be of particular importance to a multi-pass weld since this material undergoes numerous cycles of recrystallisation during the welding process itself, meaning that higher levels of niobium that encourage the formation of NbX could result in a weld that has higher creep strength. A note of caution must be added to this as Figure 4.6 also shows that the formation of NbX reduces the amount of VX; as such, a balance would need to be struck between pinning dislocations and reducing grain growth.

The primary carbide, $M_{23}C_6$, is predicted (see Figure 4.2) in all three compositions with an FCC crystal structure, although the amount present is predicted to vary; moreover, WMC is predicted to contain two forms of $M_{23}C_6$. The predicted compositions of $M_{23}C_6$ are shown in Figure 4.4. In WMA and WMB, the metal content is primarily chromium with some iron, tungsten, molybdenum and manganese. The literature states that $M_{23}C_6$ has a face-centre-cubic (FCC) structure (Sourmail 2001) and is typically $Cr_{23}C_6$ with iron, molybdenum and nickel being able to partially substitute for the chromium. However, ThermoCalc predicts that manganese rather than nickel will act as the primary substituting element. The composition of the $M_{23}C_6$ carbides is also predicted to vary with temperature, with the iron and tungsten levels increasing with temperature while the chromium and molybdenum levels are predicted to decrease. The compositions of $M_{23}C_6$ in WMC differ due to the lack of tungsten (which results in a higher molybdenum content) and the addition of boron. The literature states that together with the carbon, the boron gets incorporated in the growing $M_{23}C_6$ (which could now be referred to as $M_{23}(C,B)_6$) (Abe et al. 2004; Czyrska-

Filemonowicz et al. 2003; Golpayegani et al. 2003); in addition, ThermoCalc also predicts the presence of a small amount of $M_{23}(C,B)_6$ with the metal being comprised of chromium and iron. However, ThermoCalc also predicts that at temperatures above 610°C, the $M_{23}(C,B)_6$ will dissolve and the boron will form BN. The BN is an undesirable phase as it reduces the amount of MX present and removes boron from the $M_{23}C_6$, which thus limits its effect of reducing coarsening of this precipitate type (Czyrska-Filemonowicz et al. 2003; Golpayegani et al. 2003).

Laves phase is predicted to be present in all three weld compositions but only at lower temperatures in WMC. In contrast to $M_{23}C_6$ which remains relatively stable in the potential operating range of 600°C to 700°C, the amount of Laves phase predicted to be stable in WMA and WMB reduces rapidly with increasing temperature until fully dissolving at temperatures around 700°C. In WMC, the Laves phase is predicted to dissolve at much lower temperatures; however microstructural observations show it to be present at higher temperatures and this will be discussed in more detail in following sections. Despite this rapid reduction in the stable fraction of Laves phase with increasing temperature, the composition of the phase itself remains a stable mix of chromium, iron, molybdenum and tungsten as shown in Figure 4.5. The primary element in this Laves phase is tungsten, which is not present in WMC. The predicted form of Laves phase in WMC consists of molybdenum and iron. The effect of the Laves phase precipitation on long-term creep strength has been debated widely in the literature, since it is known that the precipitation of Laves phase promotes the depletion of molybdenum and tungsten from solid solution (Hosoi et al. 1986a; Hosoi et al. 1986b; Kunimitsu et al. 1991; Miyahara et al. 1995). As such, Laves phase has been generally considered detrimental for the creep strength of 9–12% Cr steels because of the associated reduction in solid solution strengthening. On the other hand, the presence of Laves phase can contribute to the increase of the creep strength by precipitation hardening under certain circumstances (Hald 1996). Recently, it has been generally agreed that fine Laves phase may contribute to the creep strength (Dimmler et al. 2003; Hald 1996; Hald and Korcakova 2003; Korcakova et al. 2001). As such, the lack of Laves phase predicted in WMC will favour solid solution strengthening, while in WMA and WMB, precipitation strengthening will be provided by Laves phase at the expense of solid solution strengthening.

Figure 4.2 (a) and (b) highlight a significant difference in the amount of $M_{23}C_6$ that is predicted to form in WMA and WMB, as well as a slight difference in the amount of Laves phase. ThermoCalc was used to investigate the effect of composition on the amount of precipitation of $M_{23}C_6$ and Laves phase, the results of which are shown in Figure 4.7. The individual elements were varied within the limits of the P92 specification while other elements remained at the levels present in WMA and the temperature was kept constant at 625°C. Increasing the level of carbon was shown to greatly increase the amount of $M_{23}C_6$ present while varying other elements has relatively little effect. From Figure 4.7 (a), the amount of $M_{23}C_6$ at a given carbon level can be observed and corresponds well to the phase property diagrams of Figure 4.2. This explains why WMB, with 0.09wt% C, has significantly less $M_{23}C_6$ then WMA which has 0.11wt% C. The amount of Laves phase present is affected by the levels of carbon, molybdenum, tungsten and silicon. That Laves phase precipitation would increase with increasing molybdenum and tungsten is not surprising as these are its major elements. Figure 4.7 (a) indicates that Laves phase decreases with increasing carbon content as the $M_{23}C_6$ fraction increases; this is because $M_{23}C_6$ contains chromium, iron, molybdenum and tungsten, all of which also make up Laves phase so that the former forms at the expense of the latter. The effect of silicon on Laves phase precipitation is interesting as silicon is predicted to remain in solid solution and does not directly precipitate, yet an increased level of silicon results in an increased amount of Laves phase. However, an increase in Laves phase due to increased silicon has also been observed in the literature and described as a kinetic effect, where higher levels of silicon have been shown to promote nucleation of Laves phase and additionally to reduce its coarsening rate (Hosoi et al. 1986b).

5.2 Weld Pad Microstructure

Characterisation of the experimental weld pads was carried out using OM, SEM and micro-hardness testing. Figure 4.8 shows OM images of the three welds in PWHT state, which all have the expected martensite microstructure and showed no weld defects such as porosity. No residual δ-ferrite was observed in the welds, although the complex martensite microstructure makes it difficult to identify other ferrite phases. Figure 4.9 gives a hardness profile over a length of 10 mm in each sample encompassing approximately three weld beads. The average hardness was 294.2 kgf mm^{-2} for WMA, 280.8 kgf mm^{-2} for WMB and 297.4 kgf mm^{-2} for WMC. The hardness profiles show variation over the 10 mm profile, particularly in WMB which had a maximum of 317 kgf mm^{-2} and minimum of 255 kgf mm^{-2}. Variations in hardness were expected, due to the complex multi-pass weld cycle, since the various HAZ features such as the FGHAZ and CGHAZ will have differing hardness (see Figure 2.26). Figure 4.10 shows SEM images that were taken in order to characterize the precipitates present in the weld metal. BSE imaging shows that the precipitates have a similar contrast to the matrix, especially the larger precipitates. EDX analysis revealed the larger precipitates to be chromium rich, indicating that these are $M_{23}C_6$. The other precipitates were too small to be analysed by EDX but, based on thermodynamic predictions and comparison with the literature, it can reasonably be concluded that these are MX particles. No Laves phase was observed in any of the weld pads, in contrast to the thermodynamic equilibrium predictions. This is due to the widely reported slow precipitation kinetics of Laves phase (Aghajani et al. 2009; Cui et al. 2010; Hald and Korcakova 2003); it is expected that the system will eventually reach equilibrium and the Laves phase will be present in this condition.

5.3 The Effect of Composition on A_1

It can be seen from Table 4.1 that the compositions of the weld consumables have some key differences that set them apart from the parent P92. The elements manganese and nickel are added in amounts that exceed that which is allowed for parent P92. Nickel and manganese are austenite stabilisers, lowering the ferrite to austenite transformation temperature Ac_1. The main reason for adding these elements is to ensure 100% austenite formation (without the danger of δ-ferrite formation) during initial cooling from the melt (and subsequent high-heat input during multi-pass welds) thereby increasing the stability of austenite at high temperature, and thus ensuring a 100% martensite structure when cooled (Knezevic et al. 2008). However, their levels must be restricted to ensure that during PWHT, there is no danger of reaustenitization. As can be seen from Figure 4.1 and Table 4.2, the thermodynamic modelling has enabled the prediction of the Ae_1 temperature and the δ-ferrite start temperature for all three weld consumables. If nickel and manganese are the most important austenite stabilizers and, as such, are the only ones usually considered (as suggested by Marshall (Marshall et al. 2002a)), then it would be reasonable to assume that the material with the highest combined content would have the highest δ-ferrite start temperature and the lowest Ae_1. The values in Table 4.1 give a (Ni+Mn) content of 1.42wt% for WMA, 1.41wt% for WMB and 1.29wt% for WMC. Based on this, it would be reasonable to expect WMA and WMB to have Ae_1 and δ-ferrite start temperatures which are very close to each other, with WMC having a higher Ae_1 temperature and a lower δ-ferrite start temperature. However, Table 4.2 shows that this is not the case as WMA has the lowest Ae_1 and highest δ-ferrite start temperature (respectively, significantly lower and higher than those of WMB) which means that its composition must confer the strongest austenite stabilization. The composition of WMC gives a δ-ferrite start temperature that lies between the others and an Ae_1 that is the highest. This indicates that the elements nickel and manganese should not be the only elements considered when designing the weld consumable composition. Other elements within the three weld compositions are clearly affecting both the ferrite and austenite stabilization to a significant degree. The results shown in Table 4.3 and Figure 4.12 show that there is also a difference between the measured Ac_1 and the calculated Ae_1 of typically 20-30°C which may be understood as follows. Firstly, Ac_1 is measured under continuous heating conditions, and Yang and Bhadeshia (Yang and

Bhadeshia 1989) have demonstrated that the higher the heating rate, the higher the measured Ac_1 value. To approach Ae_1 experimentally would require an infinitely slow heating rate. Secondly, Ae_1 is produced from a thermodynamic calculation that does not take into account reaction kinetics. The transformation from $\alpha \rightarrow \gamma$ is diffusional (Bhadeshia 1999), with austenite first forming at the prior-austenite grain boundaries, with fine austenite then precipitating in the grains as the reaction progresses (Shirane et al. 2009). The formation of austenite during the $\alpha \rightarrow \gamma$ transformation is controlled by the rate of carbon diffusion as the thermodynamic driving force for the formation of austenite increases with increasing available carbon (Cool and Bhadeshia 1997); however in P92 steels, most carbon is held in the form of $Cr_{23}C_6$ at the start of the $\alpha \rightarrow \gamma$ transformation which means that these precipitates must dissolve to release the carbon, leading to sluggish kinetics and thereby increasing the measured A_1 temperature.

Recently, Santella (Santella 2010) has used computational thermodynamics to predict the Ae_1 temperature in 9wt% Cr steels, and has presented the following equation for the prediction of Ae_1 in parent P92:

$$Ae_1(°C) = 778 - 80.6C - 150.7N - 55.1Mn - 68Ni + 22.9Si + 4.9Cr + 22.6Mo + 20.2Nb + 43.6V + 10.8W$$

Equation 5.1

The P92 composition range used by Santella was tailored towards the parent material which means that the range of composition of certain elements considered was narrower than that commonly observed in weld metals used for P92, whilst other elements commonly present in the welds (which are not present in bulk P92) were absent from the calculations. Indeed, the compositions of P92 weld consumables are often very different from that of the parent material, generally resulting in much lower A_1 temperatures than the parent; in some cases, there is concern that the A_1 temperature of these consumables may be low enough to result in undesirable reaustenitzation during heat treatment. According to Marshall (Marshall et al. 2002a), the tendency for undesirable reaustenitization of P92 weld metals during heat treatment may be understood by considering the sum of the nickel and manganese levels in the steel; specifically, he proposed that the minimum Ac_1 for P92 weld metal at 1.5wt%(Ni+Mn) is 790°C and thus suggested that 775°C is therefore a safe upper limit for

the PWHT temperature assuming that a margin of error of ± 15°C is required. As was argued in this thesis previously, this (Ni+Mn) rule is not deemed sufficient to describe the different Ae_1 temperatures that the three weld compositions exhibit.

Figure 4.16 indicates that the most significant elements (in terms of fractional variation in the allowed compositional range) in controlling the A_1 temperature of steels of this type (be they weld consumables or parent) are as identified by Marshall (Marshall et al. 2002a), namely nickel and manganese. However, other elements are observed to also have a significant effect, the largest of these being for molybdenum. Marshall's (Marshall et al. 2002a) proposed formula by which the potential for reaustenitization of these steels was described by the sum of the nickel and manganese contents implied that the effects of nickel and manganese on this reaustenitization potential were equal. This simplification is generally supported by Equation 4.1, where the influence of nickel and manganese are shown to be very similar (with the effect of nickel actually being 1.17 times that of manganese on a per wt% basis). To quantify the effect of such a difference, it can be shown that for a composition defined by the selected composition in Table 4.4 (but allowing nickel and manganese to vary but their sum to be 1.5 wt%), Equation 4.1 predicts an Ae_1 temperature of 773°C if the alloy contained 0 wt% Ni and 1.5wt%Mn whereas an Ae_1 temperature of 762°C is predicted if the alloy contained 1.5 wt% Ni and 0 wt% Mn; this difference of over 10°C indicates the value of the refined predictions of the Ae_1 temperature which would be provided by use of Equation 4.1 compared to use of Marshall's rule.

The recommendation that Mn + Ni < 1.5wt% (Marshall et al. 2002a) in 9-12wt% Cr steels has previously been used as a primary factor in weld consumable design for these steel types to ensure that the A_1 temperature is not reduced so far that it may begin to impinge upon the standard heat treatment temperatures for tempering of martensite. In addition, for weld metal design, other elements typically remain in the range specified by the parent alloy. However, Figure 4.12 shows that this recommendation does not sufficiently describe the effect that the alloy composition has on the A_1 temperature. Weld metals WMA and WMB both have similar (Ni + Mn) content, yet the predicted Ae_1 temperature and measured Ac_1 temperature show that WMA has a transformation temperature 10°C lower than WMB. Comparing the differences in composition with the aid of Figure 4.16 and

Equation 4.1 can help explain this difference. Weld metal WMB has silicon and niobium levels approximately twice those of weld metal WMA and Equation 4.1 shows that an increase in both of these elements increases the A_1 temperature. Figure 4.12 and Table 4.3 also indicate that while WMC has a much higher Ae_1 than WMA or WMB, their Ac_1 values are relatively close. Recent work indicates that this can be attributed to the reaction kinetics of the reaustenitization reaction since it has been argued that increases in the levels of manganese, silicon and chromium retard the kinetics of the $\alpha \rightarrow \gamma$ transformation (Miyamoto et al. 2010). Table 4.1 shows that weld metals WMA and WMB have a higher (Mn + Si) content (compared to weld metal WMC) and this is likely to slow the reaustenitization kinetics and thereby increase the measured Ac_1 temperature above the Ae_1 temperature more than that for weld metal WMC.

The P92 composition range used by Santella in the work on developing a formula for the Ae_1 temperature was tailored towards the parent material, thereby introducing key differences between their equation (reproduced in this thesis as Equation 5.1) and the equation derived as part of this current work (Equation 4.1). In Equation 4.1, the elements manganese, chromium, molybdenum and nickel have been given a greater range as these elements are found in greater concentrations in weld metals (Table 4.1). The austenite stabilisers cobalt and copper, present in the commercially available weld consumables in this study, were not included in Santella's study, but are included here. In addition, the elements boron, phosphorus and sulfur were ignored by Santella as their effect on the A_1 temperature was thought to be small. Table 5.1 shows the differences between the element coefficients in Equation 4.1 and Equation 5.1, and the effect that these differences would have on the change in the predicted A_1 temperature at both the minimum and maximum composition of that element in the weld metals (the values of maximum and minimum composition being taken from Table 4.4).

Table 5.1 Comparison of element coefficients in Equation 5.1 (Santella 2010) and Equation 4.1, showing the difference in Ae_1 that Santella's equation would produce at composition minimum and maximum

	V	Nb	S	P	B	W	Cu	C	N	Mo	Si	Ni	Co	Cr	Mn
Equation 5.1 coefficients °C/wt%	43.6	20.2	-	-	-	10.8	-	-80.6	-150.7	22.6	22.9	-68	-	4.9	-55.1
Equation 4.1 coefficients °C/wt%	53.8	31.4	85.6	35.8	20	10.6	-47.2	-99.5	-196.4	19.7	10.9	-78.8	-9.85	3.7	-67.4
Weld comp min (wt%)	0.15	0.04	0.001	0.001	0.001	1.50	0.001	0.07	0.02	0.30	0.001	0.001	0.001	8.50	0.30
Weld comp max (wt%)	0.25	0.09	0.01	0.02	0.007	2.00	0.04	0.13	0.07	1.50	0.50	0.70	1.10	10.00	1.00
Difference in Ae_1 @ comp min (°C)	-1.5	-0.4	-0.1	0.0	0.0	0.3	0.0	1.3	0.9	0.9	0.0	0.0	0.0	10.2	3.7
Difference in Ae_1 @ comp max (°C)	-2.6	-1.0	-0.9	-0.7	-0.1	0.4	1.9	2.5	3.2	4.4	6.0	7.6	10.8	12.0	12.3

A number of elements which were not included in Santella's work have been included in the current work such as boron, copper and cobalt. Of these, the effect of including these (even at the highest composition of the relevant element) is less than 1°C for the elements sulfur, phosphorus and boron, 1.9°C for copper and 10.8°C for cobalt, indicating the importance of cobalt in the calculation of Ae_1 temperature. In addition, the differences in the coefficients attached to the elements in the two equations results in some significant differences, with both manganese and chromium leading to differences of greater than 12°C at the highest composition of the relevant elements, with somewhat smaller differences for other elements. Moreover, whilst these differences are of course highest at the maximum composition of each element in the weld metal, the difference remains high even at the lowest composition of chromium. As such, although the differences in Ae_1 temperature predicted for the three weld metals considered is less than 12°C (Table 4.4), the potential for much greater differences cannot be ignored, and makes the use of Equation 4.1 more appropriate for design of such weld metals.

The investigation into the dependence of the Ae_1 temperature on composition using ThermoCalc has quantified the relative influence of the austenite and ferrite stabilisers and gives a clear indication that, within the specified composition range, large amounts of nickel and manganese will decrease the Ae_1 significantly as has been previously observed. However, the element coefficients in Equation 4.1 show that nickel actually contributes more to the lowering of Ae_1 on a per wt% basis, whilst Figure 4.16 indicates that the limits of the allowed compositional variations of these two elements in the P92 specification will confer a slightly larger range of Ae_1 temperatures associated with nickel variations. The element coefficients in Equation 4.1 highlight another factor that is not immediately obvious from Figure 4.16. Elements that are present in minor wt% ranges such as carbon, nitrogen, and sulfur have coefficients that are much greater than those of elements present in large wt% ranges. The wt% of these elements in the alloy is typically difficult to accurately control and these coefficients demonstrate that even a minor increase or decrease in the amount of these elements present in the alloys can alter the Ae_1 temperature significantly. The benefit of Equation 4.1 is that it will facilitate the balancing of elements to produce an Ae_1 at a desirable level. However, as demonstrated by Cool (Cool and Bhadeshia 1997), elements such as nickel and silicon do not just affect the transformation of $\alpha \rightarrow \gamma$ but

also affect the formation and retention of δ-ferrite which must be taken into consideration when designing weld consumables as the presence of δ-ferrite would be detrimental to mechanical properties.

5.4 PWHT Temperature Dependence

The investigation into the Ae_1 temperature of the weld metals has highlighted and quantified the importance of alloy composition on the transformation of $\alpha \rightarrow \gamma$, but it has also highlighted the difference between a calculated value of Ae_1 and measured value of Ac_1. The investigation into which is more applicable to PWHT focused on WMA as at this stage in the SUPERGEN project, it had been shown that this was the weld consumable that was expected to perform best under creep conditions. In order to assess the formation of austenite during the PWHT, a dilatometer was used as the literature had demonstrated that this was an effective means of observing the transformation via changes in volume (see section 2.4.5). The standard 2633:1987 (BSI 1987a) is currently used to determine the PWHT parameters and from this, the recommended heating rate of 100°C/hr was obtained. The cooling rate of 50°C/hr was also recommended in the specification, although this cooling rate is at the lower end of allowable cooling rates (BSI 1987a). This low cooling rate was chosen so as to investigate whether the decomposition of any austenite formed during the heat treatments would result in un-tempered martensite or soft ferrite. The selected hold temperatures of 760°C, 770°C, 780°C, 800°C and 820°C were chosen in order to investigate temperatures close to a standard PWHT of 760°C ± 15°C while also investigating temperatures that were within the observed transformation range during continuous heating (Figure 4.18). ThermoCalc was also used to calculate the equilibrium transformation of ferrite to austenite (Figure 4.17), presented in volume fraction terms so it can be directly compared to the results of dilatometry (Table 4.6).

Figure 4.16 shows the 760°C PWHT cycle and this closely follows the expansion experienced in the original continuous heating diagram. During the three hour hold, there is a dimension change that indicates ~ 1.5 vol% austenite has formed, which is in good agreement with the results of the equilibrium (ThermoCalc) predictions for this temperature (Table 4.6). During cooling, the variation of strain with temperature also closely followed the original continuous heating diagram. In Figure 4.17, the dilatation for the 770°C PWHT cycle is presented; in this case, there is a clearly visible contraction during the hold, indicating 8.3 vol% austenite, again in good agreement with the equilibrium (ThermoCalc) prediction (Table 4.6). The 780°C PWHT exhibits an even higher contraction during

the hold period, this occurring at a temperature well before the measured Ac_1 is reached, with 29.5 vol% transformation to austenite (Table 4.6). These three PWHT temperatures (760°C, 770°C and 780°C) lie between the calculated Ae_1 of 758°C and the measured Ac_1 of 792°C and all of them exhibit transformation to austenite during extended hold.

The 800°C and 820°C heat treatment cycles both exhibit significant transformation of 61.3 vol% and 84.4 vol% respectively (Table 4.6). The significant amount of transformation also allows the decomposition of the austenite to be observed, especially so in the case of the 820°C heat treatment cycle which has been reproduced below in Figure 5.1 with annotations on the phases expected to be present at each stage.

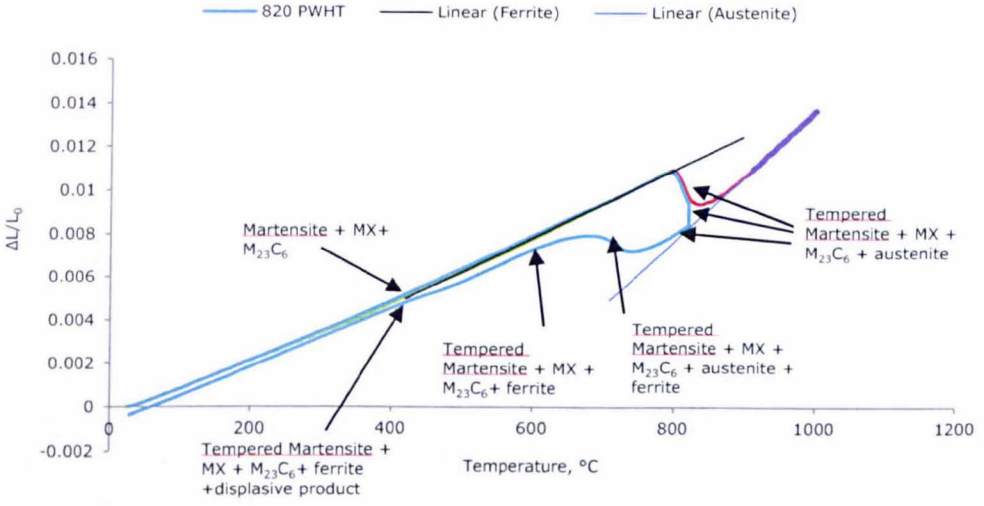

Figure 5.1 The phase transitions in WMA during the thermal cycle of a simulated 820°C PWHT with a heating rate of 100°C/hour and a cooling rate of 50°C/hour

The initial microstructure of the material in all samples is as described in section 4.5.2, namely a martensite matrix with precipitates of $M_{23}C_6$ and MX. During the hold, the transformation to austenite has been demonstrated but at the end of the hold, as the material never completely transforms to austenite, in all cases the microstructure will be a mix of austenite, heavily tempered martensite and the precipitates. As the material cools, a large expansion is observed corresponding to the transformation of austenite to ferrite, leaving a mixture of tempered martensite, ferrite and the precipitates. Around 400°C there is a further small dimension change, corresponding to the marteniste transformation temperature (M_s) for P92 steels (Richardot et al. 2000a), although the volume change is small. This leaves the resulting microstructure following a PWHT where there has been transformation to austenite consisting of a

mixture of tempered martensite, un-tempered martensite, ferrite and precipitates. This microstructure is undesirable as the ferrite has weaker creep properties compared to the tempered martensite, whilst the untempered marteniste will be initially brittle, but will temper to some degree in service (remembering that service temperatures are much lower than the standard PWHT temperatures). Faster cooling rates will result in a greater proportion of the austenite transforming to un-tempered martensite.

As has been previously highlighted, there is a difference between the measured Ac_1 and the calculated Ae_1. Table 4.3 and Figure 4.12 highlight these differences. As the parent P92 steel used in the investigation had already undergone a full normailizing and tempering heat treatment before the Ac_1 shown in Table 4.3 was measured, it was therefore prudent to investigate what effect the material starting condition would have on the measured Ac_1 and this was conducted on both the parent P92 and WMA. Figure 4.13 shows the results for the parent P92, demonstrating a 4°C drop in the measured Ac_1 from 830°C to 826°C after repeating the thermal cycle. In comparison, Figure 4.14 shows the effect on the weld metal WMA, where no difference in the measured Ac_1 was observed. This can be explained as follows. The parent P92 has previously undergone normalising and tempering heat treatments; normalising creates a microstructure of untempered martensite and when this is tempered, precipitation of the carbides $M_{23}C_6$ and MX occurs. This is the microstructure at the start of the first thermal cycle, giving an Ac_1 value of 830°C (measured using a heating rate of 100°C/hr). This first thermal cycle is essentially a normalising treatment which dissolves all the carbides and results (on cooling) in a microstructure of untempered martensite. In this structure, the carbon is in solution rather than having been bound up in precipitates. In the second thermal cycle, this free carbon increases the driving force for the ferrite to austenite transformation, thereby reducing the measured Ac_1 value.

The situation is different for the weld metal (WMA). When the weld metal is deposited, it is molten, cooling rapidly and solidifying to form a microstructure that ends up as untempered martensite with an inhomogeneous distribution of elements. As this is a multipass weld (in these samples approximately 3 weld beads per sample), the weld will undergo multiple additional thermal cycles. This results in a mixed microstructure consisting of fine grain and coarse grain martensite with

little precipitation. In the first thermal cycle, the weld metal is heated and the Ac_1 temperature measured. It was then held at high temperature and normalised, and then cooled, resulting in a microstructure with little precipitation. As such, the microstructure following one thermal cycle was very similar to that before the thermal cycle. As such, in the second thermal cycle, and the measured Ac_1 temperature was the same as in the first thermal cycle.

Further investigations were conducted into the effect of heating rate on the measured Ac_1 value. Samples of both parent P92 and WMA were continuously heated at rates of 20°C/hr, 50°C/hr and 100°C/hr and their Ac_1 values measured. The results of this experiment are shown in Figure 4.15, showing that for both the parent material and the weld metal, as the heating rate decreases below the industry standard of 100°C/hr so does the measured value of Ac_1 which approaches the calculated value of Ae_1.The question remains as to why the difference between the calculated Ae_1 value and measured Ac_1 is greater in the weld metal than the parent metal. As both materials exhibit a decrease in measured Ac_1 towards Ae_1 with decreasing heating rate, this difference must be due to kinetics of transformation. Miyamoto (Miyamoto et al. 2010) investigated the effects of manganese, silicon and chromium additions to a iron-carbon alloy on the reverse transformation to austenite. They first calculated the transformation values using ThermoCalc (with database TCFE5) and then measured the transformation temperatures with increasing alloying additions. They found that increasing additions of the elements retarded the transformation kinetics in the same way as observed in this work. A comparison of the compositions of the parent metal and WMA (Table 4.1) shows that managase is the element (of those studied by Miyatomo) with the most significant difference (0.45wt% in the parent, 0.78wt% in WMA). Oi (Oi et al. 2000) conducted a similar study that looked at both manganese and nickel additions to an iron-carbon steel. They found that the effect of nickel was similar to the effect of manganese. Comparing the nickel content of the parent metal and WMA reveals that this is another element with significant difference (0.27wt% in the parent, 0.64% in WMA). It is therefore proposed that it is the high concentrations of these elements in WMA which is responsible for the greater difference between the calculated Ae_1 and measured Ac_1. The experiments conducted in this work (both on the effect of heating rate, Figure 4.15, and the temperature of PWHT, Figure 4.19 – 4.23) demonstrate that the calculated Ae_1

temperature is more relevant to design of PWHT schedules than the Ac_1 value obtained via continuous heating.

Figure 4.25 shows the rate of austenite formation during the PWHT. At 760°C, the rate of transformation is slow with measurable transformation occurring after a hold time of 2 hours. At 770°C there is a faster rate of transformation, with measurable amounts of austenite formation from the start of the PWHT. The same is true of 780°C which again shows an increase in the rate of austenite formation. For 800°C and 820°C there is already a significant amount of austenite present by the time the hold temperature is reached, while the rate of austenite formation is initially rapid before stabilizing. The PWHT at 800°C shows that the rate of austenite formation at this temperature falls to zero after about an hour; in contrast, in the PWHT at 820°C, austenite continues to form throughout the hold. This difference is likely to be due to the $M_{23}C_6$ not dissolving at a significant rate at the lower of these two temperatures (see Figure 4.2) which means that the carbon required to force the transformation is still locked up in the precipitates. At the higher temperature of 820°C, the $M_{23}C_6$ will be dissolving rapidly and releasing the carbon into solution to drive the formation of austenite (Cool and Bhadeshia 1997). The reason for the ever increasing initial rate of austenite formation with increasing PWHT temperature is that both the diffusion rates and the driving force for the transformation are increasing with temperature, resulting in the continuous increase in the rate of transformation (Figure 5.2).

The average hardness of the samples (seen in Figure 4.26) shows a softening of the microstructure following the PWHT. Some softening is expected as the martensite tempers, but after PWHT at 800°C and 820°C, the microstructures are particularly soft due to the presence of large amounts of soft ferrite. There is also large scatter in the hardness values of the lower PWHT temperatures which is generally expected in multi-pass welds due to the differences in thermal profile that have been experienced during the welding process. In the low temperature PWHTs (760°C, 770°C), little re-transformation will have taken place, and so the varied hardness profile remains. However, during higher temperature PWHTs, significant transformation to austenite will have taken place; as such, it is likely that some variation in hardness will be due to differences between the soft ferrite or hard un-tempered martensite (the products of austenite transformation on cooling) and the original martensite that is tempered

during the PWHT. Figure 4.27 shows optical images of the five PWHT samples where it can be seen that it is difficult to identify the different forms of ferrite that may be present in the microstructure. To this end, EBSD was used due to its ability to determine crystal orientation and grain boundaries. It can be seen from the EBSD images presented in Figure 4.28 that there is an identifiable difference in the microstructures of the samples heat treated with the different hold temperatures. For the sample PWHT at 760°C, there is a clear martensite structure and the same can be said of the sample PWHT at 770°C, although the structure at 770°C appears to be finer (this is most likely due to the fact that the region imaged was an area of FGHAZ, rather than being an effect of the increased PWHT temperature). At 780°C and 820°C, there has been a clear change in the microstructure, with equiaxed grains mixed with areas of martensite. These equiaxed grains are likely to be the areas of soft ferrite, although their growth has been limited due to the high levels of precipitates present at all the PWHT temperatures (see Figure 4.8).

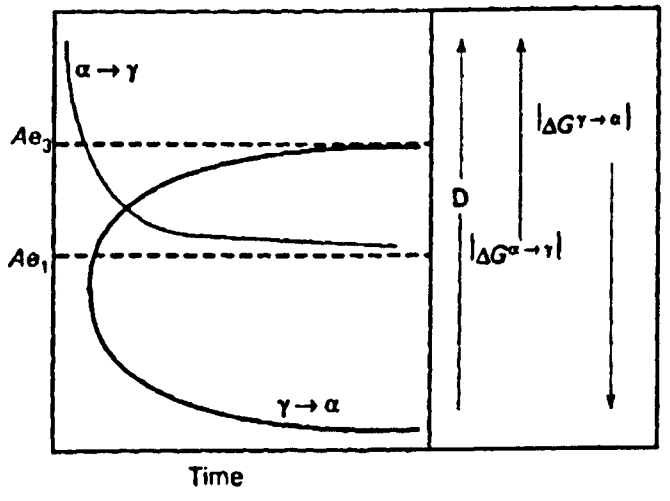

Figure 5.2 The TTT curves for the γ→α transformation and the reverse α→γ transformation (Bhadeshia and Honeycombe 2006)

5.5 Weld Metal Creep Testing

The earlier failure and low failure strain of WMB under creep has been shown to be due to the presence of precipitate free zones which are associated with the development of cracks during creep as shown in Figure 4.32. These zones experienced heavy creep damage as the precipitation strengthening important to the creep strength of P92 steels was absent. It is proposed that the PFZ has formed as the result of retained δ-ferrite in the weld. The retention of δ-ferrite in weld metal for these types of steels has been observed before (Cai et al. 1997; Falat et al.). They tend not to be observed in initial examinations of the weld pads as δ-ferrite occurs in either regions where the complex thermal cycle of multi-pass welding has created the right conditions (a peak temperature above the δ-ferrite start temperature, Table 4.2), or where weld solidification has created a localised region high in ferrite stabilizers which lowers the δ-ferrite to austenite transformation temperature. As these regions will be very localised, they can easily be missed in initial examinations of a large weld, only becoming apparent during creep testing as they are creep weak (Oñoro 2006). In Oñoro's study (Onoro 2006), the morphology of the retained δ-ferrite was found to vary depending upon the location within the weld pad, with δ-ferrite in the centre of the multi-pass weld having an elongated spherical morphology and δ -ferrite near the fusion boundary having a jagged and blocky morphology. All samples in the current study were machined from the centre of the weld pad, where the δ-ferrite morphology is expected to consist of isolated islands due to additional heat treatments produced by further weld passes. This morphology is undesirable because it has been shown to significantly reduce creep and toughness properties of the weld metal due to the δ-ferrite remaining precipitate free (Cai et al. 1997). The retained δ-ferrite remains precipitate-free since, when the high temperature δ-ferrite first forms, it contains little carbon due to the low solubility of carbon in ferrite (the carbon will have partitioned to the austenite in which it has high solubility). The rapid cooling experienced by the weld traps carbon in the newly formed martensite, from where it is consumed in the rapid precipitation of the $M_{23}C_6$ and MX precipitates. The reason why δ-ferrite, and the resulting PFZ, has formed only in WMB is due to compositional differences in the weld consumable. The first of these compositional differences to note is the

(Mn + Ni) content. For weld consumables designed for the steel P91, it has been proposed that (Mn + Ni) < 1.5wt% in order to keep the Ac_1 temperature in the range suitable for PWHT while still suppressing the formation of δ-ferrite (Marshall et al. 2002b). As previously stated, in the design of weld consumables for use with P92, this rule has been followed in the design of this consumable. Based on these values, it would be expected that WMA and WMB would have similar δ-ferrite formation temperatures while WMC would have a lower one. Table 4.2 shows that this is not the case as it is WMB that has the lowest δ-ferrite formation temperature. This is because other elements also play a role in the formation of δ-ferrite. High chromium or high silicon levels promote the formation of δ-ferrite during austenitization at around 1100°C (Bhadeshia and Honeycombe 2006). Through experimental investigation of chromium and nickel equivalents, Oñoro determined that in a 9Cr steel containing tungsten and molybdenum, the silicon and vanadium content should each be below 0.25wt%, while niobium should be below 0.006wt%, in order to avoid the formation of δ-ferrite during welding (Oñoro 2006). It can be seen from Table 4.1 that WMB has twice the amount of the ferrite stabilizers silicon and niobium compared to WMA, which has resulted in the formation of δ-ferrite during welding. The small size of the Laves phase in WMB, as shown in Table 4.7, is probably due to the higher levels of silicon which have been shown to act as nucleation sites for Laves phase and reduce their coarsening rate (Hosoi et al. 1986b). In addition to this, EDX analysis of the PFZ and surrounding bulk material (Figure 4.35 and Table 4.9) has revealed compositional differences. The PFZ has a higher amount of ferrite stabilizers, in particular tungsten. This has led to δ-ferrite being stable at lower temperatures in these regions. It is worth noting that there is difficulty in measuring the levels of elements like tungsten due to the peak positions in the EDX spectrum (Figure 4.35), which have low intensity and overlap with those of other elements. However, the general trend for higher tungsten levels in the PFZ can be identified. It is likely that this localised high-tungsten content has come about due to inhomogeneities in the welding consumable. The weld consumables are modified 9CrMo basic coated low hydrogen electrodes for high temperature creep applications, which consist of a mild steel core rod coated by a flux containing the necessary alloying elements. Discussions with industry have indicated that elements can become segregated in the flux of the weld consumable, particularly dense materials such as tungsten. When the welding is

conducted, certain areas will have higher levels of tungsten introduced due to the inhomogeneous nature of the weld consumable. It is likely that this was the source of the tungsten imbalance and the cause of the PFZ which lead to an early creep failure.

The high failure strain exhibited by WMC can also be attributed to compositional differences. While it has the same precipitate phases as WMA and WMB, the absence of the solid solution strengthening effect of tungsten has resulted in a higher ductility and therefore a higher failure strain. The addition of cobalt has not provided the same level of strengthening, and the formation of Laves phase has removed molybdenum from the matrix and thereby also reduced its solid solution strengthening effect. Klueh (Klueh 2005) stated that at equilibrium, the Mo_{eq} (where Mo_{eq} = Mo + 0.5W [wt%]) should not exceed 1%. If the steel has a Mo_{eq} greater than 1 wt% when operating in the 600-650°C range, the tendency for the intermetallic Laves-phase to form is increased, resulting in the removal of molybdenum from solid solution and a reduction in solid solution strengthening (Klueh 2005). The Mo_{eq} of WMC is well above this value at 1.41wt%. The high ductility exhibited by WMC can also be attributed to compositional differences, since this material was based on steel B2 rather than P92. This weld metal was expected to perform well since the alloy on which it is based is judged to be significantly stronger than P92 (Gianfrancesco et al. 2009). The current work and that published by others (e.g. (Allen et al. 2007b)) suggests that the compositional factors which make a parent material creep-strong do not necessarily carry across on a one-to-one basis to weld metals.

At this point it is important to refer back to section 4.1 and in particular Figure 4.2 which showed the equilibrium phase fraction diagrams. After being held at high temperature during the creep tests for long periods of time, it is expected that equilibrium conditions will have been neared if not reached. This means that precipitation of the Laves phase, (previously described as having sluggish precipitation kinetics resulting in it not being observed in the weld pads) should be complete. Indeed, Laves phase is present in all three of the welds following the creep tests. However, ThermoCalc predicted that there would be no Laves phase present in WMC at these temperatures (see Figure 4.2c), but Figure 4.31 and Table 4.8 clearly demonstrate that it is present with EDX analysis also revealing that it is molybdenum-rich. The Laves phase predicted by ThermoCalc is also

molybdenum-rich (see Figure 4.5c) but was not predicted to be stable at the temperature the creep test was conducted at. To understand the differences between the microstructural observations and the ThermoCalc predictions regarding the presence of Laves phase at these temperatures for WMC requires an examination of the mechanisms of Laves phase formation. There are two mechanisms for the nucleation and growth for Laves phase, one of which is that Laves phase precipitates alone on martensite lath boundaries, with the precipitate being coherent with one grain but growing into an adjacent grain with which it has no rational orientation relationship. The other mechanism is that Laves phase precipitates are formed in the regions adjacent to $M_{23}C_6$ particles, and they then grow at the expense of the chromium-rich $M_{23}C_6$ carbides in close vicinity. It has been established that the former mechanism is the dominant formation mechanism for Laves phase as it has been argued that Laves phase precipitates prefer to locate on the prior austenite grain boundaries and the martensite lath boundaries (Cui et al. 2010). ThermoCalc predictions are based upon the principle of thermodynamic equilibrium, but these weld metals have a martensitic matrix, which is produced via a displasive process and cannot be predicted through thermodynamic equilibrium calculations. Laves phase is present as the martensite matrix in WMC provides numerous nucleation sites.

Overall, WMA was found to have the highest creep strength for the conditions tested and is therefore most likely to be able to enable power generation plant-realistic weld HAZ failures in *cross-weld specimens* within reasonable test time.

The consumable that differed the most in terms of performance was WMB. This material had significantly lower creep ductility and the highest minimum creep strain rates.

6 Conclusions

The purpose of this thesis was to understand the behaviour of welds in P92 steel so that their in-service behaviour may be better understood. This understanding has been achieved through a combination of thermodynamic modelling, mechanical testing and microstructural characterization.

It has been industry's experience that different heats of P92 material, all within the P92 specification, can have very different mechanical behaviour Thermodynamic modelling has enabled a better understanding of how the composition affects the equilibrium phases of P92 and the knowledge learnt here is applicable to both parent and weld material. Precipitation strengthening is important to the creep resistance of P92 and the modelling has revealed how precipitate levels vary based on composition. The key findings are summarized below;

- High levels of carbon increase the amount of $M_{23}C_6$ precipitated while other *elements have* little effect (Figure 4.7). The P92 specification gives limits of 0.07-0.13 wt%C *so there can be* significant variation between P92 heats, e.g. from the weld metals studied here, weld metal A (0.11wt%C) has 25% more $M_{23}C_6$ then weld metal B (0.09wt%C).
- The amount of Laves phase is decreased with increasing carbon, but is increased with tungsten, molybdenum and silicon.
- The stability of Laves phase rapidly decreases over the temperature range of typically 600°C-700°C which has implications for the validity of accelerated creep testing used to determine the long term creep strength of P92 at its operating temperature which is typically 500°C-620°C.
- High levels of niobium will result in the formation of two different kinds of MX precipitate, observed in the literature to have different morphologies.
- The addition of boron results in two different forms of $M_{23}C_6$. The literature indicates that boron improves creep resistance as it reduces the coarsening rate of $M_{23}C_6$.

Using this knowledge, quality checks on P92 used by industry can better ensure a materials fitness for service if an accurate composition is known

and manufacturers can further tailor compositions to produce the strongest possible material.

Some of the biggest problems that industry have had when using P92 (and its predecessor P91) have been caused by incorrect heat treatments that result in a non-martensitic material entering service (that fails early in service life), or the cracking of material due to the presence of untempered martensite (resulting in delays to construction, additional cost and unfit material entering service). A combination of thermodynamic modelling and mechanical testing was used to investigate the key transformation of ferrite to austenite. This investigation focused on the effect of composition on the transformation temperature, A_1, and the rate at which austenite could form during PWHT. The key findings are summarized as follows;

- The A_1 value produced by thermodynamic modelling (Ae_1) is typically 30°C lower than the value arrived at via thermo-mechanical testing (Ac_1, which is currently the industry standard for determining maximum PWHT temperatures).
- A typical heating rate used by steel manufacturers to measure the Ac_1 temperature is 100°C / hr. Experiments conducted in this work have shown that as the heating rate decreases, the measured Ac_1 value approaches the calculated Ae_1.
- Compositional modelling has revealed the degree to which individual element variation can affect the A_1 temperature. It is demonstrated that the rule which defines that (Ni + Mn) ≤ 1.5wt% is insufficient when designing weld consumables that are to be PWHT at the industry standard of 760°C ± 15°C.
- An equation has been developed that predicts the Ae_1 temperature for any weld consumable for use with P92 using compositional data;

$$Ae_1(°C) = 809.7 - 99.5C - 196.4N - 67.4Mn - 78.8Ni - 9.85Co - 47.2Cu + 20B + 10.9Si + 35.8P + 95.6S + 3.7Cr + 19.7Mo + 31.4Nb + 53.8V + 10.6W$$

- Using thermo-mechanical testing, the transformation of ferrite to austenite has been investigated for a material with an Ae_1 = 758°C and an Ac_1 = 792°C. It has been demonstrated that, for a range of PWHT temperatures between Ae_1 and Ac_1, significant transformation to austenite takes place.

- Microstructural characterisation reveals that a slow cooling rate will result in retained austenite forming soft ferrite while a fast cooling rate results in the formation of hard untempered martensite.
- Based on the results of experiments conducted as part of this work, it is suggested that calculations of Ae_1 would be a more effective way of determining key transformations for the development of industry standards for high-alloy steels such as P92.

Using this knowledge, better heat treatments can be devised. The knowledge of how composition affects the A_1 temperature is useful for both welds and parent material, enabling the design and selection of P92 material that will not transform during heat treatment. The equation for Ae_1 allows the determination of maximum safe heat treatment temperatures, and should be used in preference to currently measured Ac_1 values; this change will reduce the likelihood of poor quality material entering service. The mechanical testing has demonstrated that during PWHT (or parent material tempering), equilibrium conditions are approached, confirming that Ae_1 should be used to determine maximum heat treatment temperatures instead of Ac_1.

Creep testing of three different weld consumables was carried out to find out which had the best properties for use in service and the key findings are summarized as follows;

- Creep testing of weld metal has indentified that δ-ferrite causes early failure, as the resulting PFZs are creep weak.
- Localized δ-ferrite is caused by inhomogeneous distribution of ferrite stabilizers such as tungsten, resulting in greater stability of δ-ferrite and its retention in the weld.
- The source of this tungsten imbalance is discussed and attributed to a weld consumable with poor tungsten distribution.
- Thermodynamic modelling has been used to calculate the temperature at which δ-ferrite forms for a number of compositions.
- Due to the localized nature of the δ-ferrite, it is difficult to locate in initial microstructural examinations, only becoming apparent upon failure as it is creep weak. Identification of significant retained δ-ferrite in a P92 weld entering service is almost impossible as destructive examination is not permitted.

- The absence of tungsten in the weld metal composition (WMC) results in a material with greater ductility, but lower creep strength. It has been noted in the literature that P92 can have low creep ductility and this indicates that tungsten may have a role in that.
- It has been reported in the literature that silicon acts as a nucleation site for Laves phase and can reduce coarsening. It is observed that the weld metal with the highest silicon content (0.42wt%, WMB) has the smallest average diameter Laves phase, but the same volume fraction of Laves phase as a weld metal with less silicon (0.2wt%, WMA).

Using this knowledge, quality checks of weld consumables can be initiated to ensure a homogeneous distribution of elements so that localized weaknesses in a weld can be avoided. There is tentative evidence that tungsten plays an important role in the creep ductility of P92 and that variations in tungsten and silicon could lead to an optimization of creep strength.

The outcomes of this thesis are very relevant to the power generation industry and will enable the more successful application of P92 steel and welds.

7 References

Abe, F. 2004. "Coarsening behavior of lath and its effect on creep rates in tempered martensitic 9Cr-W steels." Materials Science and Engineering A 387-389:565-569.

Abe, F., T. Horiuchi, M. Taneike and K. Sawada. 2004. "Stabilization of martensitic microstructure in advanced 9Cr steel during creep at high temperature." Materials Science and Engineering A 378(1-2):299-303.

Abe, F., M. Taneike and K. Sawada. 2007. "Alloy design of creep resistant 9Cr steel using a dispersion of nano-sized carbonitrides." International Journal of Pressure Vessels and Piping 84(1-2):3-12.

Abe, Fujio. 2008. Creep-resistant steels. Cambridge: Woodhead Publishing Limited.

Aghajani, A., F. Richter, C. Somsen, S. G. Fries, I. Steinbach and G. Eggeler. 2009. "On the formation and growth of Mo-rich Laves phase particles during long-term creep of a 12% chromium tempered martensite ferritic steel." Scripta Materialia 61(11):1068-1071.

Albert, S. K., V. Ramasubbu, N. Parvathavarthini and T. P. S. Gill. 2003. "Influence of alloying on hydrogen-assisted cracking and diffusible hydrogen content in Cr-Mo steel welds." Sadhana-Academy Proceedings in Engineering Sciences 28:383-393.

Allen, D. J., B. Harvey and S. J. Brett. 2007a. ""FOURCRACK" - An investigation of the creep performance of advanced high alloy steel welds." International Journal of Pressure Vessels and Piping 84(1-2):104-113.

Anderson, P., T. Bellgardt and F. L. Jones. 2003. "Creep deformation in a modified 9Cr-1Mo steel." Materials Science and Technology 19(2):207-213.

Bhadeshia, HKDH. 2004. "Developments in martensitic and bainitic steels: role of the shape deformation." Materials Science and Engineering A 378(1-2):34-39.

Bhadeshia, HKDH. 1999. "Some phase transformations in steel." Materials Science and Technology 15:22 - 29.

Bhadeshia, HKDH. and RWK. Honeycombe. 2006. Steels: Microstructure and Properties. 3rd Edition. Oxford: Elsevier.

Brett, S. J. 2004. "Type IIIa cracking in 1/2CrMoV steam pipework systems." Science and Technology of Welding and Joining 9(1):41-45.

BSI. 1987a. "2633:1987 Specification for Class I arc welding of ferritic steel pipework for carrying fluids." London: BSI.

BSI. 1987b. "Specification for Class I arc welding of ferritic steel pipework for carrying fluids." In 2633:1987. London: BSI.

Bugge, J., S. Kjaer and R. Blum. 2006. "High-efficiency coal-fired power plants development and perspectives." Energy 31(10-11):1437-1445.

Cai, G. J., H. O. Andren and L. E. Svensson. 1997. "Effect of cooling after welding on microstructure and mechanical properties of 12 pct Cr steel weld metals." Metallurgical and Materials Transactions A-Physical Metallurgy and Materials Science 28(7):1417-1428.

Cerjak, H. and E. Letofsky. 1998. "The effect of welding on the microstructural development of advanced 9-12 Cr steels." Microstructural Stability of Creep Resistant Alloys for High Temperature Plant Applications(2):323-337.

Chew, P. E. 2003. "PF-fired supercritical power plant." Proceedings of the Institution of Mechanical Engineers Part a-Journal of Power and Energy 217(A1):35-43.

Chilukuru, H., K. Durst, S. Wadekar, M. Schwienheer, A. Scholz, C. Berger, K. H. Mayer and W. Blum. 2009. "Coarsening of precipitates and degradation of creep resistance in tempered martensite steels." Materials Science and Engineering: A 510-511:81-87.

Cool, Tracey. and HKDH. Bhadeshia. 1997. "Austenite formation in 9Cr-1Mo type power plant steels." Science and Technology of Welding and Joining 2(1):36 - 42.

Cui, H. R., F. Sun, K. Chen, L. T. Zhang, R. C. Wan, A. D. Shan and J. S. Wu. 2010. "Precipitation behavior of Laves phase in 10%Cr steel X12CrMoWVNbN10-1-1 during short-term creep exposure." Materials Science and Engineering A 527(29-30):7505-7509.

Czyrska-Filemonowicz, A, K Bryla, K Spiradek-Hahn, H Firganek, A Zielinska-Lipiec and PJ Ennis. 2003. "The Role of Boron in the 9% Chromium Steels for Steam Power Plants." In Sixth International Charles Parsons Turbine Conference. Dublin:365-377

Dimmler, G., P. Weinert, E. Kozeschnik and H. Cerjak. 2003. "Quantification of the Laves phase in advanced 9-12% Cr steels using a standard SEM." Materials Characterization 51(5):341-352.

EIA. 2006. "International Energy Outlook 2006.". Washington, DC: Energy Information Administration, U.S. Department of Energy.

Ennis, P. J. and A. Czyrska-Filemonowicz. 2003. "Recent advances in creep-resistant steels for power plant applications." Sadhana-Academy Proceedings in Engineering Sciences 28:709-730.

Ennis, P. J., A. Zielinska-Lipiec and A. Czyrska-Filemonowicz. 1998. "Quantitative comparison of the microstructures of high chromium steels for advanced power stations." Microstructural Stability of Creep Resistant Alloys for High Temperature Plant Applications(2):135-143.

Ennis, P. J., A. Zielinska-Lipiec and A. Czyrska-Filemonowicz. 2000. "Influence of heat treatments on microstructural parameters and mechanical properties of P92 steel." Materials Science and Technology 16(10):1226-1232.

Ennis, P. J., A. ZielinskaLipiec, O. Wachter and A. CzyrskaFilemonowicz. 1997. "Microstructural stability and creep rupture strength of the martensitic steel P92 for advanced power plant." Acta Materialia 45(12):4901-4907.

Evans, H. E. 1984. Mechanisms of Creep Fracture. London and New York: Elsevier Applied Science Publisher.

Evans, R W and B Wilshire. 1993. Introduction to Creep. London: The Institute of Materials.

Evans, R. W. and B. Wilshire. 1985. Creep of Metals and Alloys. London: The Institute of Metals.

Falat, L., A. Výrostková, V. Homolová and M. Svoboda. 2009. "Creep deformation and failure of E911/E911 and P92/P92 similar weld-joints." Engineering Failure Analysis 16(7): 2114-2120

Francis, J. A., HKDH Bhadeshia and P. J. Withers. 2007. "Welding residual stresses in ferritic power plant steels." Materials Science and Technology 23(9):1009-1020.

Francis, J. A., W. Mazur and HKDH Bhadeshia. 2004. "Estimation of type IV cracking tendency in power plant steels." ISIJ International 44(11):1966-1968.

Gaffard, V., A. F. Gourgues-Lorenzon and J. Besson. 2005. "High temperature creep flow and damage properties of 9Cr1MoNbV steels: Base metal and weldment." Nuclear Engineering and Design 235(24):2547-2562.

García de Andrés, C., F. G. Caballero, C. Capdevila and L. F. Álvarez. 2002. "Application of dilatometric analysis to the study of solid-solid phase transformations in steels." Materials Characterization 48(1):101-111.

Gianfrancesco, A. Di, L. Cipolla, D. Venditti, S. Neri and M. Calderini. 2009. "Creep Behaviour and Microstructural Stability of FB2 (CrMoCoB) Steel Trial Rotor." In 2nd ECCC Creep Conference, eds. I. A. Shibli and S. R. Holdsworth. Zurich, Switzerland: DEStech Publications, Inc.

Golpayegani, Ardeshir, Mats Hattestrand and Hans-Olof Andren. 2003. "Effect of Boron and Copper on Precipitate Growth and Coarsening in Martensitic Chromium Steels." In Sixth International Charles Parsons Turbine Conference. Dublin:347-363

Gomez, M., L. Rancel and S. F. Medina. 2009. "Effects of aluminium and nitrogen on static recrystallisation in V-microalloyed steels." Materials Science and Engineering: A- 506(1-2):165-173.

Hald, J. 1996. "Metallurgy and creep properties of new 9-12%Cr steels." Steel Research 67(9):369-374.

Hald, J. and L. Korcakova. 2003. "Precipitate stability in creep resistant ferritic steels - Experimental investigations and modelling." ISIJ International 43(3):420-427.

Hasegawa, Y., T. Muraki, M. Ohgami and H. Mimura. 2000. "Optimum tungsten content in high strength 9 to 12% chromium containing creep resistant steels." Creep and Fracture of Engineering Materials and Structures 171-1:427-435.

Helis, L., Y. Toda, T. Hara, H. Miyazaki and F. Abe. 2009. "Effect of cobalt on the microstructure of tempered martensitic 9Cr steel for ultra-supercritical power plants." Materials Science and Engineering: A 510-511:88-94.

Hosoi, Y., N. Wade, S. Kunimitsu and T. Urita. 1986a. "Precipitation behavior of laves phase and its effect on toughness of 9Cr-2Mo ferritic martensitic steel." Journal of Nuclear Materials 141:461-467.

Hosoi, Y., N. Wade and T. Urita. 1986b. "Effect of Si and Mn on precipitation behavior of laves phase and toughness of 9Cr-2Mo steel." Transactions of the Iron and Steel Institute of Japan 26(1):B30-B30.

Hu, Xiaoqiang, Namin Xiao, Xinghong Luo and Dianzhong Li. 2010. "Transformation Behavior of Precipitates in a W-alloyed 10 wt pct Cr Steel for Ultra-supercritical Power Plants." Journal of Materials Science & Technology 26(9):817-822.

Hunt, A. C., A. O. Kluken and G. R. Edwards. 1994. "Heat input and dilution effects in microalloyed steel weld metals." Welding Journal 73(1):S9-S15.

Issler, S., A. Klenk, A. A. Shibli and J. A. Williams. 2004. "Weld repair of ferritic welded materials for high temperature application." International Materials Reviews 49(5):299-324.

Kitto, J B. 1996. "Technology development for advanced pulverized coal-fired boilers ." In Power-Gen International. Orlando, FL

Klueh, R. L. 2005. "Elevated temperature ferritic and martensitic steels and their application to future nuclear reactors." International Materials Reviews 50(5):287-310.

Klueh, R. L., N. Hashimoto and P. J. Maziasz. 2005. "Development of new nano-particle-strengthened martensitic steels." Scripta Materialia 53(3):275-280.

Knezevic, V., J. Balun, G. Sauthoff, G. Inden and A. Schneider. 2008. "Design of martensitic/ferritic heat-resistant steels for application at 650 degrees C with supporting thermodynamic modelling." Materials Science and Engineering A 477(1-2):334-343.

Kohlhofer, W. and R. K. Penny. 1996. "Hardness testing as a means for creep assessment." International Journal of Pressure Vessels and Piping 66(1-3):333-339.

Korcakova, L., J. Hald and M. A. J. Somers. 2001. "Quantification of Laves phase particle size in 9CrW steel." Materials Characterization 47(2):111-117.

Kunimitsu, S., Y. You, N. Kasuya, Y. Sasaki and Y. Hosoi. 1991. "Effect of thermomechanical treatment on toughness of 9Cr-W ferritic-martensitic steels during aging." Journal of Nuclear Materials 179:689-692.

Lancaster, J. F. 1993. Metallurgy of Welding. 5th Edition: Chapman & Hall.

Leblond, J. B., G. Mottet and J. C. Devaux. 1986. "A theoretical and numerical approach to the plastic behavior of steels during phase-transformations .1. Derivation of general relations." Journal of the Mechanics and Physics of Solids 34(4):395-409.

Mannan, S. L. and K. Laha. 1996. "Creep behaviour of Cr-Mo steel weldments." Transactions of the Indian Institute of Metals 49(4):303-320.

Marshall, A. W., Z. Zhang and G. B. Holloway. 2002. "Welding consumables for P92 and T23 creep resisting steels." In 5th International Conference Welding and Repair Technology for Power Plants. Alabama. P6-1

Maruyama, K., K. Sawada and J. Koike. 2001. "Strengthening mechanisms of creep resistant tempered martensitic steel." ISIJ International 41(6):641-653.

Masuyama, F. 1999. "New developments in steels for power generation boilers." Conference on Advanced Heat Resistant Steels for Power Generation, San Sebastian, Spain:33-48.

Masuyama, F. 2001. "History of power plants and progress in heat resistant steels." ISIJ International 41(6):612-625.

Miyahara, K., J. H. Hwang and Y. Shimoide. 1995. "Aging phenomena before the precipitation of the bulky laves phase in Fe-10-percent-Cr ferritic alloyS." Scripta Metallurgica Et Materialia 32(12):1917-1921.

Miyamoto, G., H. Usuki, Z. D. Li and T. Furuhara. 2010. "Effects of Mn, Si and Cr addition on reverse transformation at 1073 K from spheroidized cementite structure in Fe-0.6 mass% C alloy." Acta Materialia 58(13):4492-4502.

Nawrocki, J. G., J. N. DuPont and A. R. Marder. 2000. "A study on the carbide precipitation in a ferritic steel." In Microbeam Analysis 2000, Proceedings, eds. D. B. Williams and R. Shimizu. Bristol: IOP Publishing Ltd.:175-176

Oi, K., C. Lux and G. R. Purdy. 2000. "A study of the influence of Mn and Ni on the kinetics of the proeutectoid ferrite reaction in steels." Acta Materialia 48(9):2147-2155.

Onoro, J. 2006. "Weld metal microstructure analysis of 9-12% Cr steels." International Journal of Pressure Vessels and Piping 83(7):540-545.

Orlova, A., J. Bursik, K. Kucharova and V. Sklenicka. 1998. "Microstructural development during high temperature creep of 9% Cr steel." Materials Science and Engineering a-Structural Materials Properties Microstructure and Processing 245(1):39-48.

Oñoro, J. 2006. "Martensite microstructure of 9-12%Cr steels weld metals." Journal of Materials Processing Technology 180(1-3):137-142.

Paul, I., R. Taud and D. O'Leary. 2005. "Tailor-made off the shelf: reducing the cost and construction time of thermal power plants. ." The World Bank Group

Reddy, G. M., T. Mohandas and D. S. Sarma. 2003. "Cold cracking studies on low alloy steel weldments: effect of filler metal composition." Science and Technology of Welding and Joining 8(6):407-414.

Richardot, D, JC Vaillant, A Arbab and W Bendick. 2000. The T92 P92 Book: Vallourec & Mannesmann Tubes.

Santella, M. L., S. S. Babu, R. W. Swindeman and E. D. Specht. 2003. "In-situ characterization of austenite to martensite decomposition in 9Cr-IMo-v steel welds." Symposium on Austenite Formation and Decomposition, Chicago IL:247-256.

Santella, Michael. 2010. "Influence of chemical compositions on lower ferrite-austenite transformation temperatures in 9Cr steels." J. Pressure Vessel Technol. 134(2)

Savage, W. F. and A. H. Aronson. 1966. "Preferred orientation in the weld fusion zone." Welding Journal 45(2):85-89.

Savage, W. F., E. F. Nippes and E. S. Szekeres. 1976. "Study of weld interface phenomena in a low-alloy steel." Welding Journal 55(9):S260-S268.

Sawada, K., K. Kubo and F. Abe. 2001a. "Creep behavior and stability of MX precipitates at high temperature in 9Cr-0.5Mo-1.8W-VNb steel." Materials Science and Engineering A 319:784-787.

Sawada, K., K. Kubo and F. Abe. 2001b. "Creep behavior and stability of MX precipitates at high temperature in 9Cr-0.5Mo-1.8W-VNb steel." Materials Science and Engineering A 319-321:784-787.

Sawada, K., K. Kubo and F. Abe. 2003. "Contribution of coarsening of MX carbonitrides to creep strength degradation in high chromium ferritic steel." Materials Science and Technology 19(6):732-738.

Sawada, K., M. Takeda, K. Maruyama, R. Ishii, M. Yamada, Y. Nagae and R. Komine. 1999. "Effect of W on recovery of lath structure during creep of high chromium martensitic steels." Materials Science and Engineering A 267(1):19-25.

Shibli, A. 2008. "Performance of modern high strength steels (P91, P92) in high temperature plant." Proceedings of the ASME Pressure Vessels and Piping Conference 2007, Vol 9:161-170.

Shirane, T., S. Tsukamoto, K. Tsuzaki, Y. Adachi, T. Hanamura, M. Shimizu and F. Abe. 2009. "Ferrite to austenite reverse transformation process in B containing 9%Cr heat resistant steel HAZ." Science and Technology of Welding and Joining 14(8):698-707.

Sourmail, T. 2001. "Precipitation in creep resistant austenitic stainless steels." Materials Science and Technology 17(1):1-14.

Spigarelli, S. and E. Quadrini. 2002. "Analysis of the creep behaviour of modified P91 (9Cr-1Mo-NbV) welds." Materials & Design 23(6):547-552.

Tamura, M., H. Sakasegawa, A. Kohyama, H. Esaka and K. Shinozuka. 2003. "Effect of MX type particles on creep strength of ferritic steel." Journal of Nuclear Materials 321(2-3):288-293.

Vaillant, J. C., B. Vandenberghe, B. Hahn, H. Heuser and C. Jochum. 2008. "T/P23, 24, 911 and 92: New grades for advanced coal-fired power plants-Properties and experience." International Journal of Pressure Vessels and Piping 85(1-2):38-46.

Viswanathan, R. and W. Bakker. 2001a. "Materials for ultrasupercritical coal power plants - Turbine materials: Part II." Journal of Materials Engineering and Performance 10(1):96-101.

Viswanathan, R. and W. Bakker. 2001b. "Materials for ultrasupercritical coal power plants-boiler materials: Part 1." Journal of Materials Engineering and Performance 10(1):81-95.

Viswanathan, R., K. Coleman and U. Rao. 2006. "Materials for ultra-supercritical coal-fired power plant boilers." International Journal of Pressure Vessels and Piping 83(11-12):778-783.

Watanabe, T., M. Yamazaki, H. Hongo, M. Tabuchi and T. Tanabe. 2004. "Effect of stress on microstructural change due to aging at 823 K in multi-layer welded joint of 2.25Cr-1Mo steel." International Journal of Pressure Vessels and Piping 81(3):279-284.

Wu, R., R. Sandstrom and F. Seitisleam. 2004. "Influence of extra coarse grains on the creep properties of 9 percent CrMoV (P91) steel weldment." Journal of Engineering Materials and Technology-Transactions of the ASME 126(1):87-94.

Yang, J R. and H K D H. Bhadeshia. 1989. "Reaustenitization Experiments on some High-strength Steel Weld Deposits." Materials Science and Engineering A 118:155 - 170.

Yeh, Sonia and Edward S. Rubin. 2007. "A centurial history of technological change and learning curves for pulverized coal-fired utility boilers " Energy 32:1996-2005.

Yin, F. S. and W. S. Jung. 2009. "Nanosized MX Precipitates in Ultra-Low-Carbon Ferritic/Martensitic Heat-Resistant Steels." Metallurgical and Materials Transactions a-Physical Metallurgy and Materials Science 40A(2):302-309.

Yin, Y. F. and R. G. Faulkner. 2003. "Simulations of precipitation in ferritic steels." Materials Science and Technology 19(1):91-98.

Yoshizawa, M., M. Igarashi, K. Moriguchi, A. Iseda, Hassan Ghassemi Armaki and K. Maruyama. 2009. "Effect of precipitates on long-term creep deformation properties of P92 and P122 type advanced ferritic steels for USC power plants." Materials Science and Engineering A 510-511:162-168.

Zielinska-Lipiec, A. and A. Czyrska-Filemonowicz. 2007. "Characterisation of the micro- and nanoscale structure of new creep-resistant steels for use in advanced USC steam power plants." Materials Transactions 48(5):931-935.